Stony Brook University

Characterization of Damage due to Environmental Conditions in Heterogeneous Material Systems

A Dissertation Presented

by

Narayanan Ramanujam

to

The Graduate School

in Partial Fulfillment of the

Requirements

for the Degree of

Doctor of Philosophy

in

Mechanical Engineering

Stony Brook University

December 2007

Stony Brook University

The Graduate School

Narayanan Ramanujam

We, the dissertation committee for the above candidate for the

Doctor of Philosophy degree,

hereby recommend acceptance of the dissertation.

Toshio Nakamura, Dissertation Advisor
Professor, Department of Mechanical Engineering

Chad S. Korach, Chair
Professor, Department of Mechanical Engineering

Jeffrey Ge, Member
Professor, Department of Mechanical Engineering

Sanjay Sampath, Outside Member
Professor, Department of Materials Science and Engineering

This dissertation is accepted by the Graduate School

Lawrence Martin
Dean of the Graduate School

Abstract of the Dissertation

Characterization of Damage due to Environmental Conditions in Heterogeneous Material Systems

by

Narayanan Ramanujam

Doctor of Philosophy

in

Mechanical Engineering

Stony Brook University

2007

Heterogeneous materials including fiber-reinforced composites and thermal sprayed coatings have the potential of offering tailored mechanical properties for specific engineering applications; however their susceptibility to different mechanisms of damage is a cause for concern. The various damage mechanisms addressed in the present study are exposure to harsh environments that include cyclic exposure to ultra-violet (UV) radiation and moisture, thermal cycling and erosion due to foreign particle impact. There is a need for characterization of damage resistance of a heterogeneous material system. With this as a motivation, first, a new inverse analysis based procedure is proposed and applied to real material systems. Strain-damage relations are formulated and followed by an iterative technique to identify damages caused by environmental exposure/physical damages in fiber-reinforced composites. Verification analyses are

carried out to check the validity of the proposed procedure. Next, real cross-ply composite laminates are considered and damages identified. Furthermore, failure tests are performed to examine the residual strengths and early onset of delamination. In the second phase of work, interlaminar fatigue crack propagation is characterized in thermally cycled fiber-reinforced composites with recourse to 3D finite element modeling in conjunction with previously performed experiments. It was observed that energy release rates correlate to crack growth behavior through a Paris law relation.

In the final phase of work, erosion of coatings subjected to hard particle impact is addressed. First, experiments are performed using a test rig to obtain mass loss curves for heterogeneous thermal barrier coatings. Next, the erosion phenomenon is modeled for the first time via 2D finite element simulation and damages characterized. Current study offers significant insights regarding the mechanisms of damage and approximate erosion extents using 2D models. Comparisons made with results obtained from experiments qualify the current procedure albeit with refinements for modeling solid particle impact erosion problem in thermal barrier coatings.

Dedicated to my parents and my brother

Table of Contents

List of Figures

List of Tables

Acknowledgements

The experience of being involved in academic research for undertaking my doctoral degree has been truly wonderful and I am deeply indebted to my advisor, *Professor Toshio Nakamura* who instilled in me the qualities for conducting research in solid mechanics. I would consider myself very fortunate to be associated with a person of such high talent and one of the pioneers in the field of fracture mechanics. I would also like to thank him for his continued support and motivation that he provided me over the last six years. I am very grateful to the other members of my dissertation committee, *Professor Chad Korach, Professor Jeffrey Ge* and *Professor Sanjay Sampath* who reviewed my work and offered insightful comments. I am thankful to *Professor Raman P. Singh* for his invaluable advice and guidance during my experimental work. I would like to specially thank *Masataka Urago* for helping me on the work of environmental degradation of fiber reinforced composites. I am very grateful to *Zhiqiang Wang* for his work on cohesive element formulation for four noded elements that I could extend to model erosion of coatings. I am also thankful to *Pavankiran Vaddadi* who conducted experiments on fiber reinforced composites whose work I could extend.

I am very thankful to all the members of the computational mechanics laboratory, *Yu Gu, Bhavesh G. Kumar, Yajie Liu, Jian Yao* and *Swet Chandan* for their concern and support. These years at the laboratory have been memorable and have left an indelible impression on me.

I would like to show my gratitude to the former members of the Mechanics of Advanced Materials Lab at Stony Brook including *Abhishek Singh, Sehaj P. Singh* and

Suraj Zunjarrao. I am indebted to the members of the Center for Thermal Spray Research especially *Alfredo Valarezo*, *Vasudevan Srinivasan*, *Weiguang Chi*, *Eduardo Mari* and *Yu-Hong Wu* for their unconditional help toward the work on erosion of coatings. I am grateful to the members of laboratory for nanotribology and wear mechanics especially

I would like to thank my parents and my brother beyond words for their constant encouragement despite facing personal hardships. Last but not the least; I am thankful to all prospective readers of my thesis for their interest.

1. INTRODUCTION

During service, heterogeneous materials including fiber reinforced composites and thermal barrier coatings are exposed to many events that include complex loading and harsh environmental conditions. As a result, despite of those inherent benefits, they are susceptible to environmental degradation, fiber breakage during impact related events and delamination between adjacent plies. The lowered damage tolerance/resistance that results may have an adverse effect on structural durability and reliability. The quantification of structural degradation hence becomes essential for accurate determination of residual strength to avoid expenses due to numerous redundant inspections. In the present research, principal efforts are directed towards understanding damages resulting from exposure to harsh environments (UV radiation, moisture and thermal cycling) and physical damages including erosion caused by contact fatigue/hard particle impact. These data then would be vital for development of guidelines for determining the optimal frequency of inspection and repair before catastrophic failure occurs.

1.1. Background – Degradation/Physical Damage of Composites

Advanced materials particularly fiber-reinforced composites used in applications ranging from aerospace structures to recreational products are designed to possess high strength and specific stiffness. Other numerous advantages when compared with conventional materials include low density, high strength at elevated temperatures, good impact and thermal shock resistance, good fatigue resistance, better oxidation and corrosion resistance and tailored properties designed to meet specific engineering needs

[1]. Despite these inherent benefits their susceptibility to environmental degradation and physical damage raises questions about their integrity.

Numerous studies have essentially attempted to delineate the behavior of fiber-reinforced composites when submitted to harsh environmental conditions. For example, Shen and Springer [2] studied the effect of moisture and temperature on the tensile strength of T300/1034 graphite/epoxy composites. They found that for unidirectional laminates, ultimate tensile strength is significantly affected by the moisture content and the temperature. Larsson [3] evaluated the influence on the mechanical properties of unidirectional Kevlar-49 epoxy laminates of varying thickness due to degradation by ultraviolet light exposure. Yoosefinejad and Hogg [4] have studied observed a 40% decrease in overall strength of composite components after 20 years in service when compared to new panels. Recently, Shin and Hahn [5] have observed an extensive drop in modulus when composites are subjected to accelerated ageing conditions including UV radiation, temperature and moisture for 2000 hours. Moreover, Purnell and Beddows [6] have observed significant drops in elastic modulus of glass fiber reinforced concrete after 316 days of exposure. They also observed drastic changes in flexural failure stress only after 28 days. Furthermore, Kumar et al. [7] have undertaken an approach towards understanding the behavior of carbon fiber reinforced plastics when exposed to multiple environments. Prior to this work, scant attention was paid to synergistic effects of combined exposure to UV radiation and water vapor, which are predominantly responsible for degradation during outdoor service [8]. They argued that extensive amount of epoxy was removed only after 1000 hours of exposure. Even though the fibers themselves are barely affected by environmental exposure, the strength of the composite

as a whole would significantly decrease due to the limitation of load transfer to fibers. Recent research on environmental degradation of composites has been directed towards estimation of their effective elastic properties with damage modeled through analytical, experimental as well as finite element analyses [9,10]. Sevostianov et al. [11] have proposed a model to depict environmental degradation in polymer composites and to determine the bulk properties of laminates.

Frequently, extents of damages are measured using non-destructive evaluation (NDE) techniques such as radiography, ultrasonic, acoustic emissions, electrical, liquid penetration, conductivity, holography, radar and others. Although some are very effective, these procedures often require expensive equipments/tools and complex processes to quantify damages. A comprehensive review of NDE techniques by McCann and Forde [12] notes the high cost of advanced inspection methods such as a radiography that relies on x-ray or γ-ray. In fact, such a method not only requires high capital and operating costs but also large space and lengthy set-up time. Therefore, as the requirement to evaluate complex material/structure systems increases, it is beneficial to develop a simpler but still effective method. Such a goal may be realized with an aid of *intelligent* post-processing scheme.

In the current work, the objective is to develop a robust damage evaluation process for composite laminates without expensive measurement tools. Also it is intended to lay groundwork for attached sensors to monitor structural integrity during operations. In order to accomplish this goal, a novel approach to process gathered data with an inverse analysis procedure is proposed and implemented in test specimens. In recent years, various inverse models have been introduced to determine critical material

parameters. Maniatty et al. [13,14] have utilized an inverse analysis technique coupled with finite element method to solve for elastic and viscoplastic properties. Cao et al. [15] proposed an approach based on artificial neural networks for identification of unknown load. More recently, Vaddadi et al. [16] have developed an inverse approach to estimate critical moisture diffusion parameters of fiber-reinforced composites. Other investigations include a flexibility-based approach for damage localization and quantification [17], fiber-optics for delamination detection in composites [18], remote structural damage monitoring with smart terminals through the frequency response change [19], detection of crack by the body force method [20] and damage region identification by neural network-based detectors [21]. The present approach post-processes strain measurements to identify distributions of surface damage and degradation. The strains can be obtained either with a grid/network of strain-gages [22] or with one of various optical methods, which offer full-field measurements. A possible difficulty in identifying damage lies on relating measured strains to damage distributions. Here, approximate functions for a given state of damage are established, and the estimation of damage distribution is carried out with a multivariate iterative operation.

The third environmental factor addressed in the current study (other than UV radiation and moisture) includes erosive damage of composites due to solid particle impact. Literature survey shows that erosion wear has been studied primarily experimentally. For example, Pool et al. [23] observed that the continuous graphite fiber reinforced epoxy composites showed a brittle behavior where maximum erosion occurred for normal impact of particles. However, Tewari et al. [24] have reported a semi-ductile behavior of these composites under other testing conditions. Thus, these data have to be

used with caution as results can vary based on test parameters. In the present study, solid particle erosion behavior is analyzed for a different heterogeneous material system (thermal barrier coatings) and not on fiber-reinforced composites.

Finally, the fourth environmental factor posing in-service threat studied includes thermal cycling of composites. Thermal cycling causes fatigue crack growth and is one of major failure mechanisms in composites [25-29]. The fracture process of composite laminates subjected to fatigue loading involves a sequential accumulation of intralaminar and interlaminar damage in the form of transverse cracking, fiber splitting and delamination prior to catastrophic failure [30]. Fatigue of composite materials can be driven by mechanical loads, thermal loads or a combination of both [31]. To analyze their thermal fatigue behaviors, several empirical models have been proposed. Eselun *et al*. [32] noted influences of resin microcracks generated by thermal cycling on fatigue life, tensile strength and interlaminar shear strength. Cohen et al. [33] found that during thermal cycling, cracks accumulated up to a brief number of cycles, remained constant and later increased. Herakovich and Hyer [34] studied thermal cycling crack density as a function of layer thickness and number of transverse plies. They also found extensive damage in epoxy resin that included delamination. Adams *et al*. [35] showed the effects of space environment on cross ply composites and concluded that cracks tend to avoid resin rich areas and delaminations grew from transverse cracks. Others reported that elastic properties of thermally cycled carbon fiber composites were not significantly reduced while transverse tensile strength and interlaminar strength were appreciably reduced [36, 37]. Another study characterized crack growth in epoxy due to thermal

fatigue [38]. Many of these studies assumed the crack density as a function of thermal cycles.

However, investigations on thermal delamination growth between laminae are rather limited. The effects of mechanical and thermal loads on fatigue were studied for curved layered composites by Figiel and Kaminski [30]. They used the linear elastic fracture theory and the finite element analysis to solve the fatigue delamination problem. Although not for composite laminates, Gurumurthy *et al*. [39] developed an experimental procedure for measuring the crack growth along polymer interfaces under hygrothermal fatigue. The experimentally measured crack growth per unit temperature cycle (*da/dN*) was correlated to the magnitude of the energy release rate (ΔG) during temperature cycles. Optical micrographs of the damage induced to a composite specimen by the three different phenomena are shown in Fig. 1.1.

1.2. Background – Solid Particle Erosion of Thermal Barrier Coatings

Hard particle erosion is a real concern in engineering systems including gas turbines and coal conversion plants. Such erosive wear occurring when solid particles entrained in a fluid stream strike a surface has been a serious and continuing problem in several industrial operations [40]. The problem of characterizing post-impact debris is vital to determine the survivability of the material system under consideration as the so called craters act as potential sites for fatigue crack initiation due to stress concentration. At present scanning electron microscopes (SEM) and optical profilometers are used to obtain images of impacted surface for examination [41]. Extensive data is available from literature pertaining to erosion of both metals and brittle materials obtained from different empirical approaches.

Although ceramics (predominant phase in TBC studied) are high performance materials used to offer high corrosion resistance, their main weakness is low fracture toughness. From the literature review, it is clear that erosion in brittle materials occurs by onset, propagation and intersection of cracks to from fragments. This mechanism which addresses cracking and chipping as the dominant mode of material removal is based on the Hertzian/indentation fracture theory. The proposed damage mechanisms are based on either cracking patterns occurring due to single particle or multiple particles impact on a smooth surface or patterns evolving from static indentation related fracture [40]. The latter approach is based on the presumption that even for a brittle surface, there is a region of plastic deformation below the indenter where high stresses occur upon loading. Vertical cracks ensue beneath this region that may cause premature component failure and are considered unfavorable. The formation of fragments however occurs upon unloading from propagation of lateral cracks to the surface [42]. Regardless of the damage mechanism, one of the characteristic behaviors of brittle materials is that the maximum erosion occurs during normal impact of particles although there is a so-called brittle-ductile transition but is significant only for smaller sized abrasive particles (~9 μm) [40].

Specifically, plasma sprayed coatings that represent a versatile and cost effective solution for tribological and high temperature corrosion applications are susceptible to solid particle erosion [43]. One of the prominent works was by Usmani and Sampath [44] who studied erosion behavior of duplex and graded ceramic coatings. In the current study, three different material systems with varying volume fractions of phases consisting of a predominantly ceramic phase (YSZ) are considered. The rest of the phases consist of

CoNiCrAlY (Cobalt-Nickel-Chromium-Aluminum-Yttrium alloy) and Al_2O_3 (alumina) formed due to the oxidation of aluminum during the spraying process. It could then be expected that the coatings would undergo erosion primarily through brittle modes. Further, there is interesting evidence from erosion data that NiCrAlY under room temperature exhibits brittleness in coatings [45]. Here it was also suggested that the cracking mechanism occurs in the presence of negligible plastic deformation. Furthermore, it is elucidated by Karimi and Schmid [46] that thermally sprayed metals too exhibit brittleness as opposed to damage through plastic deformation which is the dominant mode of material removal for ductile materials. Hence, it can be assumed that erosive damage is caused by progressive cracking and chipping of coatings although the porous microstructure leads to other mechanisms in conjunction. In plasma sprayed coatings there are currently no models developed for capturing the damage mechanisms during solid particle erosion.

There are several empirical data available for plasma sprayed coatings as well as electron beam physical vapor deposited (EB-PVD) coatings. For plasma sprayed coatings, Gutlebar et al. [47] examined the role of processing conditions and thermal cycling on erosive behavior of TBC. Others [48-51] have extensively studied TBC morphology and aging on erosion rate. They observed different mechanisms of material removal depending on parameters such as particle velocity, size, temperature and material. Wellman and Nicholls [52] have proposed a Monte-Carlo modeling of erosion process for a wide range of dynamic conditions. However, they do not take into account the discrete nature of cracks for brittle materials. Computational models developed for modeling solid particle erosion of brittle materials are sparse. They are mainly based on

studying the stresses developed around a spherical impactor without modeling cracking [53]. One of the first studies that took into account the effect of discrete nature of cracks for modeling dynamic impact damage in brittle materials by avoiding homogenization assumptions was by Camacho and Ortiz [54] albeit not for erosion.

In the present work, coatings with three different compositions of the YSZ phase are considered. First, they are eroded using an erosion test rig. Next, an approximate estimate of depth and volume of erosion are obtained from the mass loss data. A micrograph of eroded profile for 100% YSZ coating is shown in Fig. 1.2. The legend shows the various depths with respect to the steel substrate. Following this, 2D computational models are set up taking into consideration the heterogeneous microstructure of coatings to account for brittle cracking by embedding cohesive elements along every element boundary. Erosion profiles and energy evolution are obtained through computations and compared with the erosion rates obtained experimentally. The present model needs further refinements before it can characterize erosive damage in predominantly brittle materials. Nevertheless, interesting qualitative insights can be obtained using current models about fragmentation profiles and energy absorption characteristics. Figure 1.2 highlights the surface micrograph of YSZ specimen after submitting to erosion.

1.3. Damage Mechanism - Environmental Degradation of Composites

Carbon fiber composites as mentioned previously are versatile that allow for a wide variety of designs [55]. It has been noted that there might be some coupling among the various degradation effects [56]. Liao et al. [57] have provided a comprehensive review

on the effects of ageing on composites. Degradation primarily involves ageing of the polymer phase [55] with carbon fibers relatively unaffected. The combined action of temperature, humidity and UV radiation was studied for glass fiber reinforced polymer composites by Mouzakis et al. [58]. They subjected the specimens to ageing environment and found that the aged materials gained in stiffness and slight loss in strength. They reported finding microcracks in polymer phase that attributed to drop in strength. However, a study by Silva [59] has shown that cycles of UV radiation and flooding in glass fiber reinforced composites result in a continuous drop in tensile strength albeit the elastic modulus drop being marginal. The three major outdoor conditions including environmental degradation, moisture absorption and thermal cycling are elaborated upon next.

Environmental degradation of composites has attained significant attention in the recent years. A variety of outdoor conditions including UV radiation, moisture, temperature and high pH environments are responsible for the susceptibility of polymer matrix in carbon fiber reinforced epoxy composites. In this study the cyclic exposure to UV and moisture is considered as a major factor leading to the reduction in the residual strength in laminates in light of the findings by Kumar et al. [7]. The detrimental effects of exposure to UV radiation are discussed below. The energy available from UV photons results in dissociation of polymer covalent bonds so that the chemical structure of composites is altered due to photo-oxidative reactions leading to material deterioration [60]. Polymer chain scission and cross-linking are the two phenomena that occur due to UV exposure. While chain scission causes lowering of molecular weight of polymer that

leads to a reduction in strength, cross-linking leads to excessive brittleness in polymer that leads to formation of microcracks [7].

On the other hand moisture absorption is not as detrimental to the composite material system as exposure to UV. There are relatively few studies aimed at addressing the issues posed by moisture absorption in CFRP laminates. Primarily, the ill-effects on interfacial properties [61], strains induced by temperature and moisture [62] and fatigue behavior of composites [63] due to hygro-thermal treatments are studied. Other class of problem includes damage to adhesive joint that bond CFRP laminates by moisture uptake [64]. The mechanism of damage induced can be summarized as follows. A drop in glass transition temperature occurs with increasing moisture absorption. Fibers themselves do not however absorb moisture. Hence, it is natural to expect an increase in the amount of moisture absorption with an increasing matrix volume fraction. Primarily moisture diffusion causes plasticization and hydrolysis of polymer. Plasticization tends to soften the polymers increasing their elongation under tensile loading whereas hydrolysis is responsible for chemical decomposition in polymers.

The behavior of a particular class of CFRP laminates when subjected to UV and moisture in a cyclic manner is surprisingly different from what one would expect if a linear superposition of effects is assumed. The so called synergistic effects of UV and moisture on composite degradation are discussed in detail by Kumar et al. [7]. In brief, the micro-cracks in polymers formed by UV exposure act as pathways for rapid ingress of moisture to the interior. The water soluble products formed due to UV exposure are then washed away leading to extensive erosion of matrix. Even though fibers themselves

are not directly affected, the erosion of epoxy limits the load transfer to fibers thereby reducing the laminate strength adversely.

Apart from UV radiation and moisture absorption, thermal cycling is considered a potentially detrimental phenomenon that could lead to failure from interlaminar delamination. Although a majority of studies focus their attention on matrix cracks and fiber fracture (at the microstructural level), there are relatively few studies that address the problem of delamination caused by thermal cycling at the continuum level. The thermal fatigue driven delamination in these composites has been studied with recourse to experiments and computational modeling in a recent study by Ramanujam et al. [65].

1.4. Damage Mechanism - Physical Damage of Composites and Coatings

Direct physical damages in composites primarily cause matrix cracks, fiber-breakages and delaminations as compared to environmental damage which is mainly a matrix phenomenon although it can result in catastrophic failure of the whole material system under consideration. Impact caused by foreign objects, external service load and fatigue related wear are some of the major mechanisms that result in physical damaging of composites. Impact damages caused in composite laminates have more severe implications than in homogenous materials as the resulting delaminations are not visible on the surface. This class of problem with the major focus on detecting embedded delaminations using a new inverse analysis based stochastic procedure has been solved by Ramanujam et al. [66]. In the current study the focus is on quantification of damage that occurs due to material removal from surface. These mechanisms occur by contact fatigue related wear or by impact erosion resulting from solid particles where the transfer of energy is less so that delamination does not occur. Barkoula et al. [67] studied erosive

wear due to particle impact in composite laminates where residual strength was characterized using a semi-empirical approach. An important observation in their study was that the surface topography revealed damages localized at the eroded area. In light of these observations, it is necessary to employ a similar procedure as that for environmentally degraded composite laminates to characterize the damages. The problem of erosion in polymer composites has been studied elaborately studied by several other researchers.

Material removal in coatings due to solid particle impact erosion in hot sections of gas turbines is an area of major concern as mentioned in the Chapter 1. These thermal barrier coatings (TBC) exhibit several failure modes [68]. Large-scale buckling or edge delaminations are major failure modes that have been studied extensively [69]. The mechanisms that lead to failure due to the presence of such a damage is discussed by Chen et al. [70]. The thermal barrier coating under consideration was made from yttria stabilized zirconia [YSZ]. They noted that hard particle impact led to formation of a densified region with lateral cracks near the impact site, from which kink bands emanated and propagated through the TBC towards the interface.

Although damage mechanism for erosion of brittle materials was touched upon in Chapter 1, here the subject is elaborated further. There are primarily two theories that explain crack propagation behavior in ceramics. The nature of stresses in statically indented and dynamically impacted solids are quite different. However, most of the studies are based on interpretations of static contact. The behavior of cracking in homogeneous ceramics is found to be remarkably independent of the duration of impact which allow for quasi-static analyses to be applicable to erosion [71]. For a spherical

indenter that contacts a smooth brittle surface, a ring crack is reported to be first formed. This ring crack then flares to form a cone crack. It has also been extensively reported that the size of the crack formed is proportional to the diameter of the sphere. Such a damage mechanism is more common for impact from spherical particles.

With the angular impacting particles, however, the fracture mechanisms are primarily similar to those studied for conical or pyramidal indenters. Stress gradients in region around the tip are very high if not singular and inelastic processes operate in this region. It has been proposed that beneath this region there are high tensile stresses that are responsible for crack growth in vertical direction also known as the radial/median crack. This crack is more penetrative than the lateral crack that develops during unloading from the residual stress field in the elastically deformed region surrounding the elastic-plastic region. When the lateral crack touches the free surface, they form fragments that are dislodged leading to erosion [72].

All of those studies mentioned above are empirical and do not take into account the dynamic nature of impact thereby employing gross approximations. In the current study, angular particle impact of thermal barrier coatings is modeled via explicit dynamic calculation by simulating multiple cracking and fragmentation to account for erosion. Even though current simulations are performed in 2 dimensions, the modeling procedure can readily be implemented in 3 dimensions. Although there have been attempts to model dynamic impact they have not taken into account the discrete nature of the cracks. The stress field developed for an uncracked model has been interpreted to predict fragmentation phenomenon. In the current model however, cracking phenomenon is modeled using a cohesive element approach embedded in the interface between every

element boundary. The development of a cohesive element approach and implementation to the current model will be discussed in further detail in Chapter 4.

1.5. Summary

The damage mechanisms that prove to be detrimental to composite structures and coatings in-service have been discussed earlier in this section. Matrix embrittlement occurs in UV degraded laminates leading to formation of micro-cracks while less severe effects are observed from exposure to moisture. However, when they act in unison, there is extensive matrix erosion due to synergistic effects. Even though environmental degradation is a matrix phenomenon, it affects the composite laminate adversely due to limitation of load transfer to fibers. In addition, to environmental degradation, direct physical damages occur in composites and coatings due to complex loading conditions and unexpected events encountered during service. Some of the loading conditions that cause material removal from surface include solid particle impact and contact fatigue. The methodology of characterizing these damages is elaborated in the following sections.

This dissertation addresses characterization of damages primarily in two heterogeneous material systems. In Chapter 2 various damage mechanisms resulting from in-service environments are discussed. In Chapter 3, characterization of damage in fiber reinforced composites due to exposure to harsh environments is discussed. Here a robust inverse analysis procedure is developed and implemented to identify extents of damage in real composite specimens. Damages are characterized by post processing of measurements instead of modeling the phenomenon directly. In Chapter 4, however, erosive damage in thermal barrier coatings is modeled using real 2D micro-structural images. A cohesive type traction separation law for brittle cracking and chipping is

utilized to model surface separation. Although full 3D models (computationally expensive) are required to accurately characterize damage; present comparisons with experiments show that 2D models are capable of capturing the damage mechanisms/extents reasonably well.

1.6. References

1) Schwartz, R.T., Schwartz, H.S. (1968). Fundamental Aspects of Fiber-Reinforced Plastics Composites, John Wiley & Sons, Inc., New York, NY.
2) Shen, C.H., Springer, G.S. (1977). Effects of Moisture and Temperature on the Tensile Strength of Composite Materials. *Journal of Composite Materials*, **11**(2):2–16.
3) Larsson F. (1986). The Effect of Ultraviolet Light on Mechanical Properties of Kevlar 49 Composites. *Journal of Reinforced Plastic Composites*, **5**(1):19–22.
4) Yoosefinejad A, Hogg PJ. (1997). Durability of fibre reinforced composite materials after twenty years of exposure to weathering. In: Proceedings of ICCM—11, vol. V, July, p. V493–498.
5) Shin, K.B., Hahn, S.H. (2005). Evaluation of the structural integrity of hybrid railway carriage structures including the ageing effects of composite materials. *Composite Structures*, **68**(2): 129-137.
6) Purnell, P., Beddows, J. (2005). Durability and simulated ageing of new matrix glass fibre reinforced concrete. *Concrete Composites*, **27**(9-10): 875-884.
7) Kumar, B.G., Singh., R.P., Nakamura., T. (2002). Degradation of carbon fiber-reinforced epoxy composites by ultraviolet radiation and condensation. *Journal of Composite Materials*, **36**(24): 2713-2733.
8) Blaga, A., Yamasaki, R.S. (1973). Mechanism of surface microcracking of matrix in glass-reinforced polyester by artificial weathering. *Journal of Materials Science*, **8**: 654–666.

9) Shen, W., Tang, C.Y., Tsui, C.P., Peng, L.H. (2002). Effects of two damage mechanisms on effective elastic properties of particulate composites. *Composites Science and Technology*, **62**(10-11): 1397-1406.

10) Mishnaevsky Jr., L.L. (2005). Automatic voxel-based generation of 3D microstructural FE models and its application to the damage analysis of composites. *Materials Science and Engineering* A, **407**(1-2): 11-23.

11) Sevostianov, I., Sookay, N.K., von Klemperer,C.J., Verijenko, V.E. (2003). Environmental degradation using functionally graded material approach. *Composite Structures*, **62**(3-4): 417-421.

12) McCann, D.M., Forde, M.C. (2001). Review of NDT Methods in the Assessment of Concrete and Masonry structures, *NDT & E International*, **34**(2): 71-84.

13) Maniatty, A.M., Zabaras, N.J., Stelson, K. (1989). Finite Element Analysis of Some Inverse Elasticity Problems, *Journal of Engineering Mechanics*, **115**(6): 1303-1317.

14) Maniatty, A.M., Zabaras, N.J. (1989). Method for Solving Inverse Elastoviscoplastic Problems, *Journal of Engineering Mechanics*, **115**(10): 2216-2231.

15) Cao, X., Sugiyama, Y., Mitsui, Y. (1998). Application of Artificial Neural Networks to Load Identification, *Computers and Structures*, **69**(1): 63-78.

16) Vaddadi, P., Nakamura, T., Singh, R.P. (2003). Inverse Analysis for Transient Moisture Diffusion through Fiber-reinforced Composites, *Acta Materialia*, **51**(1): 177-193.

17) Bernal, D., Gunes., B. (2001). A Flexibility-Based Approach for the Localization and Quantification of Damage: Application in a Benchmark Structure, *Structural Health Monitoring: The Demands and Challenges*, CRC Press, Florida.

18) Leung, C.K.Y., Yang, Z., Xu, Y., Tong, P., Lee, S.K.L. (2001). A New Fiber Optic-Based Method for Delamination Detection in Composites, *Structural Health Monitoring: The Demands and Challenges*, CRC Press, Florida.

19) Inada, T., Todoroki, A., Sugiya, T. (2001). Remote Structural Monitoring via Internet with Frequency Response Change Method, *Structural Health Monitoring: The Demands and Challenges*, CRC Press, Florida.

20) Chen, D.H., Nisitani, H. (1993). Detection of a Crack by Body Force Method, *Engineering Fracture Mechanics*, **45**(5): 671-685.

21) Ni, Y.Q., Ko, J.M. and Zhou, X.T. (2001) Damage Region Identification of Cable-Supported Bridges using Neural Network Based Novelty Detectors, *Structural Health Monitoring: The Demands and Challenges*, CRC Press, Florida.

22) Fares, N., Maloof, R. (1998). Crack Detection Characterization of Strain Sensing Grids, *International Journal of Solids and Structures*, **35**(22): 2861-2875.

23) Pool, K.V., Dharan, C. K. H., Finnie, I. (1986). Erosive wear of composite materials, *Wear,* **107**(1):1-12

24) Tewari, U.S., Harsha, A.P., Häger, A.M., Friedrich, K. (2003). Solid particle erosion of carbon fibre– and glass fibre–epoxy composites. *Composites Science and Technology*, **63**(3-4): 549-557.

25) Vaddadi, P., Nakamura, T., Singh, R., (2003). Transient hygrothermal stresses in fiber reinforced composites: a heterogeneous characterization approach. *Composites Part A: Applied Science and Manufacturing*, **34**(8): 719-730.

26) Azimi, H.R., Pearson, R.A., Hertzberg, R.W. (1995). Role of crack tip shielding mechanisms in fatigue of hybrid epoxy composites containing rubber and solid glass spheres. *Journal of Applied Polymer Science*, **58**(2): 449-463.

27) Bucknall, C.B., Dumpleton, P. (1987). Effects of loading history on fatigue crack growth in high density polyethylene and toughened poly (methyl methacrylate). *Polymer Engineering and Science*, **27**(2): 110-115.

28) Lowe, A., Kwon, O.H., Mai, Y.W. (1996). Fatigue and fracture behavior of novel rubber modified epoxy resins. *Polymer,* **37**(4): 565-572.

29) Figiel, L., Kaminski, M. (2003). Mechanical and thermal fatigue delamination of curved layered composites. *Computers and Structures*, **81**(18-19): 1865-1873.

30) Lafarie-Frenot, M.C., Ho, N.Q. (2006). Influence of free edge intralaminar stresses on damage process in CFRP laminates under thermal cycling conditions. *Composites Science and Technology*, **66**(10): 1354-1365.

31) Kashtalyan M, Soutis C. (2005). Analysis of composite laminates with intra- and interlaminar damage. Progress in Aerospace Sciences, **41**(2): 152-173.

32) Eselun, S.A., Neubert, H.D., Wolff, E.G. (1979). Microcracking effects on dimensional stability. In: National SAMPE technical conference (24^{th} conference). p. 1229-1309.

33) Cohen, D., Hyer, M.W., Tompkins, S.S. (1984). The effects of thermal cycling on matrix cracking and stiffness changes in composite tubes. In: National SAMPE technical conference (16th conference). p. 577-588.

34) Herakovich, C.T., Hyer, M.W. (1986) Damage-induced property changes in composites subjected to cyclic thermal loading. *Engineering Fracture Mechanics* ,**25**(5-6): 779-791.

35) Adams, D.S., Bowles, D.E., Herakovich, C.T. (1986) Thermally induced transverse cracking in graphite/epoxy cross-ply laminates. *Journal of Reinforced Plastics and Composites*, **5**(3): 152-169.

36) Kellogg, K.G., Kallmeyer A.R., Dutta, P.K. (2003). Influence of moisture and reduced-temperature thermal cycles on the izod notch toughness of a pultruded glass-fiber composite. *International Journal of Offshore and Polar Engineering*, **13**(3): 232-239.

37) Dutta, P.K., Kalafut, J.F., Lord, H.W. (1988). Response of advanced composite space materials to thermal cycling. In: Proceedings of the Engineering, Construction and Operations in Space. p. 506-517.

38) Tang, T., Hui, C.Y., Retsos, H.G., Kramer, E.J. (2005). Characterization of a fracture specimen for crack growth in epoxy due to thermal fatigue. *Engineering Fracture Mechanics*, **72**(5): 791-805.

39) Gurumurthy, C.K., Kramer, E.J., Hui, C.Y. (2001). Hydro-thermal fatigue of polymer interfaces. *Acta Materialia*, **49**(16): 3309-3320.

40) Finnie, I. (1995). Some reflections on the past and future of erosion, *Wear*, **186-187**(1): 1-10.

41) Shewmon, P., Sundararajan, G. (1983). The erosion of metals. *Annual Review of Materials Science*, **13**: 301-318.

42) Lawn, B.R. Erosion of wear of ceramics. (1980). In: Proceedings of Conference on Wear - Principles and Prevention, Australian Corrosion Assoc. and Australian Inst. of Metals, Sydney.

43) Usmani, S., S. Sampath. (1996). Ambient and Elevated Temperature Erosion Behavior of Duplex and Graded Ceramic Coatings, *Journal of Metals*, **48**(11): 51.

44) José R.T.B., Gansert, R., Sampath, S., Berndt, C.C., Herman, H. (2004). Solid Particle Erosion of Plasma Sprayed Ceramic Coatings. *Materials Research*, **7**(1)**:** 147-153.

45) Wang, B.Q., Geng, G.Q., Levy, A.V. (1990). Erosion-Corrosion of Thermal Spray Coatings. *Surface and Coatings Technology*, **43-44**(2): 859-874.

46) Karimi, A., Schmid, R.K. (1992). Ripple Formation in Solid-liquid Erosion. *Wear,* **156**(1):33-47.

47) Gutleber, J., Sampath, S., Usmani, S. (1997). Processing and thermal cycling effects on the erosion behavior of thermal barrier coatings. In: Thermal Spray: a United Forum for Scientific and Technological Advances, Indianapolis, USA. 15-18, September, p. 285-289.

48) Wellman, R.G., Deakin, M.J., Nicholls, J.R. (2005). The effect of TBC morphology on the erosion rate of EB PVD TBCs, *Wear*, **258**(1-4):349-356.

49) Wellman, R.G., Nicholls, J.R. (2004). On the effect of ageing on the erosion of EB-PVD TBCs, *Surface and Coatings Technology*, **177-178**:80-88.

50) Wellman, R.G., Dyer, A., Nicholls, J.R. (2004). Nano and Micro indentation studies of bulk zirconia and EB PVD TBCs, *Surface and Coatings Technology*, **176**(2):253-260.

51) Wellman, R.G., Nicholls, J.R. (2000). Some observations on erosion mechanisms of EB PVD TBCs, *Wear*, **242**(1-2):89-96.

52) Wellman, R.G., Nicholls, J.R. (2004). A Monte Carlo model for predicting the erosion rate of EB PVD TBCs, *Wear*, **256**(9-10):889-899.

53) Balasubramaniyam, S.S. (1998). Computational Modeling of Brittle Impact Erosion Mechanisms, MS Thesis, West Virginia University, Morgantown, West Virginia, USA.

54) Camacho, G.T., Ortiz, M. (1996). Computational Modeling of Impact Damage in Brittle Materials, *International Journal of Solids and Structures*, **33**(20-22):2899-2938.

55) Oliveira, B.F., Creus, G.J. (2004). An analytical–numerical framework for the study of ageing in fiber reinforced polymer composites. *Composite Structures*, **65** (3-4): 443-457.

56) White, J.R., Turnbull, A. (1994). Weathering of polymers—mechanisms of degradation and stabilization, testing strategies and modeling. *Journal of Materials Science*, **29**(3): 584–613.

57) Liao, K., Schultheisz, C. R., Hunston, D., and Brinson, L. C. (1998). Long-Term Durability of Fiber-Reinforced Polymer-Matrix Composite Materials for

Infrastructure Applications: A Review. SAMPE *Journal of Advanced Materials*, **30**(4): 3-40.

58) Mouzakis, D.E., Zoga, H., Galiotis, C. (2007). Accelerated environmental ageing study of polyester/glass fiber reinforced composites (GFRPCs). *Composites Part B: Engineering*, In Press.

59) Silva, M.A.G. (2007). Aging of GFRP laminates and confinement of concrete columns. *Composite Structures*, **79**(1): 97-106

60) Ranby, B. and Rabek, J.F. (1975). Photodegradation, Photo-Oxidation and Photostabilization of Polymers, John Wiley and Sons, London.

61) Wang, Y., Hahn, T.H. (2007). AFM characterization of the interfacial properties of carbon fiber reinforced polymer composites subjected to hygrothermal treatments. *Composites Science and Technology*, **67**(1): 92-101.

62) Collings, T.A., Stone, D.E.W. (1985). Hygrothermal effects in CFRP laminates: Strains induced by temperature and moisture. *Composites*, **16**(4): 307-316.

63) Chiou, P., Bradley, W.L. (1995). Effects of seawater absorption on fatigue crack development in carbon/epoxy EDT specimens. *Composites*, **26**(12)**:** 869-876.

64) Parker, B.M. (1986). Some effects of moisture on adhesive-bonded CFRP-CFRP joints. *Composite Structures*, **6**(1-3): 123-139.

65) Ramanujam, N., Vaddadi, P., T. Nakamura, and R. P. Singh, Interlaminar Fatigue Crack Growth of Cross-Ply Composites under Thermal Cycles. *Composite Structures*, under review.

66) Ramanujam, N., Nakamura, T., Urago, M. (2005). Identification of embedded interlaminar flaw using inverse analysis. *International Journal of Fracture*, **132**(2): 153-173.

67) Barkoula N.M., Papanicolaou, G.C., Krager-Kocsis, J. (2002). Prediction of the residual tensile strengths of carbon-fiber/epoxy laminates with and without interleaves after solid particle erosion. *Composites Science and Technology*, **62**(1): 121-130.

68) Hillery, R., (Ed.) 1996. Coatings for High Temperature Structural Materials, NRC report, National Academy Press.

69) Choi, S.R., Hutchinson, J.W., Evans, A.G., 1999. Delamination of multilayer thermal barrier coatings. *Mechanics of Materials*, **31**(7): 431.

70) Chen, X., Wang, R., Yao, N., Evans, G., Hutchinson, J.W., Bruce, R.W., 2003. Foreign object damage in a thermal barrier system: mechanisms and simulations. *Materials Science and Engineering A*, **352**(1-2): 221-231.

71) Frank, F.C., Lawn, B.R. (1967). On the Theory of Hertzian Fracture. In: Proceedings of the Royal Society of London. Series A, Mathematical and Physical Sciences, Volume 299, Issue 1458, p. 291-306

72) Lawn, B.R. (1980). Erosion and wear of ceramics. In: Proceedings of Conference on Wear-Principles and Prevention, Australian Corrosion Assoc. and Australian Inst. of Metals, Sydney, p. 1-7.

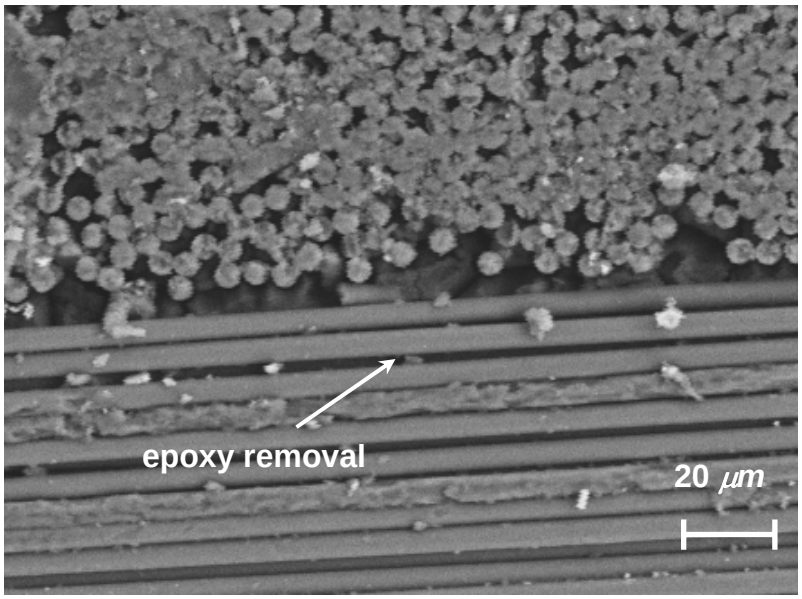

(a)

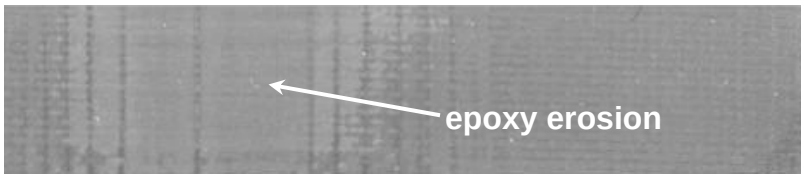

(b)

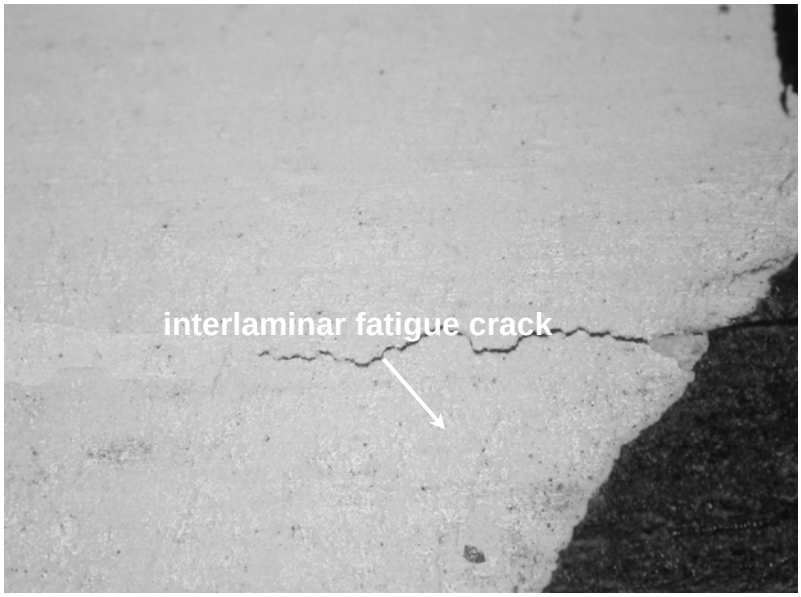

(c)

Fig. 1.1. Images of damaged carbon fiber-reinforced epoxy matrix due to (a) 1,000 hours of repeated moisture and UV radiation, (b) sand-blasting of composite surface and (c) 400 cycles of thermal load (ΔT = 120°C)

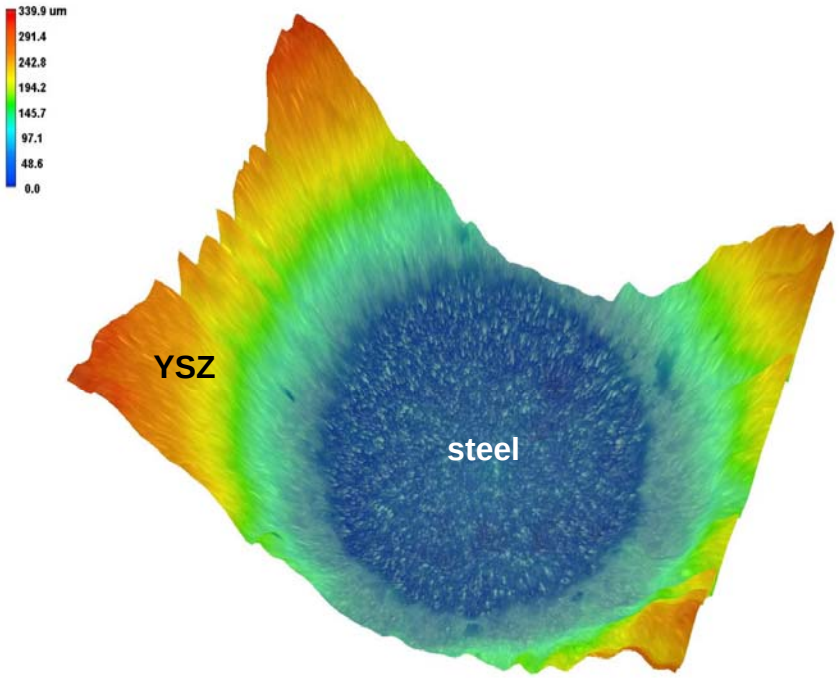

Fig. 1.2. Optical micrograph of YSZ coating surface after complete erosion.

2. Estimation of Damage Distribution in Fiber Reinforced Composites

2.1. Introduction

In the present work, damage is identified by adopting an inverse analysis based approach. Traditionally damages are evaluated using non-destructive evaluation (NDE) techniques such as radiography, ultrasonic, acoustic emissions, electrical, liquid penetration, conductivity, holography, radar and others. Although some are very effective, these procedures often require expensive equipments/tools and complex processes to quantify damages. In fact, such a method not only requires high capital costs but also large space, high operating costs and lengthy set-up time. Therefore, as the requirement to evaluate complex material/structure systems increases, it is essential to develop a simpler but still effective method, with an aid of appropriate post-processing scheme, regardless of measurement techniques.

In this study the damages are proposed to be estimated from strain measurements. The damages in a particular region of a composite are expected to affect the strain field since the degraded specimen would yield a compliant response as compared with the intact one due to loss of material. As mentioned earlier, matrix erosion in composite specimen occurs as a result of cyclic exposure to UV and moisture. The loss of matrix stiffness that occurs is very less (1-3%). However the loss of fiber confinements leads to limitation of load transfer to fibers. This phenomenon is expected to cause a similar effect as that of thinning, which is critical under bending rather than uniaxial tension. In fact, based on analytical calculations for drop in modulus due to thinning from laminate

theory, it is found that about 13% drop in modulus translates to 3% thinning [1].The details of the proposed approach for estimating the damage distribution is elaborately discussed below.

2.2. Inverse Analysis Approach

The physical responses of material can be defined or approximated by a set of model/state parameters. However, in complex material systems, often they are not directly measurable. In such cases, other observable/measurable parameters whose values have functional dependence on the model parameters must be used to estimate the unknowns [2]. Inverse analyses are generally required to connect such *indirect* measurements to the unknown parameters. Since there are various inverse procedures, it is essential to establish a *suitable* model and properly *tailor* it for given conditions. Here, the spatial variations of surface damage are the unknown model/state parameters while surface strains are assumed as the measurable parameters. In this study, two approaches were utilized to formulate the required strain-damage relations. One is based on polynomial functions and the other is based on the B-spline method. Then, an error objective function is minimized via multivariate Newton's method to estimate the damage distributions.

2.2.1. Representation of Surface Damage Model

Initially, to construct the approximate functions and verify the proposed inverse procedure, damaged models are constructed in finite element analyses. To conform with actual specimens to be tested, the model is chosen to be 8 layer cross-ply composite laminates. Although not shown here (due to space limitation), the proposed method was

also tested with homogeneous isotropic materials. The damage is assumed to exist on one side of the panel surfaces. In order to simulate such a damage condition, elements/material are discretely removed from finite element mesh. Here *comb-like* element/material deletions, as shown in Fig. 2.1(a), are performed to replicate the damaged state. The comb-like model has good resemblance to actual damage observed in real specimens. Alternatively, one may choose to signify the damage by varying elastic modulus of near-surface region. Such a model would also imitate weakening caused by the damage. However, it is emphasized that *choice of damage model* is not essential here since the purpose of study is to develop a method to estimate damage fields. In fact, other existing damage models can be readily implemented in the proposal procedure.

In order to quantify the distribution or variation of damage across the surface, the panel/beam is divided into several sectors as illustrated in Fig. 2.1(a). Here, S is the sector width while t denotes the panel thickness. The scheme is to identify the effective/average damage within each sector where individual strain measurement is assumed to be made. The present procedure can also accommodate other types of measurements including full-field strain measurements via an optical technique such as by speckle laser-interferometry or active sensors with radar interferometry (review in [3]). For large surfaces, these techniques may be more suitable than the ones with strain gages. If the strain field is obtained via a full-field measurement, the average strain within sector/section will be used as the measured parameter. In this initial study, the damage variation is only estimated along one axis with an assumption that it is nearly uniform through the width. The extension to more practical 3D panels (i.e., damage variation over two-dimensional surface) is discussed later.

Furthermore, if S / t ratio is large (> 4), there would be no effects from neighboring damage and the damage identification would be straightforward. Within each sector, the surface axial/longitudinal strain ε^{meas} is measured under pure bending condition. The bending is chosen over tension because of larger strain increases with surface damage [4]. The relative scale of sector width is an important factor. With the present approach, a suitable range of sector width-thickness ratio is ~1 < S / t < ~4. A smaller sector width would require too many measurements while a larger sector width would not yield precise damage variations.

2.2.2. Error Objective Function

Existence of surface damage influences deformation of specimens. Suppose the change in axial strain due to damage under bending is normalized as,

$$\Delta\tilde{\varepsilon} = \frac{\varepsilon^{meas} - \varepsilon_{o}}{\varepsilon_{o}} . \tag{2.1}$$

Here ε_{o} is a (reference) strain under same moment without damage. Next, a dimensionless damage/degradation parameter D is introduced to quantify the extent of average damage within a sector as shown in Fig. 2.1(b). For the current model, the parameter defines the average extent of damage through scaling with the material removal depth. Here no damage corresponds to D = 0 while D = 1 is set when the average material removal reaches single ply thickness. Thus, if the material removal occurs over the entire 1st layer (equals to t/8 for 8-ply laminates considered here), then D = 1. If the damage extends into the 2nd layer, then D > 1. Obviously, it is a simplistic definition of damage parameter and there are other various phenomenological definitions. However, it is reminded that this is just an operational designation used to establish the identification procedure. Furthermore

any *other types of damage models* can be readily accommodated in the procedure. In such cases, the parameter D would represent some effective value of damage that corresponds to average strain amplification within a sector. Note the maximum extents of damage are set differently in the two cross-ply laminates considered here (i.e., $D_{\max} = 0.50$ for $[0/90]_{2s}$ and $D_{\max} = 1.5$ for $[90/0]_{2s}$) based on damages to real specimens.

For panel-like structures, it is expected that a strain be influenced by nearby damage as illustrated in Fig. 2.1(a). Such influence diminishes as the distance to damage increases. Suppose the influence is limited to the damage at *three* closest sectors (opposite surface), then the normalized strain change at sector α is a function of three damage parameters as,

$$\Delta\widetilde{\varepsilon}_{\alpha} = \Delta\widetilde{\varepsilon}(D_{\alpha-1}, D_{\alpha}, D_{\alpha+1}) . \tag{2.2}$$

Here D_{α} is the effective damage at sector α, and $D_{\alpha-1}$ and $D_{\alpha+1}$ denote the effective damage in adjacent sectors, respectively. The above assumption should be valid as long as $S/t > \sim 1$. For a smaller S/t, influences from other neighboring sectors may need to be included.

The unknown damage parameters are sought by minimizing the error between measured strains and strains corresponding to estimated damage. Suppose $D_{\alpha-1}^{est}, D_{\alpha}^{est}, D_{\alpha+1}^{est}$ are the estimated damage in the three sectors, then the corresponding estimated/approximated strain at sector α is expressed as,

$$\varepsilon_{\alpha}^{est}(\boldsymbol{D}) = \varepsilon_{o}[1 + \Delta\widetilde{\varepsilon}_{\alpha}(D_{\alpha-1}^{est}, D_{\alpha}^{est}, D_{\alpha+1}^{est})] . \tag{2.3}$$

Here the vector $\boldsymbol{D}$ contains the unknown damage parameters at sectors. The goal is to find damage parameters that yield the minimum error between the *estimated* and *measured*

strains across the entire model. The error objective function of sector α and the global function can be defined as,

$$\phi_\alpha(\boldsymbol{D}) = \frac{\varepsilon_\alpha^{est}(\boldsymbol{D}) - \varepsilon_\alpha^{meas}}{\varepsilon_o} = 1 + \Delta\widetilde{\varepsilon}_\alpha(\boldsymbol{D}) - \frac{\varepsilon_\alpha^{meas}}{\varepsilon_o} \quad \text{and} \quad \Phi(\boldsymbol{D}) = \sum_{\alpha=1}^{n} \left|\phi_\alpha(\boldsymbol{D})\right| . \tag{2.4}$$

The minimization of the global objective function will lead to the best estimates of damage parameters over *n* sectors.

2.2.3. Formulations of Damage-Strain Relations

In order to identify the damage distribution effectively, a functional formulation to approximate the damage-strain relation is necessary. In fact, the development of suitable damage-strain relations is the *focal* point of proposed procedure. Without such formulations, an iterative scheme to find the unknown parameters would place a great burden in the computations. For an example, it would require step by step finite element analysis with new mesh constructed each time. Clearly, that would be prohibitively expensive and make the method impractical. In this work, many different forms were tried and examined prior to selecting the two approaches described next. They are the quadratic formulation and the B-spline method, which can be utilized depending upon the extent of damage.

A. Quadratic Formulation Approach

Suppose the strain increase due to existence of damage is expressed in terms of a series of polynomials, then (2.2) can be expressed as,

$$\Delta\widetilde{\varepsilon}_\alpha = \sum_{i=\alpha-1}^{\alpha+1} a_i D_j + \sum_{i=\alpha-1}^{\alpha+1} \sum_{j=\alpha-1}^{\alpha+1} b_{ij} D_i D_j + \ldots . \tag{2.5}$$

Here, a_i and b_{ij} are the coefficients that depend on material properties as well as geometrical parameters such as sector width/thickness ratio. In the above equation, the first summation represents the direct effect while the second double summations express the coupling as well as nonlinear effects of damage in sectors. Our study showed that the nonlinear and coupling effects beyond the second order terms were minimal when the damage is contained within the first surface ply. Then, the strain increase is shown in a quadratic form as,

$$\begin{aligned}\Delta\tilde{\varepsilon}_\alpha = {} & c_1 D_\alpha + c_2 (D_\alpha)^2 + c_3 D_{\alpha-1} + c_4 D_\alpha D_{\alpha-1} + c_5 (D_{\alpha-1})^2 \\ & + c_6 D_{\alpha+1} + c_7 D_\alpha D_{\alpha+1} + c_8 D_{\alpha-1} D_{\alpha+1} + c_9 (D_{\alpha+1})^2 \end{aligned} . \tag{2.6}$$

Here c's are the coefficients (re-expressed for a_i and b_{ij}) to be determined. The above expression can be further simplified. First, the coupling effects between $D_{\alpha\text{-}1}$ and $D_{\alpha+1}$ may be ignored since these sectors are farther apart (i.e., $c_8 = 0$). Second, if all sector widths were set equal, the contributions from $D_{\alpha\text{-}1}$ and $D_{\alpha+1}$ should be symmetric (i.e., $c_3 = c_6$, $c_4 = c_7$ and $c_5 = c_9$). With these considerations, the strain change in terms of damage simplifies to,

$$\begin{aligned}\Delta\tilde{\varepsilon}_\alpha = {} & c_1 D_\alpha + c_2 (D_\alpha)^2 + c_3 (D_{\alpha-1} + D_{\alpha+1}) + \\ & c_4 D_\alpha (D_{\alpha-1} + D_{\alpha+1}) + c_5 [(D_{\alpha-1})^2 + (D_{\alpha+1})^2] \end{aligned} . \tag{2.7}$$

The coefficients in (2.7) can be determined from some known relations between the damage and strains. Here singular value decomposition method (SVD) is utilized after strains are obtained under various prescribed damage conditions. The SVD is an effective technique to diagnose or solve problems involving multiple equations or matrices that are either singular or numerically close to singular in parametric data modeling [5]. This method is used in many problems including investigations of ill-conditioned structures

where small perturbations result in magnified errors [6], optimizations of measurement locations for dynamic testing [7], and spatial parameter estimations of vibrating structures [8].

In (2.7), the strain change due to damage is expressed as a function of three parameters, D_α, $D_{\alpha\text{-}1}$ and $D_{\alpha+1}$. In order to reduce the number of calculations required for the parametric study to determine the coefficients, the effects of $D_{\alpha-1}$ and $D_{\alpha+1}$ are evaluated under $D_{\alpha-1} = D_{\alpha+1}$ conditions. Such an assumption reduces the computational requirements significantly since the study can be carried out for two parameters, D_α and $D_{\alpha\pm1}$. To make sure this approximation does not lead to large errors, (2.7) is used to compute $\Delta\widetilde{\varepsilon}_\alpha$ under the worst conditions (e.g., unlikely case of $D_{\alpha-1} = 0$ and $D_{\alpha+1} = D_{\max}$). The error in the computed strain increase was less than 2%. Based on these assumptions, parametric computations with different combinations of D_α and $D_{\alpha\pm1}$ are performed with finite element models. In each case, $\Delta\widetilde{\varepsilon}_\alpha$ is obtained from computed axial strain at one sector. Suppose a total of m simulations (described later) are carried out with prescribed $D_\alpha{}^i$ and $D_{\alpha\pm1}{}^i$ (where $i = 1, 2, \ldots, m$), then the resulting relations between the damage and strain can be expressed in a matrix form as,

$$\begin{bmatrix} D_\alpha{}^1 & (D_\alpha{}^1)^2 & 2D_{\alpha\pm1}{}^1 & 2D_\alpha{}^1 D_{\alpha\pm1}{}^1 & 2(D_{\alpha\pm1}{}^1)^2 \\ D_\alpha{}^2 & (D_\alpha{}^2)^2 & 2D_{\alpha\pm1}{}^2 & 2D_\alpha{}^2 D_{\alpha\pm1}{}^2 & 2(D_{\alpha\pm1}{}^2)^2 \\ \vdots & \vdots & \vdots & \vdots & \vdots \\ D_\alpha{}^m & (D_\alpha{}^m)^2 & 2D_{\alpha\pm1}{}^m & 2D_\alpha{}^m D_{\alpha\pm1}{}^m & 2(D_{\alpha\pm1}{}^m)^2 \end{bmatrix} \begin{bmatrix} c_1 \\ c_2 \\ c_3 \\ c_4 \\ c_5 \end{bmatrix} = \begin{bmatrix} \Delta\widetilde{\varepsilon}_\alpha^1 \\ \Delta\widetilde{\varepsilon}_\alpha^2 \\ \vdots \\ \Delta\widetilde{\varepsilon}_\alpha^m \end{bmatrix}. \tag{2.8}$$

Suppose the above is expressed as $\widetilde{\boldsymbol{D}}\,\boldsymbol{c} = \boldsymbol{e}$, where $\widetilde{\boldsymbol{D}}$ is a matrix containing known prescribed damage parameters, $\boldsymbol{c}$ is the unknown coefficient vector and $\boldsymbol{e}$ is the vector

containing normalized strain changes. In general, with five unknown components, only five independent equations are sufficient to determine the coefficients. However, since (2.7) is an approximated relation, $\boldsymbol{c}$ is not unique. Thus, the aim is to determine *best fits* for $\boldsymbol{c}$ components so that good strain approximations can be obtained for wide range of extents of damage. For $[0/90]_{2s}$ panels (with $D_{\max} = 0.5$), D_{α} and $D_{\alpha\pm1}$ are varied between 0 and 0.5 with increments of 0.125 (i.e., $m = 25$ combinations). Essentially, an over-determined system of equations minimizes the error arising from the approximated function (2.7).

After parametric computations, the singular value decomposition (SVD) method is utilized. First, since $\widetilde{\boldsymbol{D}}$ is not a square matrix (i.e., 25×5), it is decomposed into a column-orthogonal matrix $\boldsymbol{U}$, a square diagonal matrix $\boldsymbol{S}$, and transpose of a square orthogonal matrix $\boldsymbol{V}$ as $\widetilde{\boldsymbol{D}} = \boldsymbol{USV}^T$ (i.e., singular decomposition). Here, the diagonal components of matrix $\boldsymbol{S}$ are the non-negative singular values of matrix. Once these matrices are computed, the generalized inverse of $\widetilde{\boldsymbol{D}}$ can be obtained as $\widetilde{\boldsymbol{D}}^{+} = \boldsymbol{VS}^{-1}\boldsymbol{U}^T$. With this matrix, the coefficient vector is computed as $\boldsymbol{c} = \widetilde{\boldsymbol{D}}^{+}\boldsymbol{e}$ [5]. The generalized inverse matrix $\widetilde{\boldsymbol{D}}^{+}$ is obtained with an IMSL subroutine [9].

B. B-spline Approach

When the damage extends beyond the first surface ply, the strains suddenly change and they cannot be approximated by polynomial formulations accurately. Usually the discontinuity in the slopes arises as the damages enter into the second ply. The damage extension into multiple plies may occur when panels are subjected to mechanical contacts or repeated low-energy impact (e.g., sand blasting). In order to formulate the

damage-strain relations in such cases, a so-called *basis* or B-spline method was adopted that is a powerful technique in multidimensional shape illustration. The adoption of B-spline for the current problem is described below.

The foundation of B-spline curve lies is in a Bezier curve that is characterized by a set of control points and basis functions. The control points form a control polygon and the Bezier curve lies within the *convex hull* of the polygon. Note that control points do not necessarily lie on the curve but they are expressed by linear combinations of coefficients in a polynomial function. They have associated weighting or basis functions, which define the influence of the respective control points. In order to accommodate sharp changes in slope, B-splines are formed by combining Bezier segments. Here a knot vector is introduced to join adjacent Bezier segments. By changing the values of knot vector, one can adjust the length of a Bezier segment. In the present problem, a tensor product B-spline surface is established to express the strain change due to damage as,

$$\Delta\tilde{\varepsilon}(D_{\alpha-1}, D_{\alpha}, D_{\alpha+1}) = \sum_{i=1}^{n}\sum_{j=1}^{m} N_i(D_{\alpha}) N_j(D_{\alpha\pm1}) P_{ij}\,. \tag{2.9}$$

Here, N_i are the basis functions and P_{ij} are the control points in the coordinate that represents the strain change, and n and m are the numbers of control points along the dimensions of D_{α} and $D_{\alpha\pm1}$, respectively. In this study, they are set as $n = m = 6$ while the order of basis functions are set as quadratic. As in the quadratic formulation, the effects of $D_{\alpha-1}$ and $D_{\alpha+1}$ are approximated from $D_{\alpha\pm1}$. With these choices, each of the basis functions (N_1~ N_6) can be defined as,

$$N_i(D_\alpha) = \frac{D_\alpha - D_\alpha{}^i}{D_\alpha{}^{i+2} - D_\alpha{}^i} N_i{}^*(D_\alpha) + \frac{D_\alpha{}^{i+3} - D_\alpha}{D_\alpha{}^{i+3} - D_\alpha{}^{i+1}} N_{i+1}{}^*(D_\alpha)$$

$$\text{where } N_i{}^*(D_\alpha) = \frac{D_\alpha - D_\alpha{}^i}{D_\alpha{}^{i+1} - D_\alpha{}^i} N_i{}^o(D_\alpha) + \frac{D_\alpha{}^{i+2} - D_\alpha}{D_\alpha{}^{i+2} - D_\alpha{}^{i+1}} N_{i+1}{}^o(D_\alpha). \tag{2.10}$$

$$\text{where } N_i{}^o(D_\alpha) = \begin{cases} 1 & \text{for} \quad D_\alpha{}^i \le D_\alpha \le D_\alpha{}^{i+1} \\ 0 & \text{for} \quad D_\alpha{}^i > D_\alpha \text{ or } D_\alpha > D_\alpha{}^{i+1} \end{cases}$$

Here $D_\alpha{}^i$ represents damage at i_{th} knot point and it ranges i = 1~9. The basis functions for $D_{\alpha\pm1}$ are expanded in a similar way. The knot points are selected so that the sudden slope changes can be modeled accurately. For $[90/0]_{2s}$ panels where the maximum damage is set as $D_{\max}$ = 1.5 (based on actual damaged specimens), the knot points are chosen as $D_\alpha{}^i = D_{\alpha\pm1}{}^i = (0, 0, 0, 0.98, 1.02, 1.25, 1.50, 1.50, 1.50)^T$. Since the degree of the basis functions is 2, the B-spline surface is C^2 continuous everywhere inside the domain. When $D_\alpha{}^{i+3} = D_\alpha{}^{i+1}$ (for $1.25 \le D_\alpha < 1.5$), then singularities appear in (2.10). In such cases, the second term of RHS of the first equation is set zero. Model finite element simulations are performed by setting D_α and $D_{\alpha\pm1}$ at 11 different values as 0, 0.2500, 0.5000, 0.7500, 1.0000, 1.0625, 1.1250, 1.1875, 1.2500, 1.3750, 1.5000 with total of 121 combinations.

2.2.4. Multivariate Newton's Method

The inverse analysis techniques can be categorized into ones that involve numerical differentiations or ones based upon iterative numerical integrations. The methods based upon differentiations often have an order of magnitude faster convergence than that with numerical integrations [10]. The multivariate Newton's method is a simple but efficient multidimensional root finding method, which falls into the former category. In this approach, the objective is to minimize the error functions in (2.4). First, the local error functions ϕ_α are expanded using Taylor series as,

$$\phi_\alpha(\boldsymbol{D}+\delta\boldsymbol{D}) = \phi_\alpha(\boldsymbol{D}) + \sum_{\beta=1}^{n} \frac{\partial \phi_\alpha}{\partial D_\beta}\delta D_\beta + O(\delta \boldsymbol{D}^2)\,. \tag{2.11}$$

A minimization of the error functions $\phi_\alpha(\boldsymbol{D})$ can be achieved when each component is minimized in the neighborhood of $\boldsymbol{D}$. The higher order terms including $O(\delta\boldsymbol{D}^2)$ are ignored giving a linear approximation for $\phi_\alpha(\boldsymbol{D}+\delta\boldsymbol{D})$. If $\phi_\alpha(\boldsymbol{D}+\delta\boldsymbol{D})$ is set to zero (theoretical minimum), a system of simultaneous linear equations appear as,

$$\phi_\alpha(\boldsymbol{D}) + J_{\alpha\beta}\delta D_\beta = 0 \qquad \text{where} \qquad J_{\alpha\beta} \equiv \frac{\partial \phi_\alpha}{\partial D_\beta}\,. \tag{2.12}$$

In the above, $J_{\alpha\beta}$ is the Jacobian matrix and summation over β is assumed. This equation is solved via iterations by adding correction vector $\delta D_\alpha = -(J_{\alpha\beta})^{-1}\phi_\beta$ to the estimated damage parameters.

In general, computations of Jacobian matrix are cumbersome and difficult. However, in our proposed damage-strain models, the equations are *recursive* and their non-zero components can be conveniently expressed in a banded matrix form. For the quadratic formulation discussed previously, the components of Jacobian matrix using Equations (2.4) and (2.7) are,

$$\begin{aligned} J_{\alpha(\alpha-1)} &= c_3 + c_4 D_\alpha + 2c_5 D_{\alpha-1} \\ J_{\alpha\alpha} &= c_1 + 2c_2 D_\alpha + c_4(D_{\alpha-1} + D_{\alpha+1}) \\ J_{\alpha(\alpha+1)} &= c_3 + c_4 D_\alpha + 2c_5 D_{\alpha+1} \end{aligned}\,. \tag{2.13}$$

For the B-spline approximation shown in (2.9), they are,

$$J_{\alpha(\alpha-1)} = \frac{1}{2}\sum_{i=0}^{n}\sum_{j=0}^{m} N_i(D_\alpha)N'_j(D_{\alpha-1})P_{ij}$$

$$J_{\alpha\alpha} = \frac{1}{2}\sum_{i=0}^{n}\sum_{j=0}^{m} N'_i(D_\alpha)N_j(D_{\alpha-1})P_{ij} + \frac{1}{2}\sum_{i=0}^{n}\sum_{j=0}^{n} N'_i(D_\alpha)N_j(D_{\alpha+1})P_{ij} \quad . \tag{2.14}$$

$$J_{\alpha(\alpha+1)} = \frac{1}{2}\sum_{i=0}^{n}\sum_{j=0}^{m} N_i(D_\alpha)N'_j(D_{\alpha+1})P_{ij}$$

In the above, $N'_i(D_\alpha)$ is the derivative of basis function with respect to D_α expanded as,

$$N'_i(D_\alpha) = \frac{2}{D_\alpha^{i+2} - D_\alpha^{i}} N_i^{*}(D_\alpha) + \frac{2}{D_\alpha^{i+3} - D_\alpha^{i+1}} N_{i+1}^{*}(D_\alpha) \ . \tag{2.15}$$

If (2.15) is singular, then the same procedure as described for the basis function is applied. The inverse of Jacobian matrix is obtained using the lower triangle-upper triangle (LU)

decomposition technique [5]. The iterations are carried out until convergence is obtained as $\Phi(\boldsymbol{D})$ < TOL. TOL is set 10^{-7} in the quadratic formulation and 10^{-3} in the B-spline method, requiring 5-8 iterations. The flowchart of the iterative method is illustrated in Fig. 2.2.

2.3. Verification Analyses

2.3.1. Models with Surface Damages

Prior to implementing the proposed procedure in real tests, its feasibility is examined in a simulation study. Since the exact or prescribed damage is known here, it can be used to test the accuracy. In fact, the verification study is a critical part of establishment of any novel procedures. Here, surface damaged 8-ply $[0/90]_{2s}$ as well as $[90/0]_{2s}$ composite laminates are considered. The two laminates are essentially the same cross-plies with the difference of 90^o rotation. Under bending load, $[0/90]_{2s}$ panel exhibits

much stiffer response than that of $[90/0]_{2s}$ panel. The two arrangements were considered in the simulation study as well and in the actual tests to verify the proposed method.

In each ply, the mechanical property is assumed to be transversely isotropic, and their linear elastic properties are E_L = 150GPa, E_T = 9.0GPa, ν_{LT} = 0.330, ν_T = 0.176 and G_{LT} = 5.0GPa, where, the subscript '*L*' indicates the fiber direction and the subscript '*T*' indicates the transverse direction.

These values correspond to the properties of actual specimens tested (IM7/997 composites). The schematic in Fig. 2.3(a) represents the $[0/90]_{2s}$ composite laminate subjected to remote bending with damage on one surface layer and strain measurements on the other surface. To determine the distribution, the panel is divided into 20 sectors, denoted as $S_1, S_2, \ldots, S_{20}$. Initially the sector width-thickness ratio is set as S/t = 1.67 and later set as S/t = 3.33. An enlarged section of the lower plies is shown in Fig. 2.3(b). Here, 0^o plies have fibers along the axial/longitudinal direction while 90^o plies have fibers oriented along the out-of-plane direction. A comb-like model represents the damage as shown in the finite element mesh of damaged section in Fig. 2.3(c). An automatic mesh-generator code was developed to construct such a model. In the mesh, smaller elements are placed near the damaged region to resolve higher stresses. Each model contains approximately 90,000 generalized plane strain four-noded isoparametric elements.

2.3.2 Computations of Coefficients in Damage-Strain Relations

A. Quadratic Formulation for $[0/90]_{2s}$ Model

Prior to estimating the damage distribution, the coefficients in (2.7) must be determined. Here, they are obtained by a separate finite element analysis. In Fig. 2.4, the three-dimensional surface plot represents the effect of damage on strain measurement in

sector α under different combinations of D_α and $D_{\alpha\pm1}$ (for $S/t = 1.67$). Since this relation assumes the effects of damage to arise from three nearest sectors, a simplified model is utilized to reduce the modeling and computational efforts. Rather than the entire model shown in Fig. 2.3, a smaller half-model shown in the Fig. 2.4 (inset) is considered. The model assumes a uniform damage within each sector. The longitudinal strain ε_α is computed for various combinations of damage at sectors α and $\alpha\pm1$ as shown in Fig. 2.4. The maximum extent of damage is set at $D_{\max} = 0.5$ and the damage parameters D_α and $D_{\alpha\pm1}$ are each varied in increments of 0.125 with total of 25 combinations. The coefficients obtained via the singular value decomposition method are listed in Table 2.1.

B. B-spline Approach for $[90/0]_{2s}$ Model

When damage extends into the second layer from the surface and the damage-strain relation possesses discontinuous slopes, the quadratic formulation is ineffective and instead the B-spline method is utilized. For this analysis, $[90/0]_{2s}$ laminates are chosen since a rapid increase in strain can be observed if the damage penetrates into the second 0^o layer (not so with $[0/90]_{2s}$ laminates). In the analysis, the maximum damage is set at $D_{\max} = 1.5$ (other values can be easily accommodated). To determine the control points in the B-spline and corresponding strains, computations are carried out with 121 varying combinations of D_α and $D_{\alpha\pm1}$ as described earlier. Fig. 2.5 shows the computed strains for different combinations of D_α and $D_{\alpha\pm1}$ with the width-thickness ratio of $S/t = 3.33$. As expected, the surface exhibits kinks along $D_\alpha = D_{\alpha\pm1} = 1.0$ when damage enters into the second layer. With these results, the control points for surface fitting are obtained through the least square minimization [11] as listed in Table 2.2.

The accuracies of these empirical representations of strains are examined for sample cases. For the quadratic formulations, the approximated strain from (2.7) is shown with a solid line in Fig. 2.6 (a). In the same figure, independently computed strains from the finite element calculations are shown with circles. To be objective, this combination of D_α and $D_{\alpha\pm1}$ is not used in the determinations of coefficients in (2.7). The agreements are very good. Computations from other cases showed the strains approximated via (2.7) to be always within 2% of independently calculated strain. A similar plot is shown for the B-spline model in Fig. 2.6 (b). Here the accuracy is somewhat worse near the kink (i.e., $D_\alpha = 1.0$) although the approximations at other points match well with the independently computed values. Note that B-spline method is a more versatile approach and it works well also when the damage is contained in the first layer. However, as compared to the quadratic formulation, the B-spline procedure is more complex to set-up and requires additional computations. Therefore in cases when the damage is contained to the surface ply (generally observed for environmentally degraded composites), the quadratic formulation is more effective.

2.3.3. Simulated Damage in Flexurally Stiff $[0/90]_{2s}$ Model

In order to examine the accuracy of present procedure with known solutions, simulations are carried with artificially imposed damage across the surface of $[0/90]_{2s}$ laminates. Fig. 2.7(a) shows the simulated strain measurements across the sectors and a schematic of corresponding damaged model. The magnitudes of damage in sectors are *randomly* prescribed between 0.03~0.25. Using these strains as input, the multivariate Newton-Raphson method is performed to estimate the damage distribution with the quadratic formulation. The *estimated* damage distribution as well as the *exact/imposed*

damage distribution is shown in Fig. 2.7(b). In each sector, the estimated results (shaded circles) nearly overlap the exact results (diamonds) which imply excellent agreements. To illustrate the significance of including the nonlinear as well as coupling effects from the neighboring damage, estimates are also made from a linear relation (shown with empty circles in Fig. 2.7(b)). Here a simple strain-damage relation of $\Delta\tilde{\varepsilon}_\alpha = c^* D_\alpha$ is assumed where coefficient c^* (= 0.316) is obtained from a single calculation with $D_\alpha = D_{\alpha\pm1} = 0.25$. Although the linear model still captures the trend of damage, it does not yield accurate estimates. Although not shown here, other cases were tested where damage is prescribed *randomly over the entire surface* (instead of keeping them uniform within each sector). The estimated damage in each sector was very close to the *average* of prescribed damage for given sector. Other models also confirmed the accuracy of the proposed procedure to support its robustness to estimate the damage distribution.

To observe the effects of sector width, the method is examined in a model with a different relative sector width ($S/t = 3.33$), which matches with the actual measurements. As in the previous model, the coefficients in (2.7) are determined from calculations with various combinations of D_α and $D_{\alpha\pm1}$ and the SVD method. The computed coefficients are listed in Table 2.1. Due to its larger sector width, lesser effects of the adjacent sector (i.e., smaller c_3 and c_5) as well as weaker coupling effect (i.e., smaller c_4) are observed as compared to those from the $S/t = 1.67$ model. In the simulation, damage is again distributed randomly and resulting axial strains are shown in Fig. 2.8(a). Using these strains as inputs, the Newton-Raphson iterations are carried out to estimate damages. The estimated damages across sectors are shown in Fig. 2.8(b). The agreements between the exact and estimated results are better than the previous model as they are essentially

identical at each sector. Although not included in the figure, estimates based on a linear model (with $c^* = 0.322$) exhibited better approximations than those from short sector width. This was expected, since the damage influences from adjacent sectors are diminished due to larger relative sector width. Simulations with other sector width model showed that the present procedure performs well even with the relative sector width as small as $S/t = 1$. Such a sector width may be appropriate for physically thick composite panels with full-field strain measurements (e.g., optical method).

2.3.4. Simulated Damage in Flexurally Compliant $[90/0]_{2s}$ Model

For the verification, similar tests are carried out for $[90/0]_{2s}$ laminates containing severe damage ($D > 1.0$). Again the choice of this ply arrangement was made to capture a large strain jump when damage penetrates into the second layer at some sectors. Figure 2.9(a) shows the variation of computed strains across the sectors with randomly prescribed damage as illustrated inset. Here, the sector width-thickness ratio is set as $S/t = 3.33$ to conform to the actual specimens. Using the computed strains as input, the multivariate Newton-Raphson method with B-spline representation of strains is performed. The estimated damage in each sector as well as the exact/prescribed damage are shown in Fig. 2.9(b). The excellent agreements across various sectors support the accuracy of proposed procedure with the B-spline for laminates that exhibit damage beyond the outermost ply.

2.4. Damage Characterization in Real Composite Panels

Upon successful verification of the proposed damage identification method, it is implemented in real composite laminates possessing surface damage. The composites

used in the experiments are commercially fabricated 8-ply laminates of IM7/997 carbon-fiber reinforced epoxy laminates donated by Cytec Fiberite Inc. The fiber diameter is 5μm with volume fraction of 58%. The material properties follow those noted in Verification Section. The IM7/997 system is under development for application to aerospace and rotorcraft structures. The specimens were machined to average dimensions of 140mm×12.7mm×1.2mm. The specific details of imposed damage conditions are described next.

2.4.1. Environmental Degradation Experiments

Composite specimens were subjected to environmental degradation under cyclic periods of UV radiation (with an irradiance level of 0.68 W/m^2) and moisture (relative humidity: 100%) for about 2,000 hours (close to 3 months) in an accelerated environmental chamber (QUV/Se weathering chamber, Q-Panel Lab Products). Physically, the specimens become compliant due to erosion of epoxy matrix that lowers load transfer mechanisms among fibers. From SEM micrographs, it was found that the erosion can be more than 30μm deep [4]. In this study, the goal is to estimate the distribution of surface damage. Thus, in order to generate *non-uniform* surface damage, aluminum sheets are used to partially cover surface area of specimens. The covered areas are changed *irregularly* to produce varying damage on the surface layer. At the end of exposure, uneven degradations across the surface are visible. Here only one side of panel is exposed while the other side was kept undamaged with a covered aluminum sheet. The detailed study to correlate the *exposed time* to the *damage distribution* will be conducted in future.

2.4.2. Strain Measurements under Four-Point Bending

In order to produce a constant bending through the measured segment, four-point loading is carried out as shown in Fig. 2.10(a). Here, the loading span and support span are set as 60mm and 120 mm, respectively, as illustrated in Fig. 2.10(b). These dimensions follow the standards for performing flexural tests on composites specified in ASTM D6272-02 [12]. In order to measure axial strains from multiple gages, so-called "strip strain gage" is utilized which contains equally spaced 10 gages in a strip. These gages circumvent problems of unequal-spacing and misalignment caused by bonding of several gages. The 10-gage strips (Vishay Micro Measurements Inc.) are available with either 2mm or 4mm spacing. Although both types were tried, the results are reported with the 4 mm spacing since the measurements with 2mm spacing were more difficult. Fig. 2.10(c) shows a composite panel with a strip gage. The initial resistance of each gage is 120Ω. The gage is bonded onto undamaged side of panel with two-component 100% solid epoxy system (M-Bond AE-10) with a curing agent type 10 (24 hrs) supplied by Vishay Micro Measurements Inc. Prior to testing environmentally degraded specimens, strains are measured on *undegraded* model under bending. This was carried out to calibrate the reference strain without damage and to ensure uniformity in strains across gages in a strip. From this test, the reference strain is measured as $\varepsilon_o = 9.18\, M/(E_L t^2 b)$, where M is the bending moment and b is the width of specimen, for $[0/90]_{2s}$ specimen. The deviations among 10 gages are less than ±0.5% at M = 0.6 N·m, which gives sufficient strains ($\varepsilon \sim 2\times10^{-3}$) without large panel curvature. Although the reported measurements are made under tension, the loading under compression yielded similar

results with or without damages. For $[90/0]_{2s}$ specimen, the reference strain was $\varepsilon_o = 1.02 M/(E_T t^2 b)$.

2.4.3. Damage Identification for $[0/90]_{2s}$ Panels

Environmentally degraded $[0/90]_{2s}$ panels are loaded under bending and axial strains are measured at M = 0.6 N·m. The increases in strains due to damage are normalized with the reference strain as listed in Table 2.3 for two specimens. The consistent increases of strain (up to 6.3%) imply the presence of damage. For each specimen, the damage distribution is estimated through the multivariate Newton-Raphson method using the strain-damage relation via the quadratic formulations. Fig. 2.11 shows the estimated damage distributions across 10 sectors for the two specimens. In each specimen, the estimated damage is not distributed uniformly. Since the exposure to environmental degradation was made inconsistently, one cannot make correlations between the exposed conditions and damage. However, in this proof of concept, these tests clearly support the effectiveness of proposed method to detect damages.

The error size of estimated damage is dictated by the accuracies of strain measurements as well as property variation in composite panel itself. Since systematic measurements are yet to be carried out to define the precise error bound, it is approximated from the strain measurements on undamaged specimens. Generally, they exhibited 0.5% variations about the mean and this value was assumed for all measured strains. These errors translate to $\Delta D^{\text{error}} \cong \pm 0.02$ (see Fig. 2.6(a) for relation) in the damage estimations. Obviously, these errors are larger than the damage parameters themselves at some sectors. However, since it is more critical to estimate *large* damage, relatively large size of the error bound should be still acceptable.

2.4.4. Damage Identification for $[90/0]_{2s}$ Panel

In addition to environmental degradation, composite panels can be damaged through direct impact and wear by abrasive particles. In such cases, damages may extend beyond the surface ply. To validate the applicability of proposed method under such conditions, physically damaged $[90/0]_{2s}$ panels were also tested. The panel with these ply orientations are chosen over $[0/90]_{2s}$ panels (essentially the same panel with 90^o rotation) because damage extension into the stiffer second 0^o ply produces large strain changes (not with $[0/90]_{2s}$ panels).

To produce damage/wear on specimens, an abrasive sand/grit-blasting is utilized. Although the resulting damage depends on various factors including the type of abrasive, the duration of contact and contact pressure, the detailed effects are not studied here. The sand blasting is a realistic representation of material removal due to abrasive wear phenomena that may occur in severe environments. It was carried out with a spray gun in a blasting chamber that directs silicon carbide (SiC) particles through 7mm diameter nozzle. Non-uniform surface damage along the specimen length was made artificially by altering the spray durations while along the specimen width, the damage was made nearly uniformly. Optical micrographs of sand-blasted specimen is shown in Fig. 2.12(a) for Specimen C. Near sector 4, the first 90^o ply was completely removed as evident from the exposed second 0^o ply. Near sector 7, the first ply was only partially removed and the micrograph still shows the 90^o fibers.

A strip strain gage is bonded onto the undamaged surface and strains are measured under four-point bending. The normalized strain increases are listed in Table 2.3 and shown in Fig. 2.12(b). Based on measurements without damage, a similar error

bound for strain as $[0/90]_{2s}$ panels is assumed (±0.5%). Here, sectors 3~5 exhibits higher strains due to larger damage, which are consistent with the micrographic observations, A separate $[90/0]_{2s}$ panel (Specimen D) was also artificially damaged by another method. Since the objective of present study is to prove the applicability of proposed method, damage was not introduced systematically. Subsequent studies will inspect the material removal and damage relations. The measured strains across 10 different sectors are listed in Table 2.3 and shown in Fig. 2.12(b). Compared to Specimen C, the magnitudes of strain increases are generally lower.

With these measured strains, distributions of surface damage are estimated with the inverse analysis using the B-spline representation for strain and damage. The results are shown in Fig. 2.13. As expected, a large damage ($D > 1$) is estimated near the sectors 3~5 for Specimen C, which suggests the damage penetration to the second layer as confirmed by the micrograph (Fig. 2.12(a)). However, our analysis also estimates the high damage at sector 6 that is not apparent from the strain measured at this location. In fact, we can clearly observe the trend of strains across the sectors shown in Fig. 2.12(b) to be *different* from the damage distribution shown in Fig. 2.13. These results support the *significance* of processing the measured strains in the present inverse analysis to identify the damage. Somewhat less damage is observed for Specimen D in Fig. 2.13. Here larger damage is estimated near the sectors 3~4 which is also confirmed by micrographic observations (not shown here). The error bound is different for $D < 1$ and $D > 1$ since the strain-damage relations are different in two ranges (see Fig. 2.6(b)). Same magnitude of strain error translates to a smaller error in D for $D > 1$.

In inverse approaches, it is often difficult to prove that estimates are indeed correct or near-correct solutions. In the present study, the defined damage parameter is related to surface thinning. Thus using a vernier caliper (precision of 2.5μm), the thinning was measured and compared with the estimated damage. Measured thinning at 10 sector locations for Specimen C is shown in Fig. 2.14. Due to the uneven surface and varying degree of damage along the length, the accuracy of thickness measurement is not expected to be high (approximated error bound of ±20μm). However, the similarity of measurements with the estimated damage shown in Fig. 2.13 is extremely high. In this analysis, D = 1.0 was defined to equal the material removal of one ply thickness (150μm). These results should prove the effectiveness of proposed procedure.

2.5. Extension to Three Dimensional Models

In this initial study to test the proposed method, it was applied to 1D damage models (2D geometric models) with an assumption of uniform damages along the width direction (i.e., damage variation restricted to length direction). However, the method can be extended for detecting damage over a surface or in 2D damage (3D geometric models) models. Here panels would be divided into virtual (square) sectors/sections over two-dimensional surface. The effective/average damage at one sector then can be expressed as $D_{\alpha,\beta}$ where α and β denote the sector numbers along the axial and width directions, respectively. The following briefly describes the outline of such extension.

2.5.1. Objective Function

For 2D damage models, the error objective function is generated a similar way. As in the case of 1D damage model, it is assumed that strain change due to damages be

controlled by damages at only neighboring nine sectors, namely $D_{\alpha,\beta}$, $D_{\alpha\pm1,\beta}$, $D_{\alpha,\beta\pm1}$ and $D_{\alpha\pm1,\beta\pm1}$. Thus, the normalized change of strain at sector (α, β) can be expressed as,

$$\Delta\widetilde{\varepsilon}_{\alpha,\beta} = \Delta\widetilde{\varepsilon}_{\alpha,\beta}(D_{\alpha,\beta}, D_{\alpha\pm1,\beta}, D_{\alpha,\beta\pm1}, D_{\alpha\pm1,\beta\pm1}) . \tag{2.16}$$

The corresponding local objective function is

$$\phi_{\alpha,\beta}(\boldsymbol{D}) = \frac{\varepsilon^{est}_{\alpha,\beta}(\boldsymbol{D}) - \varepsilon^{meas}_{\alpha,\beta}}{\varepsilon_{\mathrm{o}}} . \tag{2.17}$$

Here damages at different sectors can be expressed in the matrix $\boldsymbol{D}$. As in the previous cases, ε_{o} represents the reference strain corresponding to the state of no damage. The above matrix function can be minimized to obtain the best estimates of damage distributions across the surface using the multivariate Newton-Raphson method.

2.5.2. Formulation of Damage-Strain Relation

Effective identification of unknown parameters requires accurate damage-strain relation expressed in a function. Here using the similar assumptions used for the quadratic formulations (2.7), the damage-strain relations for three-dimensional model can be formulated as,

$$\begin{aligned}\Delta\widetilde{\varepsilon}_{\alpha,\beta} = {} & c_1 D_{\alpha,\beta} + c_2 D^2_{\alpha,\beta} + 2c_3 D_{\alpha\pm1,\beta} + 2c_4 D_{\alpha\beta} D_{\alpha\pm1\beta} + 2c_5 D_{\alpha,\beta\pm1} + 2c_6 D_{\alpha,\beta} D_{\alpha,\beta\pm1} \\ & + 4c_7 D_{\alpha\pm1\beta\pm1} + 4c_8 D_{\alpha,\beta} D_{\alpha\pm1,\beta\pm1} + 2c_9 D^2_{\alpha\pm1,\beta} + 2c_{10} D^2_{\alpha,\beta\pm1} + 4c_{11} D^2_{\alpha\pm1,\beta\pm1}\end{aligned} . \tag{2.18}$$

Here, $2D_{\alpha\pm1,\beta}$ corresponds to ($D_{\alpha+1,\beta}$ +$D_{\alpha-1,\beta}$) and other terms with '±' have similar implications. Similar to the 1D damage models, $D_{\alpha+1,\beta}$ and $D_{\alpha-1,\beta}$ are assumed to have the equivalent effects and so are $D_{\alpha,\beta+1}$ and $D_{\alpha,\beta-1}$. The above function requires determination of eleven independent coefficients, increase of six parameters over the 1D

models. They may be determined with simulated computations and SVD method. It is expected to perform a larger number of simulations with various combinations of $D_{\alpha,\beta}$, $D_{\alpha\pm1,\beta}$, $D_{\alpha,\beta\pm1}$ and $D_{\alpha\pm1,\beta\pm1}$. Our preliminary study of 3D panels suggests more than 200 cases to determine eleven coefficients accurately. Furthermore, estimations improved greatly when additional strain component is used as a measurement (i.e., ε_{22} in addition to the axial strain ε_{11} when the x_1-x_2 plane is set as the composite surface). Certainly, these would add considerable efforts in both formulations and experimental measurements. Furthermore, it may be more practical to measure strains with an optical technique rather with strain gage network.

2.6. Failure Tests on Composite Specimens

Apart from an apparent decrease in strength of the composite that would occur due to the degradation/damage, it would be of interest to correlate damage distribution to failure initiation location. After the damages are estimated using the inverse analysis approach, the regions showing the maximum damage can be expected to be the most compliant and susceptible to early failure. The degraded specimens were submitted to bending in order to determine the failure initiation location using special fixtures. The setup described in Fig. 2.10 cannot be used to perform the failure tests. This is due to the reason that the moment observed causes large rotations such that specimen slips away from contact without failing. A modified fixture with shorter loading span (50 mm), shorter support span (80 mm) and bigger loading pins alleviate the difficulties and ensures that the specimen fails before losing contact with the pins.

The strains are monitored continuously with an aid of oscilloscope. The lead wires from the strain gages are attached to strain indicators that are in turn connected with the

oscilloscope. Since the oscilloscope can handle only four input channels, four strain gages that show the most compliant response are selected for monitoring strains until failure. The failure pattern of the specimens is shown in Fig. 2.15(a). Failure occurs by delamination between the first and second plies on the compressive side. From preliminary results obtained it is quite clear that failure in degraded specimens occur at a lower load compared to the undegraded ones (14% difference). This is shown in Fig. 2.15(b). However a clear difference in strain records that would indicate the delamination/failure initiation location is not observed. Fig. 2.16 (a) highlights the damage estimate records and the sectors in which strains are monitored. Fig. 2.16 (b) shows that load point displacement as a function of strain. It is clear that the failure occurs at earlier load point displacement for degraded specimens than those for undegraded specimens.

2.7. Summary

A novel approach based on an inverse analysis is introduced to estimate damage and degradation distribution on a panel surface. The scheme is proposed as an alternative to traditional damage evaluation techniques, which generally require high set-up costs and complex procedures. This inverse approach processes strain measurements to extract best estimates of damage fields. The verification study followed by the application in the real composite laminates support the effectiveness of this technique.

The key features of this approach and the main observations of our study can be summarized as below.

1. Effective damage-strain relations that consider nonlinear as well as coupling effects are developed. The accuracy of these relations has been verified to estimate the unknown parameters in a robust manner.
2. The inverse analysis methodology utilizes the powerful singular decomposition technique to determine the coefficients in the damage-strain relation when the damage-strain relations are smooth. When the damage-strain relations are not smooth i.e. when damage extends beyond the outermost surface ply, a tensor product B-spline surface fitting technique has been developed for robust damage estimations.
3. To determine damage distributions (i.e., at multiple sectors), the multivariate Newton-Raphson method is utilized, which is an efficient root finding iterative method.
4. Verification analyses are conducted for composite panels with damaged surface. These results show excellent matches between the actual/prescribed damage and the estimated damage via surface strains.
5. Damage distributions in real composite laminates with environmental degradation or physical damage were estimated from strains obtained under four-point bend load. These measurements were successfully used to estimate the damage distributions.

The present method can readily accommodate full-field strain measurements which are more suitable for three-dimensional models. The application of this method for composite laminates with many plies (e.g., 32-64 plies) may be difficult since existence of limited damage cannot be detected in strain measurements. The multi-layer penetrations of damage are needed before strain change can occur. One possible scheme to circumvent the difficulty is to utilize *embedded* strain sensors with optical fibers. If these sensors are

place closer to the surface, they may provide sufficient strain variations to identify damage. Obviously, such a technique would be more costly but these embedded sensor panels are increasingly being considered for health monitoring of structures. The present procedure can be modified to interpret the data from embedded sensors and estimate surface damage state. In addition, the measurement is not restricted to strains. A similar approach can be used to process other variables (e.g., electrical current) to estimate damage.

2.8. References

1. Vaddadi, P., Nakamura, T., Singh, R., (2003). Transient hygrothermal stresses in fiber reinforced composites: a heterogeneous characterization approach. *Composites Part A: Applied Science and Manufacturing*, **34**(8): 719-730.
2. Tarantola, A. (1987). *Inverse Problem Theory: Methods for Data Fitting and Model Parameter Estimation*, NY: Elsevier Inc.
3. Grediac, M. (2004). The use of Full-field Measurement Methods in Composite Material Characterization: Interest and Limitations. *Composites Part A*: *Applied Science and Manufacturing*, **35**(7-8): 751-761.
4. Nakamura, T., Singh, R.P. and Vaddadi, P. (2006). Effects of Environmental Degradation on Flexural Failure Strength of Fiber-reinforced Composites. *Experimental Mechanics*, **46**(2): 257-268.
5. Press, W.H., Teukolsky, S.A., Vetterling, W.T. and Flannery, B.P. (1992). *Numerical Recipes in C: The Art of Scientific Computing*, UK: Cambridge University Press.
6. Hasan, W.M. and Voila, E. (1997). Use of the Singular Value Decomposition Method to Detect Ill-conditioning of Structural Identification Problems. *Computers and Structures*, **63**(2): 267-275.
7. Penny, J.E.T., Friswell, M.I. and Garvey, S.D. (1994). The Automatic Choice of Measurement Locations for Dynamic Tests. *AIAA Journal*, **32**(2): 407-414.

8. Mottershead, J.E. and Foster, C.D. (1991). On the Treatment of Ill-conditioning in Spatial Parameter Estimation from Measured Vibration Data. *Mechanical Systems and Signal Processing*, **5**(2): 139-154.

9. *IMSL Fortran Numerical Library* (1999). Visual Numerics, Inc., San Ramon, CA.

10. Murray-Smith, D.J. (2000). The Inverse Simulation Approach: A Focused Review of Methods and Applications. *Mathematics and Computers in Simulation*, **53**(4): 239-247.

11. *Matlab Reference Guide* (2001). The Mathworks, Inc., Natick, MA.

12. ASTM D6272-02, Standard Test Methods for Flexural Properties of Unreinforced and Reinforced Plastics and Electrical Insulating Materials by Four-Point Bending, In: *Annual Book of ASTM Standard*, Vol. 08.01.

Table 2.1. Coefficients of nonlinear damage-strain equations for $[0/90]_{2s}$ laminates for two different sector widths. They are obtained with singular value decomposition.

Models	Coefficients (%)				
	c_1	c_2	c_3	c_4	c_5
S / t = 1.67	17.5	24.1	4.95	-11.9	9.05
S / t = 3.33	21.8	22.1	2.97	-6.85	4.99

Table 2.2. Control points that represent the best fit for damage-strain relation in B-spline method for $[90/0]_{2s}$ laminates with S/t = 3.33. These are obtained using MATLAB.

Control points (%)		D_α					
		0.0	*0.49*	*1.00*	*1.14*	*1.38*	*1.50*
$D_{\alpha\pm1}$	*0.0*	0	2.39	3.49	9.56	23.4	33.9
	0.49	0.233	2.39	3.51	9.52	23.3	33.8
	1.00	0.557	2.62	3.64	9.62	23.4	33.8
	1.14	1.79	3.74	4.69	10.0	23.6	33.8
	1.38	5.65	7.38	8.24	12.9	24.4	34.5
	1.50	8.91	10.6	11.4	15.8	26.6	35.7

Table 2.3. Normalized increases of experimentally measured strains in sectors under four-point bend loading for four specimens with two different ply composite laminates.

$\Delta\widetilde{\varepsilon}_\alpha$ (%) for $[0/90]_{2s}$ laminates, error bound: ±0.5%										
sectors	*1*	*2*	*3*	*4*	*5*	*6*	*7*	*8*	*9*	*10*
Specimen A	4.00	2.90	3.71	3.47	1.81	1.04	0.66	1.71	2.76	4.38
Specimen B	3.92	2.39	1.01	3.15	4.73	4.84	6.26	5.09	4.17	5.86
$\Delta\widetilde{\varepsilon}_\alpha$ (%) for $[90/0]_{2s}$ laminates, error bound: ±0.5%										
sectors	*1*	*2*	*3*	*4*	*5*	*6*	*7*	*8*	*9*	*10*
Specimen C	1.52	1.12	9.70	12.8	6.65	4.12	1.96	1.55	0.92	0.32
Specimen D	1.18	2.33	5.13	3.77	2.67	2.45	2.06	1.34	1.21	1.19

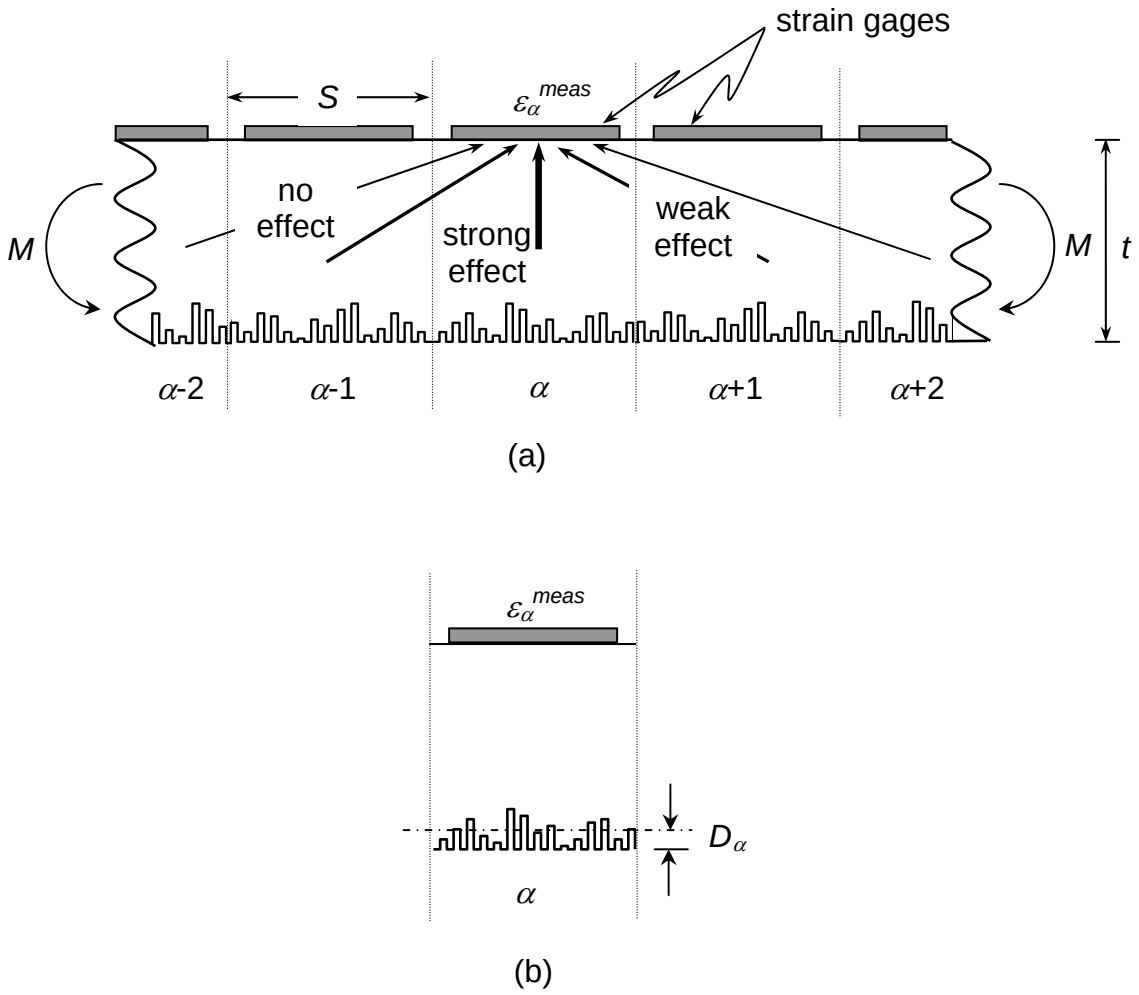

Fig. 2.1 (a) Schematic of surface damaged plate represented by comb-like material removal. Strain measurement is made on the opposite surface under remote bending at each sector. Effects of damages at neighboring sectors are also illustrated. (b) The average extent of damage within sector α is represented by damage parameter D_α.

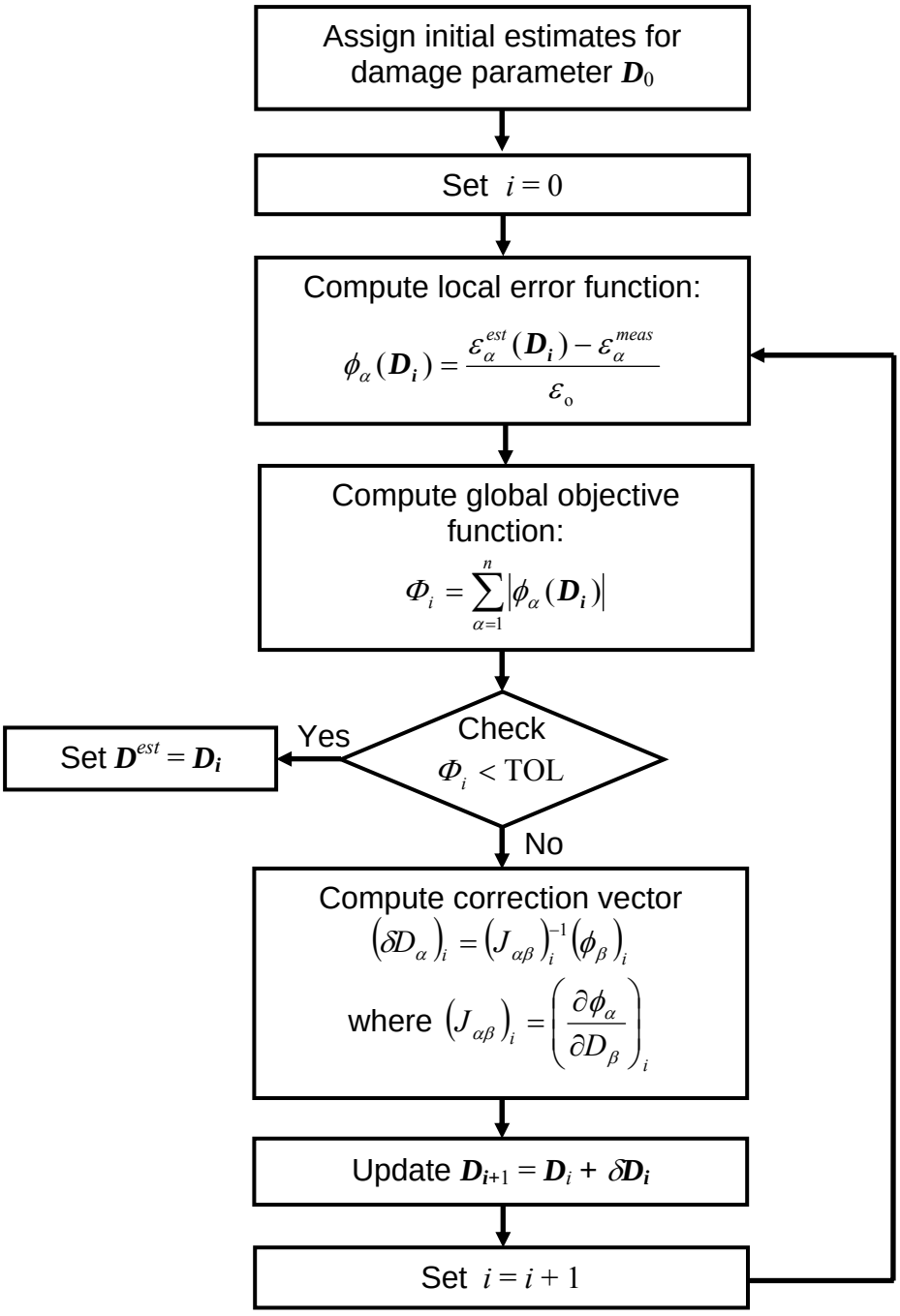

Fig. 2.2. Flowchart for inverse approach to determine damage distribution over sectors.

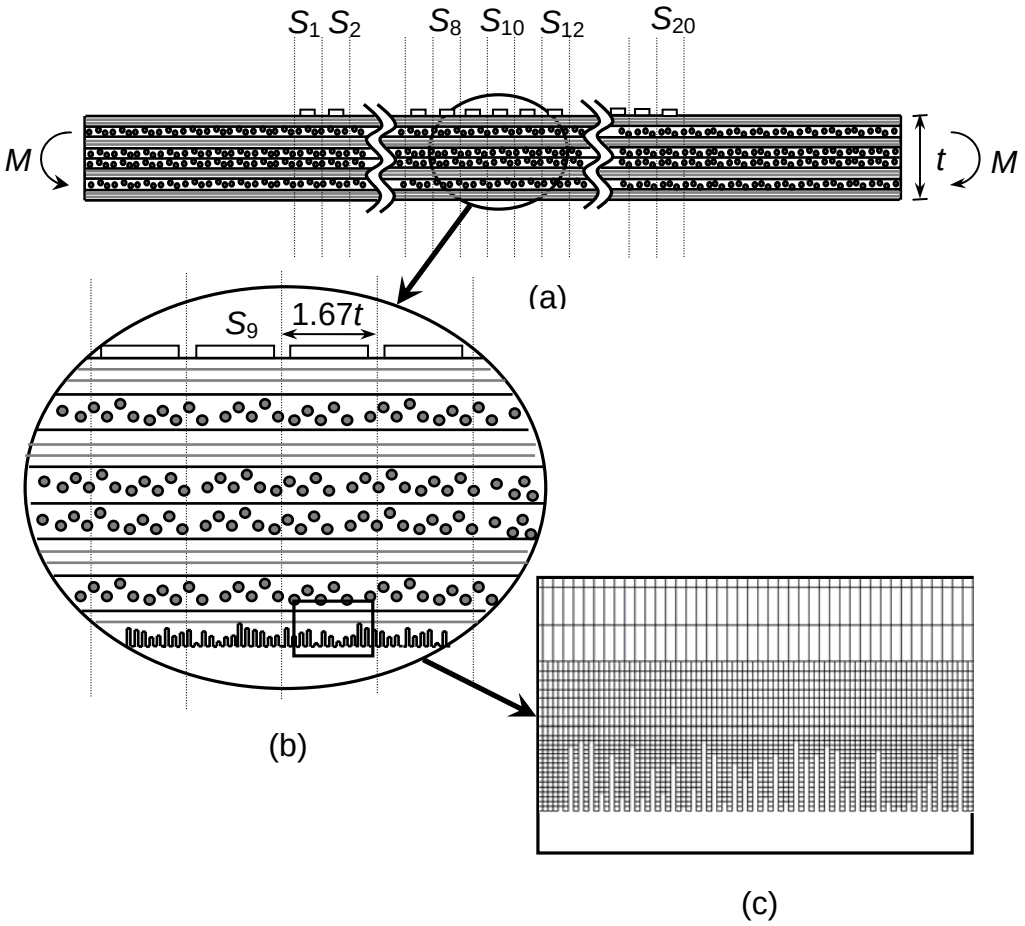

Fig. 2.3. (a) Surface damaged 8-ply $[0/90]_{2s}$ composite laminate subjected to four-point-bend. (b) Enlarged section of model showing comb-like degradation on exposed surface. (c) Finite element mesh near damage. Vertical dimensions are magnified by 5 times for clarity.

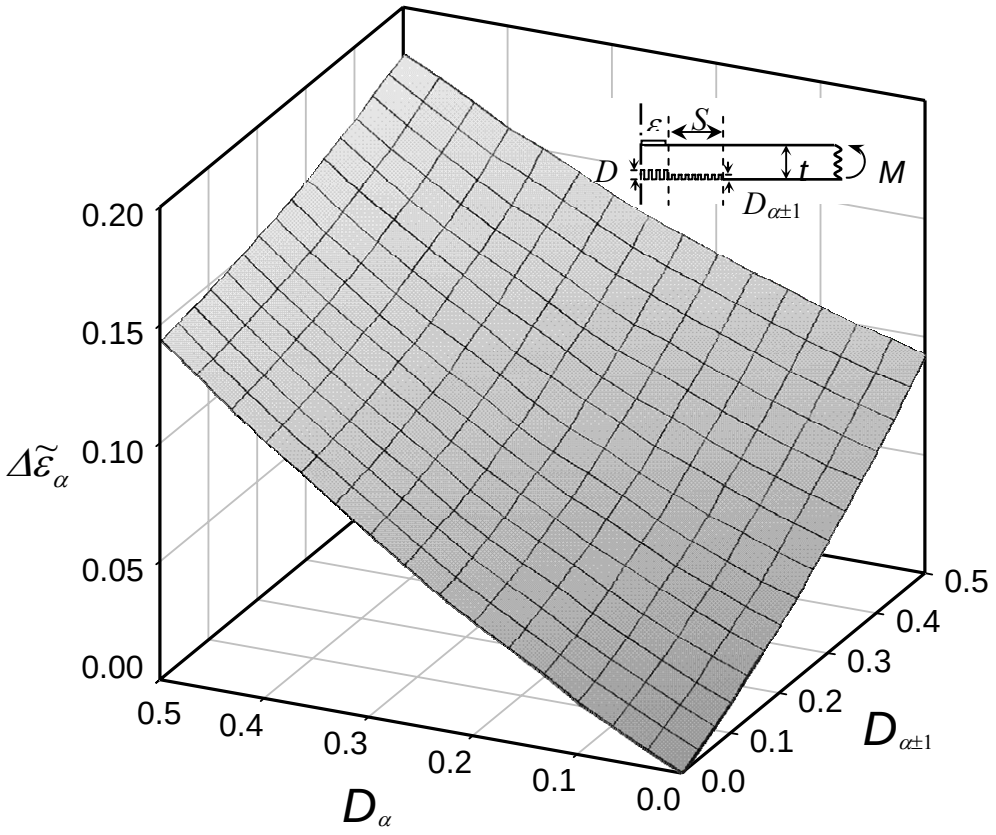

Fig. 2.4. Effects of damage on strains are illustrated for different combinations of D_α and $D_{\alpha\pm1}$ in $[0/90]_{2S}$ laminate with S / t =1.67. Here the maximum damage remains within the 1st surface layer. The model is shown inset.

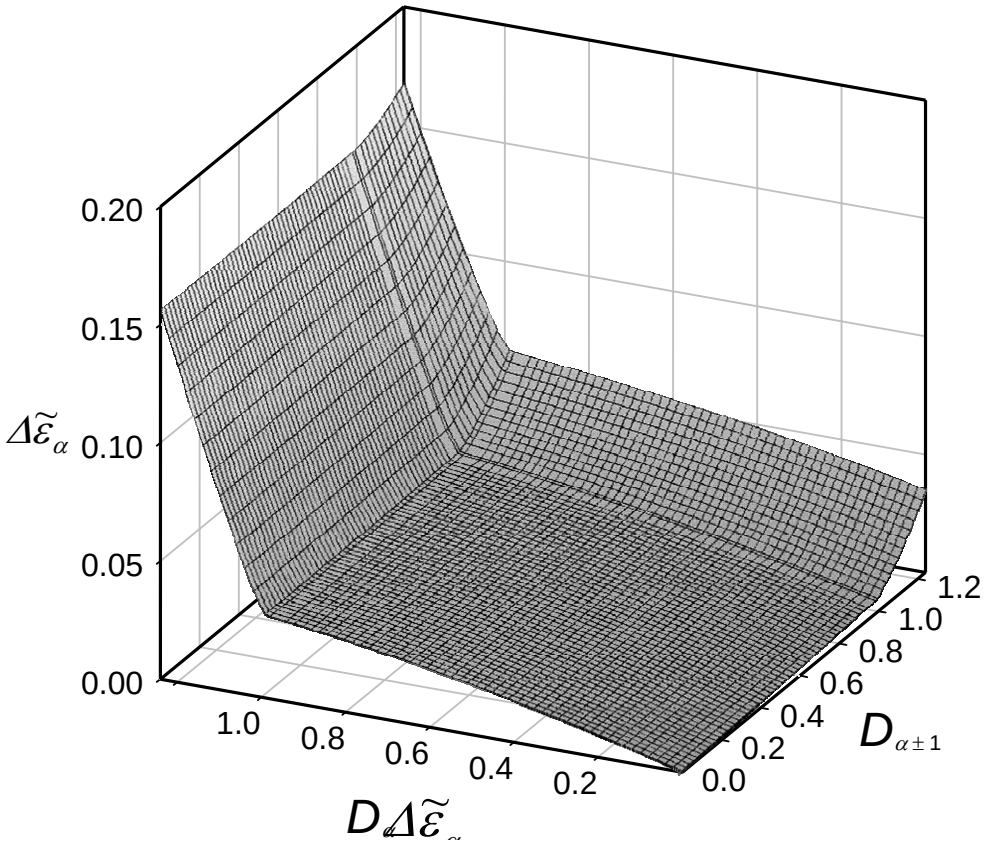

Fig. 2.5. Effects of damage on strains are illustrated for different combinations of D_α and $D_{\alpha\pm1}$ in $[90/0]_{2S}$ laminate with S / t =3.33. Here the maximum damage extends into 2nd surface layer (D > 1.0) where drastic strain changes occur.

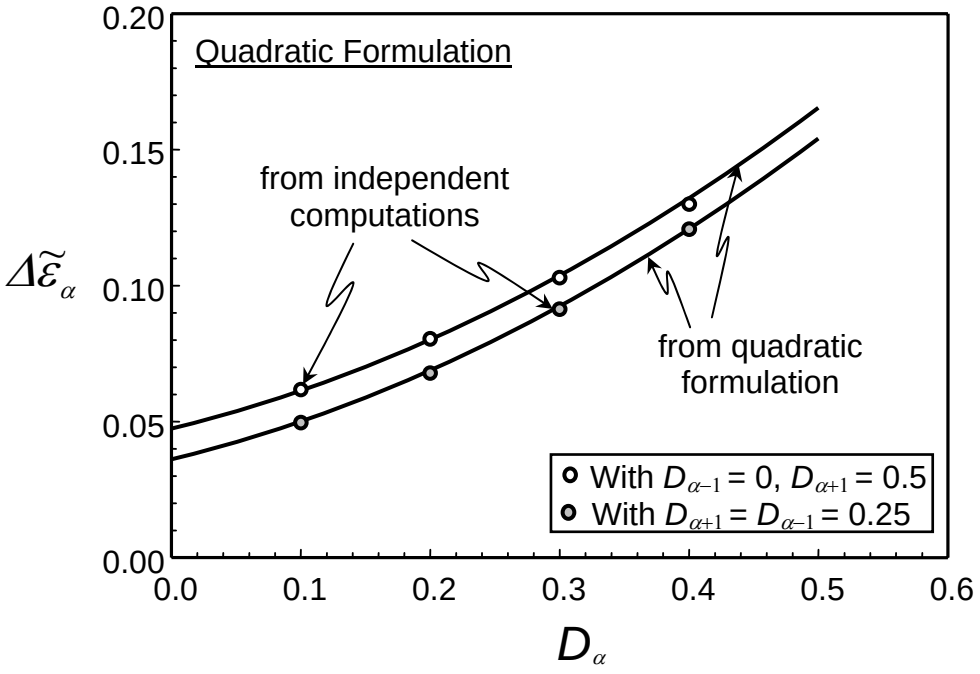

(a)

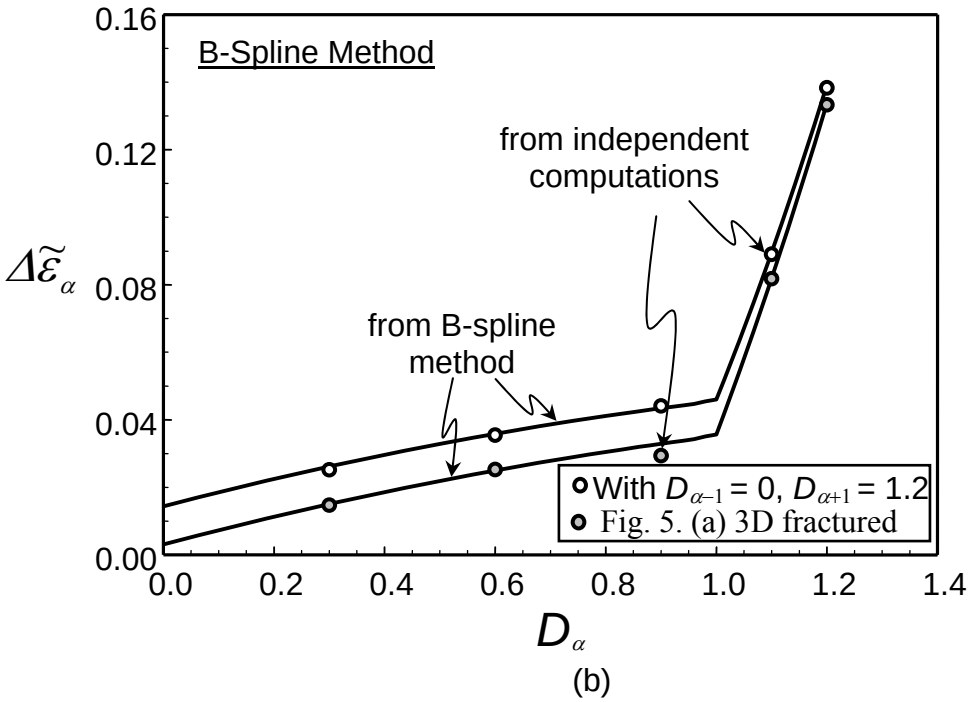

(b)

Fig. 2.6. Accuracies of approximated damage-strain relations are shown with independently computed strains. (a) With quadratic formulation in $[0/90]_{2S}$ laminate with S / t =1.67. (b) With B-spline method in $[90/0]_{2S}$ laminate with S / t =3.33.

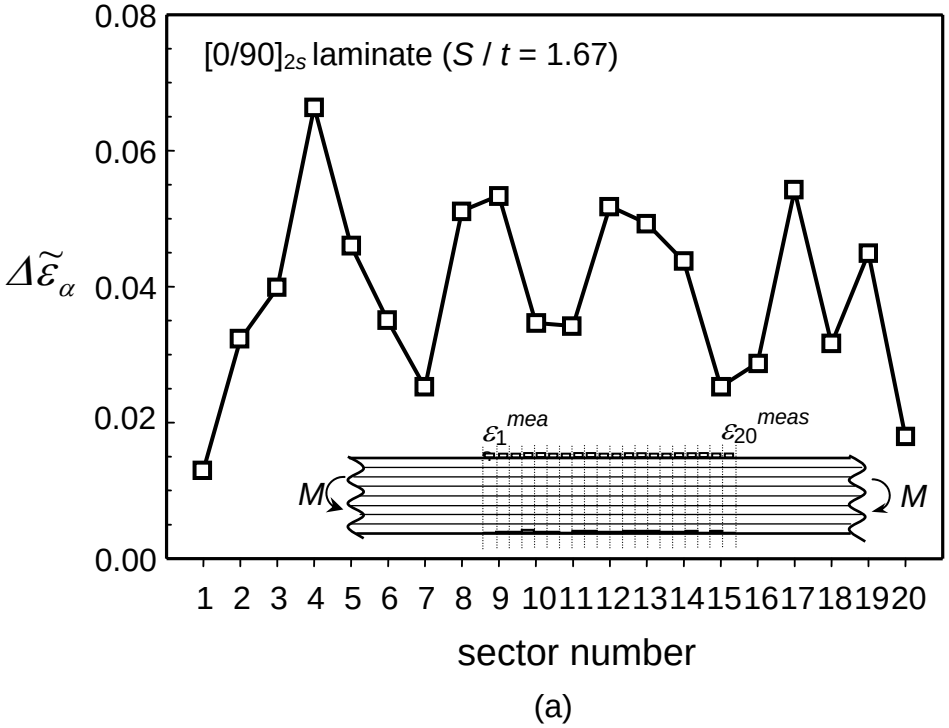

(a)

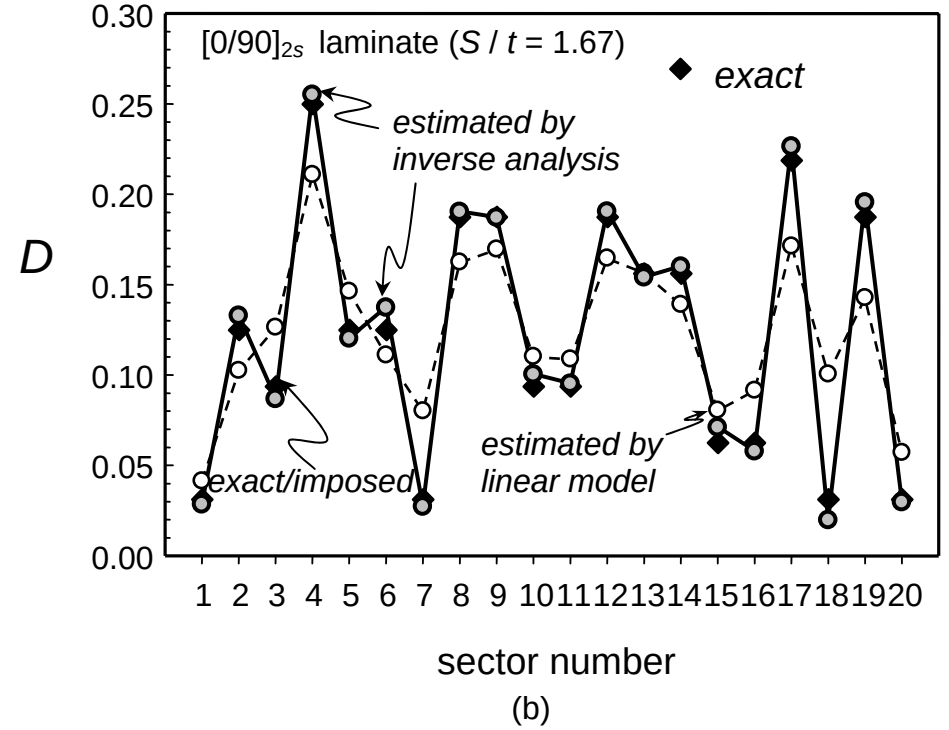

(b)

Fig. 2.7. Results of verification study. (a) Computed strains across 20 sectors. Vertical model dimensions are magnified by 10 times. (b) Estimated damage from inverse analysis (shaded circles). The exact/imposed damage is shown for accuracy check. For comparison, estimates from linear model are also shown (open circles).

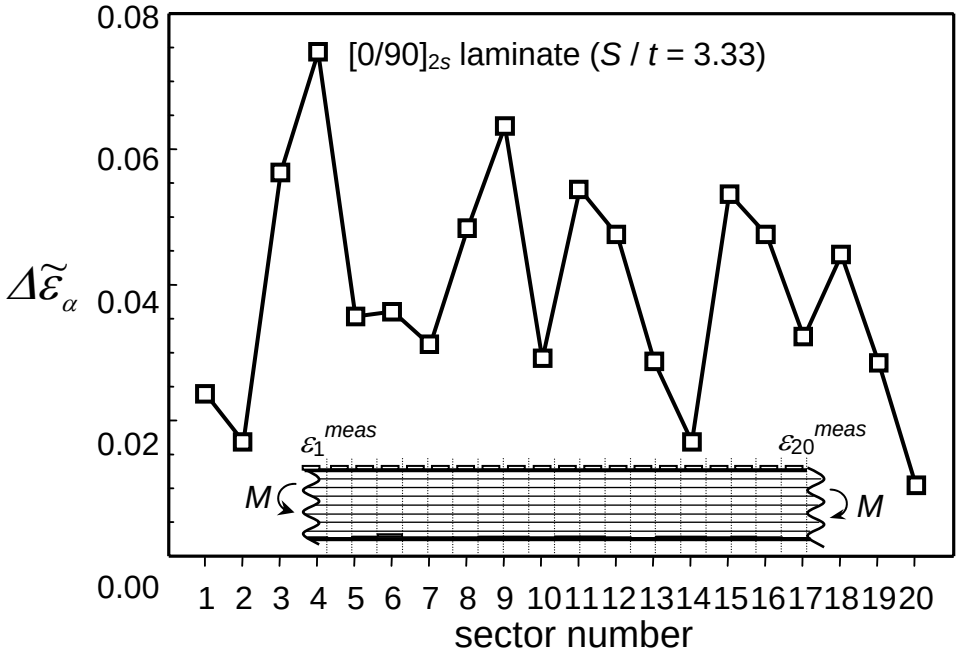

(a)

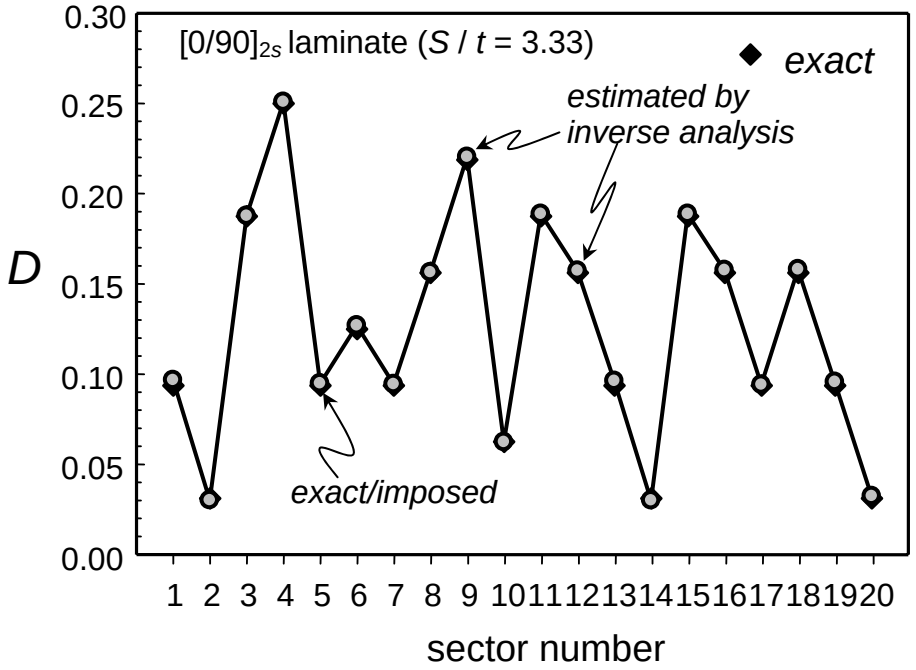

(b)

Fig. 2.8. Verification study for a different sector-width thickness ratio (S / t = 3.33). (a) Computed strains across 20 sectors. Vertical model dimensions are magnified by 10 times. (b) Estimated damage from inverse analysis (shaded circles). Exact/imposed damage essentially overlaps estimate.

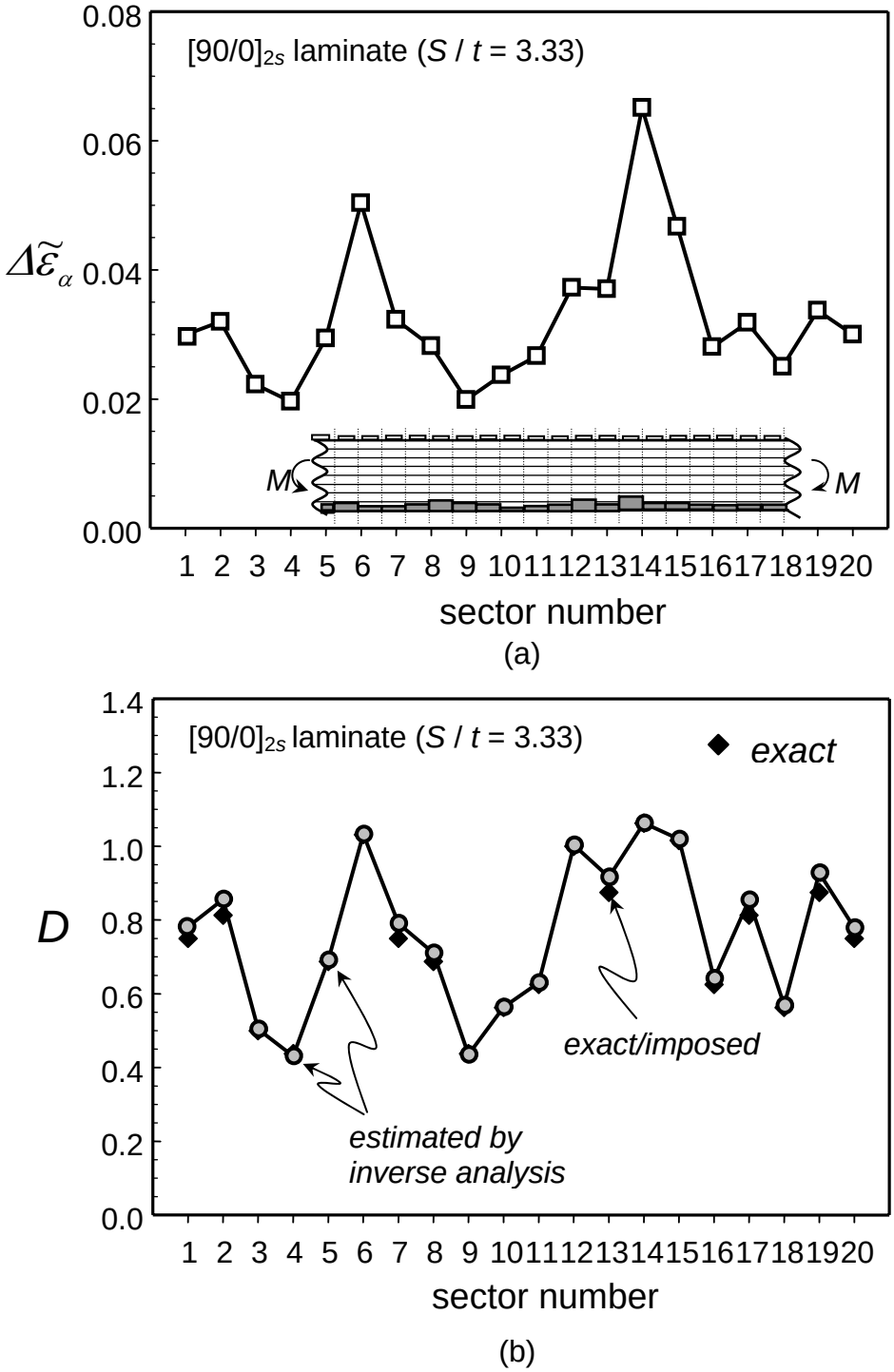

Fig. 2.9. Results of verification study for a physically damaged $[90/0]_{2S}$ laminate. (a) Computed strains across 20 sectors. Vertical model dimensions are magnified by 10 times. (b) Estimated damage from inverse analysis (shaded circles). Exact/imposed damage is also shown for comparison.

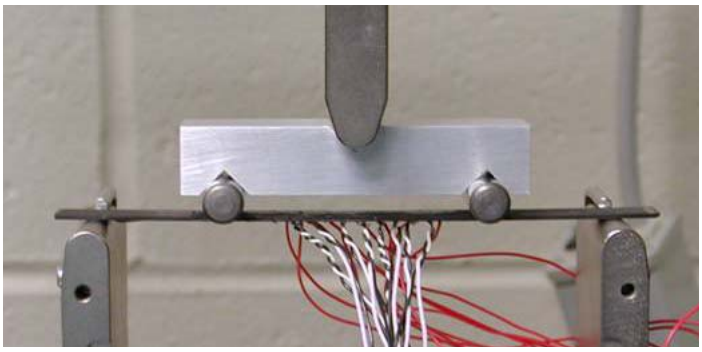

(a)

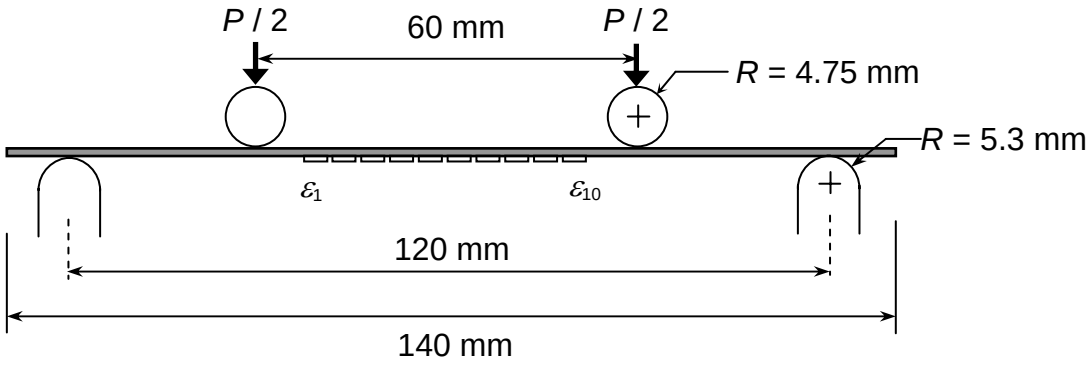

(b)

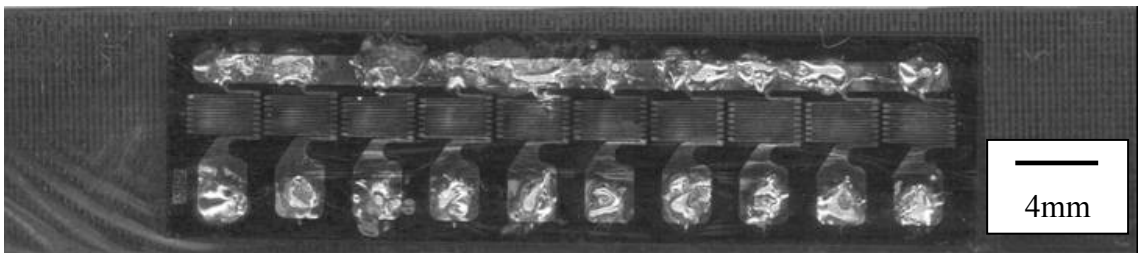

(c)

Fig. 2.10. (a) Four-point bend setup for testing the composite laminates. (b) Schematic of the four-point bend configuration. (c) A strip-gage with 10 strain gages (4mm intervals) bonded on the composite specimen. Lead wires are removed for clarity.

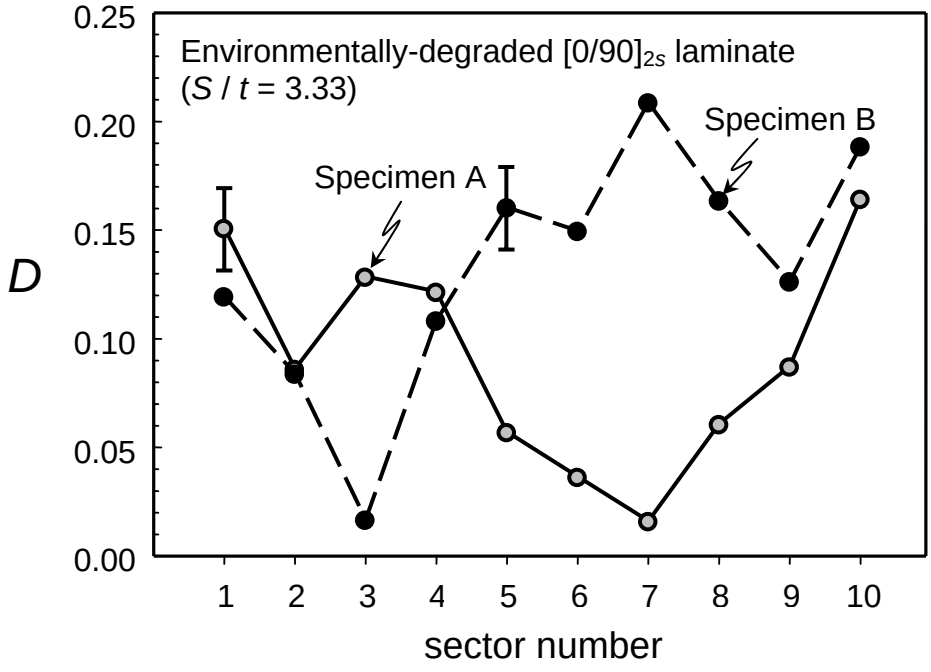

Fig. 2.11. Estimated damage values in the 10 different sectors after performing inverse analysis for two different environmentally degraded $[0/90]_{2s}$ laminates. Approximated error band is $\Delta D = \pm 0.02$.

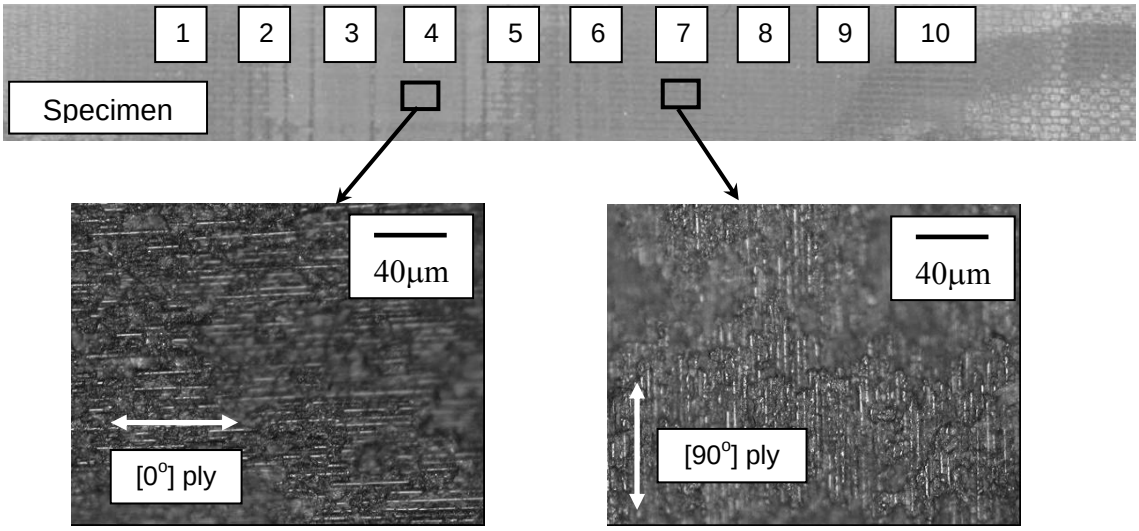

(a)

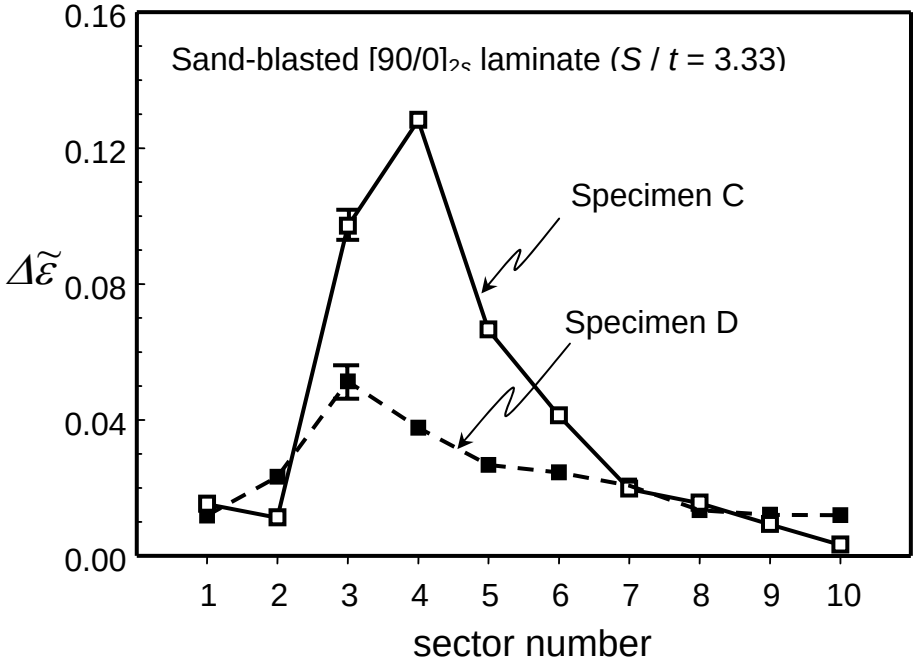

(b)

Fig. 2.12. (a) Damaged surface of specimen C. Locations/sectors of strain gages on the opposite surface are noted. Large damage near sector 4 is confirmed by exposure of 2nd [0^o] ply while damage is contained in the 1st [90^o] ply near sector 7. (b) Normalized strain measurements of sand-blasted $[90/0]_{2s}$ laminates. Error bound for strain is ±0.5%.

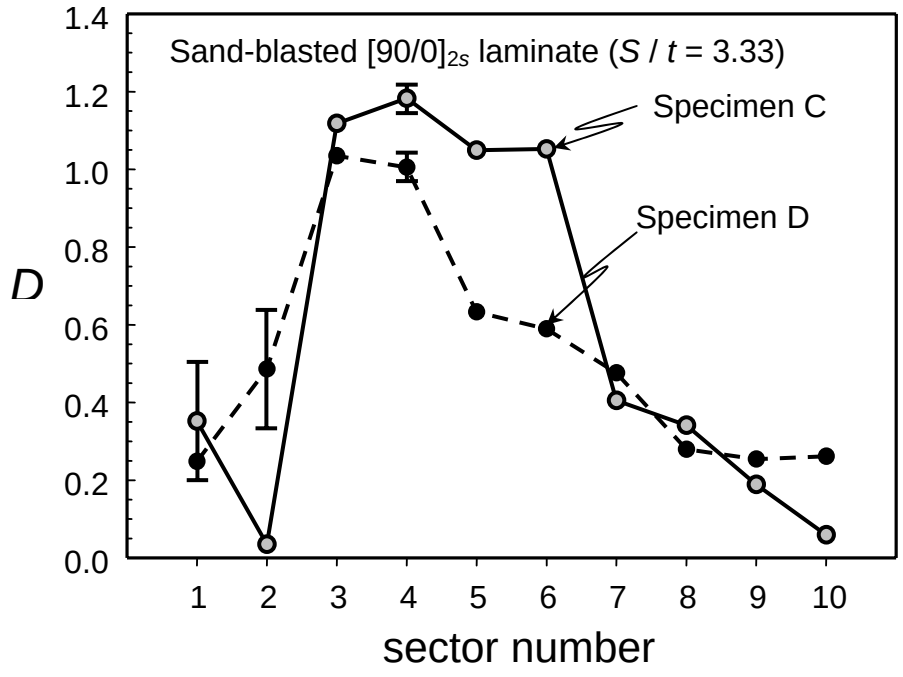

Fig. 2.13. Estimated damage values in the 10 different sectors after performing inverse analysis for two sand-blasted $[90/0]_{2s}$ laminates. Approximated error bounds are $\Delta D = \pm 0.15$ for $D < 1$ and $\Delta D = \pm 0.03$ for $D > 1$.

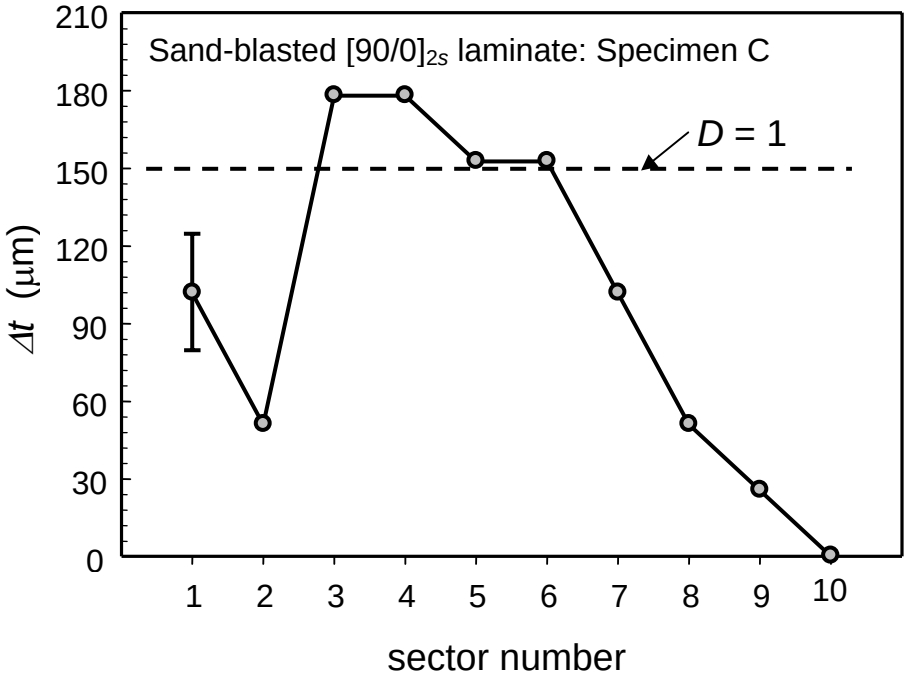

Fig. 2.14. Decreased thickness across sectors measured by vernier calipers. Equivalent unit damage parameter (D =1) is noted. Approximated error bound is $\Delta t = \pm 20\mu m$.

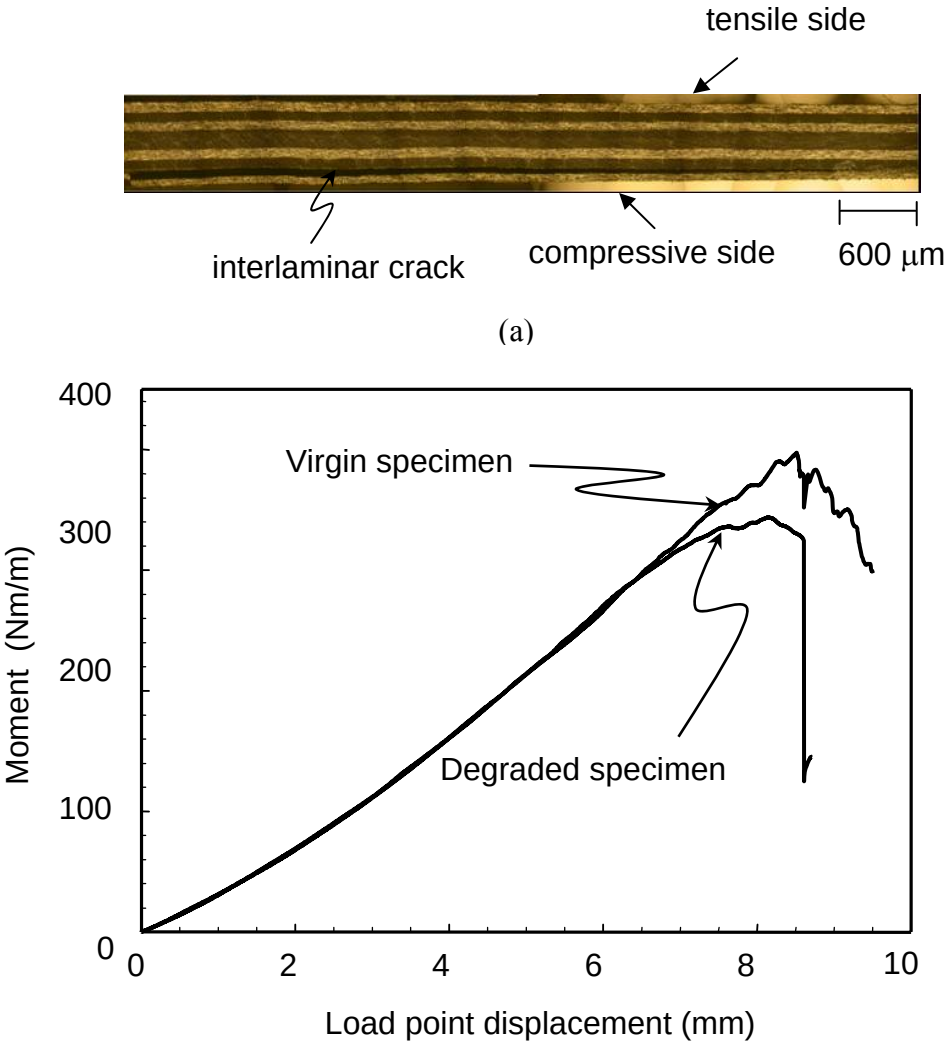

Fig. 2.15. (a) Optical micrograph showing the failure pattern for the 8-ply $[0/90]_{2s}$ composite laminates. (b) Plot showing the failure behavior of undegraded and degraded composite specimens.

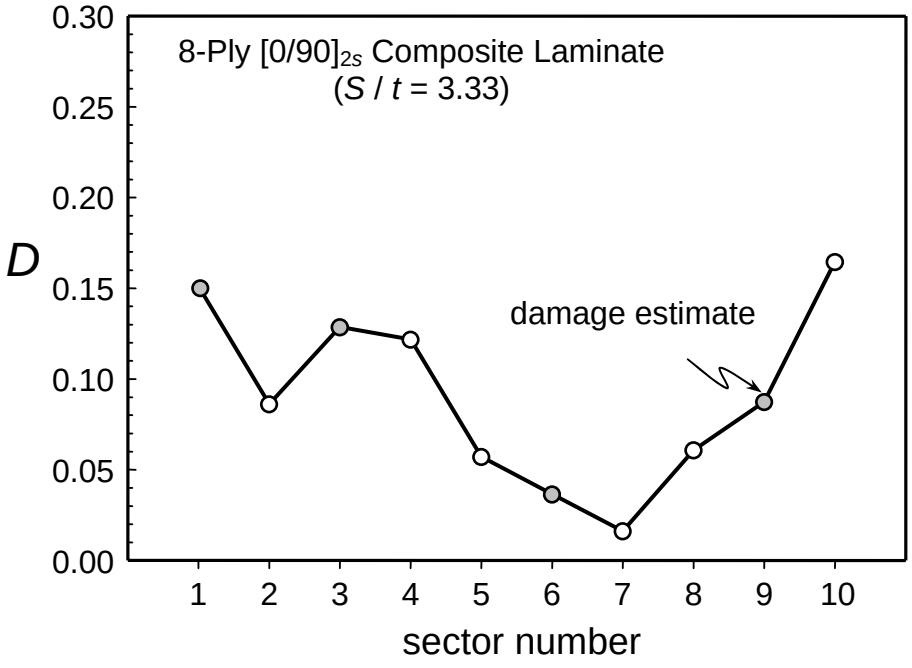

(a)

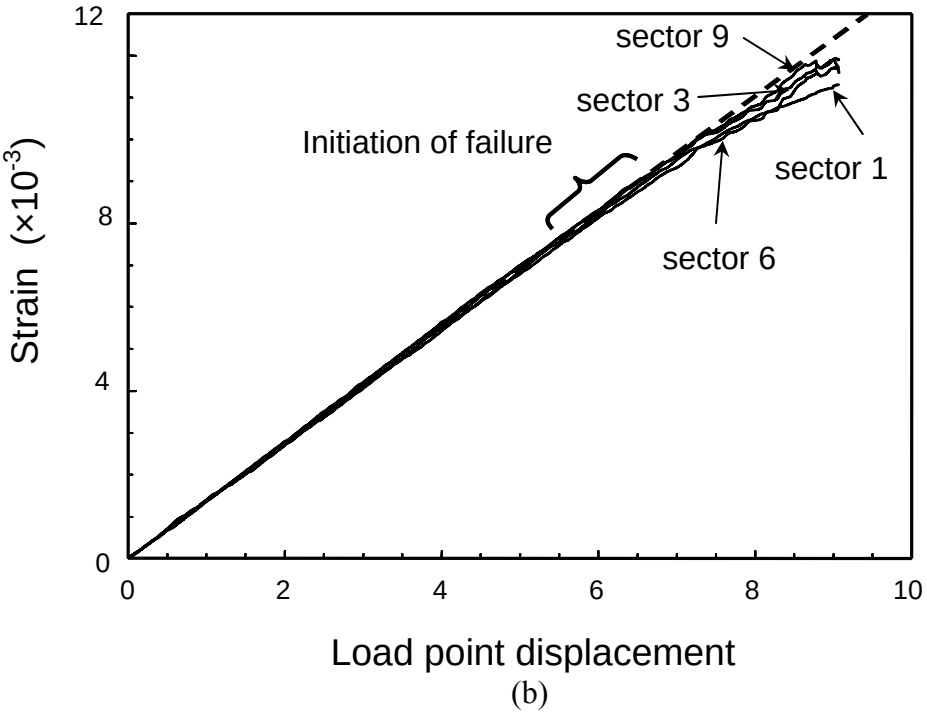

(b)

Fig. 2.16. (a) Damage estimates from which four sectors are chosen for monitoring. (b) Strain variations with load point displacement for four chosen sectors.

3. Interlaminar Fatigue Crack Growth of Cross-Ply Composites under Thermal Load

3.1. Introduction

The current study is undertaken to describe the fatigue delamination growth under thermal load. Specifically, it reveals how an existing interlaminar delamination can propagate from temperature change without any external mechanical load. Following the thermal cycling tests, fatigued surfaces are closely examined to determine the fracture mode. In addition, the rate of crack growth is correlated with the range of energy release rate (obtained through computational models) using both 2D and 3D models. The relation is used to determine the level of threshold energy release rate needed to sustain crack growth phenomenon. A brief review of the experimental work by Vaddadi [1] is provided to better explain the computational modeling work undertaken.

3.2. Experimental Procedure

3.2.1. Specimen Fabrication

Carbon fiber reinforced epoxy composite laminates were prepared using vacuum bagging with unidirectional carbon fiber cloth C383 (acquired from CST Sales). The fiber cloth was smooth webbed having a weight of 4.7 Oz., width of 12" and thickness of 0.006". As a part of the epoxy system, Epon 862 resin, a low viscosity, liquid epoxy resin manufactured from epichlorohydrin and Bisphenol-F was used (Hexion speciality chemicals, Houston, TX). This system offers several advantages including long working life, high elongation, very versatile processing system for fabricating fiber reinforced

pipes, tanks and composite parts. In order to cure the epoxy a curing agent, Epi-cure was used by 15% of the weight of resin. Finally, the specimen is post-cured for 2 hours at 120ºC.

The vacuum bagging procedure was use to fabricate $[0°_{12}/90°_{12}]$ laminates consisting of twelve 0° and twelve 90° plies. This unique arrangement was chosen to maximize the stresses generated by the thermal expansion mismatch between 0° and 90° plies. Prior to curing, a pre-existing delamination crack was introduced along this interface by inserting a strip of Teflon tape. Test specimens were machined from the post-cured laminate using a water-cooled high-speed diamond saw, and then the edges were polished using 120, 400 and 600 grit metallographic papers to remove any microstructural damage that might have occurred during cutting. A schematic of the specimen configuration is shown in Fig. 3.1. Prior to thermal cycling, the crack faces are tapped to open to ensure no local bonding (from residual epoxy) between the crack faces.

3.2.2. Mechanical and Thermal Properties of Lamina

Here, primary goals are to characterize crack growth in composites under thermal cycling and to investigate if the growth rate follows the Paris-law, as for fatigue under mechanical loading [2]. The latter analysis requires the estimation of fracture parameters, as well as mechanical and thermal properties of the composite material. To this end, separate specimens consisting of an 8-ply unidirectional laminate were fabricated using the same vacuum bagging process. Tensile tests were performed on these specimens to obtain load-displacement data as well as independent strain measurements from gages bonded on the specimen surface. From tests conducted on both $[0_8]$ and $[90_8]$ specimens the tensile moduli in the longitudinal and transverse directions were measured to be E_L =

105±2GPa and E_T = 5.5±0.08GPa, respectively. Using the longitudinal modulus and known properties of the fibers and matrix, the fiber volume fraction was estimated to be 44% via the rule of mixtures. The estimated values of other mechanical parameters for the transversely isotropic materials were ν_{LT} = 0.33, ν_{TT} = 0.30 and G_{LT} = 3.50GPa. In order to estimate the poisons ratios, strain gages were bonded in both longitudinal and transverse directions to record the longitudinal and lateral strains.

The coefficients of thermal expansion (CTE) were determined by strain measurements on unidirectional laminates that were heated in an environmental chamber (Benchmaster BTRS, Lunaire Ltd., Williamsport, PA). Here the temperature was varied from 25°C to 125°C and strains were measured for unidirectional $[0]_8$ and $[90]_8$ laminates. To ensure accuracy, a separate aluminum plate with strain gages was placed in the same chamber to obtain reference strain measurements. During the experiment, the temperature was raised at 20°C intervals, and the system was allowed to stabilize for few minutes to ensure thermal equilibrium. The accuracy of the strain measurements was further verified subsequently by raising the temperatures directly to intermediate values and comparing strains with earlier measurements. The measured CTE exhibited slight temperature dependence. However, since it was not significant, the temperature variation was not considered and the average value was chosen for the present analysis. The longitudinal and transverse coefficients were estimated to be $\alpha_L = 0.63 \times 10^{-6}/^{o}\text{C}$ and $\alpha_T = 32 \times 10^{-6}/^{o}\text{C}$, respectively. The procedure for determining these coefficients are discussed in further detail in another work [3]. Here, from strain variation of composite laminate with temperature, the CTE of epoxy was estimated through an inverse analysis procedure.

However, since information on CTE of fiber is well documented, this value was treated as known.

Prior to the thermal fatigue tests, similar pre-cracked specimens were utilized to estimate fracture resistance under monotonic mechanical load. Using the double cantilever beam set-up with attached hinges at the ends, the specimen was fractured under opening mode. The measured toughness was G_{Ic} = 155 ± 7J/m^2. The specimen was also loaded under 4-point-bend to generate shear dominated mode. However the specimen failed at the surface of 90^o ply before the crack growth initiation could occur along the interlayer.

3.2.3. Thermal Cycling Tests

Thermal cyclic loading tests were conducted using the same environmental chamber used to measure CTE. It provides automated cyclic or constant condition at certain temperature as well humidity. In the current experiments, in order to isolate the effects of thermal loading, the relative humidity was set at 0%. The objective of the thermal cycling tests was two fold, first to measure the crack growth length as a function of the number of thermal cycles, and second to observe the effect of temperature range on the crack growth rate. Accordingly, different ranges of temperatures were employed. A typical thermal cycle was carried out as follows. In the case of ΔT = 140^{o}C, initially the temperature was maintained at 20°C for 10 minutes. This was followed by a steady ramp up to 160°C within 30 minutes. Then the temperature was held constant at 160°C for 30 minutes to ensure thermal equilibrium throughout the specimen. Finally the specimen was cooled down to 20°C in 40 minutes. The entire thermal cycle lasts about 110 minutes.

Measurements of the crack length were made after every twenty thermal cycles with simple visual crack detection after the specimen surfaces were masked by white correction tape to highlight the location of current crack tip. These measurements were made for two separate specimens under an optical microscope at a magnification of 50 times the original size. In order to determine the length, an image of a micro-scale with a precision of 10μm was superimposed on the picture. Two separate specimens were used in the measurement. For each specimen, the crack tip positions on both sides were measured. In this manner the crack length was established as a function of the number of thermal cycles.

Figure 3.2 shows the optical micrographs of crack growths after different numbers of thermal cycles. For each measurement, the specimen was taken out of the environmental chamber for about 8 minutes, which is presumed to be short enough to have minimal effects on the crack growth behavior. The crack growth behavior is shown as a function of thermal cycle in Fig. 3.3(a). Here the average of 4 measurements is plotted for up to 920 cycles or about 70 days. Note that the variations of crack lengths were generally within ±2% among the four locations. However, it is important to note that these measurements were made at the surfaces and they do not necessarily represent the crack length through the thickness. Uneven or curved through-thickness crack growth will be discussed later in Section 3.2. During the test, the temperature amplitudes were varied as indicated in the Fig. 3.3. The initial amplitude of $\Delta T = 140^{o}$C was intentionally chosen to be large to ensure crack initiation and grown. The four subsequent temperature amplitudes of $\Delta T = 60^{o}$C, 30^{o}C, 100^{o}C, and 120^{o}C were prescribed during the measurement period to systematically vary the crack growth behavior. Since the

temperature amplitudes need to drive the crack at various rates were not known *a priori*, they were determined by trial-and-error during the course of the experiment. In Fig. 3.3(a), the slope represents the crack growth rate for given temperature amplitudes. Figure 3.3(b) shows the crack growth rate per cycle.

The effects of temperature amplitude can be clearly observed in these figures. During the initial phase of ΔT = 140°C, it took about 240 cycles to reach steady state propagation when the growth rate was estimated to be da/dN = 5.1μm/cycle. At 500th cycle, the temperature amplitude was switched to 60°C and maintained for 100 cycles. The smaller number of cycles was chosen since it was observed that the propagation reached steady state much faster. Nonetheless, the steady state rate of crack was lowered. In the subsequent phase (after 600 cycles), ΔT was further reduced to 30°C. With this temperature variation, the measurements showed no visible change in the crack length even after 80 cycles. It is likely that driving force to fatigue growth is below the threshold value. Note that prior to testing, we had no knowledge of the dependence of ΔT on the delamination growth. Thus the temperature changes were assigned based on the crack growth behavior observed in the previous segment. The next ΔT was chosen to be 100°C. As the measurements were made, it took longer time to reach the steady state. This is probably because the crack was arrested for about 6 days at ΔT = 30°C and some healing might have occurred near the crack tip. To ensure steady state condition the ΔT = 100°C condition was maintained for 180 cycles. For the final test, the temperature amplitude was set at ΔT = 120°C for 60 cycles. Although a detailed analysis was not carried out to determine dependence on loading history (i.e., order of imposed ΔT), such an effect is likely to be minimal for crack growth after steady state has been reached.

3.2.4. Examination of Fracture Surfaces

The fracture surfaces were examined at the conclusion of the thermal cycling test. To open the crack surfaces for microscopy the specimens were immersed in a nitrogen bath and then split in half along the crack plane. Figure 3.4 shows an optical and SEM micrographs of the fracture surfaces which revealed unexpected crack growth phenomena. Two specimens showed non-uniform propagation across the thickness or crack front, and the cracks appeared to grow from the edge or free-surface toward the interior. At the mid-section, there was essentially no propagation. Also, the propagation behavior was nearly symmetric about the mid-point. The average angle between the initial crack front and the kinked crack front was measured to be 43.5^{o}.

The micrographs also showed three different exposed surfaces belonging to the 0^{o} and 90^{o} fiber layers and the interlaminar epoxy phase. This observation suggests non-planar growth of the crack front during the fatigue process. A closer inspection on the non-planar crack surface was made using an optical surface profiler (Digital Microscope, Keyence, VHX-500K, Osaka, Japan). Figure 3.5(a) shows the topology of the crack surface near the line denoted as A–B in Fig. 3.4. The zero depth was set to the middle of interlaminar epoxy phase which in turn was measured to be 15μm thickness using optical microscopy of the specimen edge. The measured depth variation between the points *A* and *B* is also shown in Fig. 3.5(b). Here three different phases are superimposed to show approximate location of crack. The crack is initially located within the 0^{o} ply, designated as point A. The crack then enters into the epoxy phase before finally entering the 90^{o} ply. Similar alternating crack planes were also observed for the other specimen whose micrograph is not shown here.

The observed nonlinear crack plane suggests that the interlaminar epoxy layer is sufficiently tough so as to not represent a weak plane. Otherwise the crack would have most likely chosen a weak plane to propagate. Crack growth in alternating planes is also driven by the predominantly Mode II condition, as described in the next section. The large shear condition coupled with the crack contact condition may generate the unstable crack growth condition. In addition, although not determined in this analysis, the *T*-stress might have also played a role. These observations of fracture surface dictate the necessity for a 3D model to analyze fatigue growth behavior. The following section describes the computational procedure used to determine the energy release rate as well as the mixed-mode stress intensity factors.

3.3. Computational Analysis of 3D Thermal Crack

3.3.1. Finite Element Models

Since no analytical solutions exist for a three-dimensional crack front in a composite laminate, a finite element model was constructed to identify the relationship between thermal loading and the fracture parameters. Three crack front configurations were considered for analyses. Two of these include the initial straight crack front (before propagation) and the final angled or kinked crack front (after propagation) shown in Fig. 3.4(a). In between, an additional model was also generated based on estimated crack front evolution during thermal cycling process. For homogenous materials, Heyder and Kuhn [4] utilized transparent materials to record evolution of crack front in their 3D fatigue crack propagation study. Similar observations of the growing crack front would have been ideal even in this case. Nonetheless, this is not possible due to the opaque nature of

the specimen. Furthermore, carrying out a series of interrupted tests would require a very large number of specimens and a prohibitively lengthy test period.

To construct the final crack front configuration, dimensions of fracture surfaces of two specimens were measured. As described in the previous section, the crack front consists of three nearly linear sections. One at the middle and two inclined at the sides with the kink angle being 43.5^{o}. A schematic of delamination model is shown in Fig. 3.6. Since intermediate crack front shapes were not known, it is assumed that they maintain similar angle between the middle crack front and the angled crack front. Although other growth models are possible, all should have similar fracture parameter variations (e.g., energy release rate along crack front), at least qualitatively. In this study, three separate models representing different stages of crack growth were constructed, as shown in Fig. 3.6. The first model (crack front *A*) is for the initial stage possessing a straight crack front along the width direction (the configuration prior to thermal cycling). Next model corresponds to an intermediate stage of crack propagation (crack front *B*). A third model (crack front *C*) represents the measured growth at the final stage. In addition, the crack growth was assumed to be planar even though vertically alternating crack paths were observed, as shown in Fig. 3.5. Although such a behavior is also an important subject of interlaminar crack growth, the study would require detailed microstructural models. Since our present aim is to understand the fatigue growth behavior at continuum level, our 3D models did not take into account the non-planar growth.

In order to construct the finite element model, a mesh generator was developed. The symmetry condition was utilized to model only a half of the actual specimens, fine elements were used at the crack front, and 30 element layers were taken along the half-

width of the specimen. A selectively refined mesh was used to ensure accurate computations of mixed-mode stress intensity factors along the crack front. The final crack growth configuration model, shown in Fig. 3.7, contains approximately 60,000 eight-noded brick elements. The material model was chosen to be transversely isotropic and the properties reported in Section 3.2.2 were assigned. The upper half was modeled as 0^o ply (fibers in the direction of crack growth) while the bottom half was modeled as 90^o ply (fibers perpendicular to the direction of crack growth). During trial computations, a limited overlapping of top and bottom crack surfaces was observed (due to large Mode II condition). In order to circumvent the problem, contact conditions were enforced between the fracture faces to avoid overlapping. Furthermore, in order to minimize calculation errors for fracture parameters, the angled crack location was slightly smoothed by introducing a narrow transitional region that was 1.7mm wide.

3.3.2. Determination of 3D Fracture Parameters

Using the 3D model, relevant fracture parameters along crack front were computed. For the orthotropic materials, the relationship between the energy release rate and three stress intensity factors is given as [5],

$$\mathsf{G} = \frac{H_A}{4\cosh^2(\pi\varepsilon)}\left|\boldsymbol{K}\right|^2 + \frac{H_B}{8}K_{\mathrm{III}}{}^2 \tag{3.1}$$

Here $\boldsymbol{K}$ is the complex stress intensity factor and is given by $\boldsymbol{K} = K_{\mathrm{I}} + iK_{\mathrm{II}}$. Also the material constants H_A and H_B can be determined from the Hermitian matrix $\boldsymbol{H}$ and ε is the oscillatory index which depend on material properties. Note that $\boldsymbol{H}$ has a complex form for orthotropic bimaterials but H_A and H_B reduce to $4/E_{\mathrm{eff}}$ and $4/\mu_{\mathrm{eff}}$, respectively, for isotropic bimaterials in which case E_{eff} and μ_{eff} are the effective tensile and shear moduli.

The determination of these parameters was shown by Nakamura *et al.* [5] and Yang *et al.* [6]. In the present model, they are H_A = 0.5786/GPa, H_B = 1.399/GPa and ε = –0.0601. Many experimental studies have shown that the critical energy release rate G_c depends on the mode of fracture. Generally under a predominantly Mode II condition, G_c is a few times greater than that under Mode I condition [7]. Thus it is essential to quantify the mixed-mode state. A convenient way to define the mixed-mode condition is to use phase angles. For 3D cracks that can possess all three modes, it is necessary to utilize two phase angles, ψ and ϕ. The first phase angle must be defined in terms of a characteristics length scale, L, as,

$$\psi(L) = \tan^{-1}\left\{\frac{\mathrm{Im}(\boldsymbol{K}L^{i\varepsilon})}{\mathrm{Re}(\boldsymbol{K}L^{i\varepsilon})}\right\} \cong \tan^{-1}\left[\left(\frac{\sigma_{12}}{\eta\sigma_{22}}\right)_{r=L}\right] \tag{3.2}$$

Where η is a traction resolution factor and given by $\eta = \sqrt{H_{22}/H_{11}} = 1.25$ in the current model. In our analysis, L = 80 μm was chosen since the size of fracture process zone is probably about this length-scale. However a phase angle with other L may be obtained through the equation below.

$$\psi(L_2) = \psi(L_1) + \ln\left(\frac{L_2}{L_1}\right) \tag{3.3}$$

The other phase angle that is related to the out-of-plane shear mode may be introduced as,

$$\phi = \cos^{-1}\left[K_{\mathrm{III}}\Big/\sqrt{\frac{2H_A}{\cosh^2(\pi\varepsilon)H_B}\left(K_{\mathrm{I}}{}^2 + K_{\mathrm{II}}{}^2\right) + K_{\mathrm{III}}{}^2}\right] \tag{3.4}$$

In the present model where the crack front propagation is not linear, the magnitudes of two shear modes K_{II} and K_{III} depends greatly on the growth angle. Thus it is useful to

quantify the effective shear mode with respect to tensile mode, and an additional phase angle may be introduced as

$$\varphi = \cos^{-1}\left|\cos\psi \sin\phi\right| \tag{3.5}$$

Under pure Mode I conditions $\varphi = 0^o$, and if the crack growth is dominated by shear then $\varphi \to 90^o$.

3.3.3. Computed Results

The three models shown in Fig. 3.6 were loaded by assigning a temperature increase at every node. The computed effective stress contours near the crack fronts of model C under $\Delta T = 140^o$C are shown in Fig. 3.8. These plots show stress contours on the plane of crack on both sides, i.e., bottom 90^o ply and top 0^o ply. Note that the near front stresses exceed 150MPa under this temperature. The high stresses indicated by red essentially denote the shape of kinked crack front. Large stresses can be also observed near the free-surface of uncracked ligament.

Figure 3.9 shows the contours for different components of stress but only on the side of the 0^o ply. The large tensile stress σ_{11} in the uncracked ligament corresponds to smaller CTE for 0^o ply. On the 90^o ply, σ_{11} is negative at the uncracked ligament due to its larger CTE. The opening stress σ_{22} is not zero on the cracked surface but slightly negative. This indicates that crack surfaces are in contact and it is consistent with negative K_I results, as discussed next. The two shear stress components σ_{12} and σ_{23} show very large magnitudes ahead of crack front. The 3D energy release rates, computed via the domain integral [5], are shown as a function of the arc length measured from the

center or symmetry plane in Fig. 3.10. Here the energy release rate is normalized by $hE^*(\Delta\alpha\Delta T)^2$, where h is the laminate thickness, E^* is the effective in-plane tensile modulus defined as $E^* = 4\cosh^2(\pi\varepsilon)/H_A$, and $\Delta\alpha = \alpha_T - \alpha_L$. The energy release rate for the crack front A shows a steep increase near the edge or the free-surface. Such behavior is consistent with a 3D interface crack under dominant Mode II condition [8]. Furthermore it supports that the initiation point of crack growth is at the free edge, as observed on the fracture surfaces. For the other two models, the largest G occurs near the angled or kinked region as indicated in Fig. 3.10. It is also interesting to note that the location of maximum G shifts toward the mid-point as shown in the mid-stage model B and the final stage model C. In addition, the energy release rate is more even across the entire crack fronts in these models. In Fig. 3.10, the energy release from the plane strain model ($G/hE^*(\Delta\alpha\Delta T)^2 = 0.112$) is also indicated. This value is lower than any of 3D values due to greater constraint condition.

Due to the nature of thermal loading, the primary mode of crack growth was expected to be Mode II. The first phase angle ψ is shown in Fig. 3.11(a). In all models, it is nearly constant at $\psi \cong 100^o$ along the initial (unkinked) crack fronts. Note the sign of K_I is negative while K_{II} is positive with that angle. For the two angled crack front models (B and C), this angle suddenly changes beyond the transition region. In fact the sign K_{II} changes from positive to negative (at $\psi = 180^o$). This occurs due to the shifting of crack propagation direction. The relative magnitude of K_{III} is shown via the second phase angle in Fig. 3.11(b). Here at the mid-plane, $\phi = 90^o$ due to the symmetry condition. In all cases, relative K_{III} increases toward the free-surface. For the crack front B and C models,

a nearly pure Mode III condition (i.e., $\phi = 0^o$) is observed near the transition region. These results are consistent with the shear stress contours shown in Fig. 3.9.

The combined effects of Modes II and III can be shown with the additional phase angle φ, as defined by (3.5). The variations of φ across the crack fronts are shown in Fig. 3.12. Here, regardless of the crack front shapes, the results are nearly identical for all models. In fact the value is always $80^o < \varphi < 90^o$ even along the kinked front except near the free-surface. These results essentially confirm that the shear mode is dominant throughout the crack fronts. Based on the results from the computational model and the observed crack front shape, it is likely that the delamination begins at the corner/free-surface and progresses at an inclined angle as depicted in Fig. 3.6. Using these results, the relationship between the fatigue growth rate and the thermal cycle is described next.

3.4. Fatigue Crack Growth Characterization via Paris Law

As in homogeneous materials, the threshold resistance for fatigue crack growth in a composite material is expected to be less that that under monotonic loading. Here we inspect the fatigue crack growth rate (da/dN) to determine the remaining life or an inspection interval of component [9]. Based on the observed crack growth during thermal cycling and the relationship between the energy release rate and temperature change, the rate of fatigue growth is characterized. Since the local G is not uniform over the inclined or growing portion of the crack front, the average value was chosen from the results of crack front model *C* shown in Fig. 3.10. This value is $G_{ave}/hE^*(\Delta\alpha\Delta T)^2 = 0.20$. Also since the actual crack growth is directed inward as well, the true growth rate is determined by

multiplying the measured crack growth at free-surface by cos 43.5°. The results are listed in Table 3.1.

In order to gauge the three-dimensional effects, a separate interpretation based on 2D model was also made and is listed in the same table. Since the actual 3D crack growth shape cannot be determined, such an *apparent* relation based on a 2D interpretation should be useful in evaluating thermal fatigue growth.

Since a power law equation based on the Paris law is a most common approach to relate the crack driving force and the growth rate, the following formula is considered.

$$\frac{da}{dN} = C\left(\Delta G - \Delta G_{th}\right)^m \tag{3.6}$$

Here C and n are material constants, and ΔG_{th} is the threshold fatigue crack growth toughness. These parameters were obtained using a curve fitting program, and with 3D interpretation, they are, $C = 0.482\times10^{-6}$ [m/cycle(J/m^2)], $m = 0.44$ and $\Delta G_{th} = 12.5$J/m^2. With 2D interpretation, they were $C = 0.869\times10^{-6}$ [m/cycle(J/m^2)^m], $m = 0.44$ and $\Delta G_{th} = 6.9$J/m^2. The observed threshold toughness is more than a magnitude less than the reported interlaminar critical energy release rate for fiber-reinforced composites under Mode II condition which typically exceeds $G_c = 500$J/m^2. These fatigue growth rate results are shown in Fig. 3.13(a), which shows a very good agreement with measured data. Note this fatigue law does not account for the effect of mode mixity. However, since the relative shear mode is nearly constant across the crack fronts as shown in Fig. 3.12, these parameters should be valid for predominantly shear mode condition. The results are also shown in log-log scale plot in Fig. 3.13(b), which also confirm a good

match with the power law model. Additionally, a similar power law model is possible with the stress intensity which yields the exponent as $2m = 0.88$.

3.5. Summary

In typical cross-ply composite laminates, multi-layered arrangements add larger constraint, and an interlaminar crack growth may be more difficult than in the current 2-layer specimen. However magnitudes of thermal stresses generated by CTE mismatch are still similar. Furthermore, if structures are subjected to mechanical loads as well, the likelihood of fatigue crack growth may increase. In addition, other factors including environmental degradation may promote the fatigue crack growth.

In the current study, we fabricated laminate specimens with the vacuum bagging technique so that delamination could be introduced prior to thermal cycling. In practice, delamination may occur due to weak bonding or after repeated mechanical loading and/or under severe environmental conditions. The present tests confirm that such crack can grow under thermal cycles albeit under certain conditions. Examination of the fractured surface revealed complex crack propagation behavior. The path alternated between the 0^o and 90^o laminae. This was probably due to the dominant Mode II condition but it also confirms that a high bonding strength exists between the plies. This adds an assurance that growth under thermal cycling occurred not because of weak adhesion caused by the present fabrication process, but due to inherent stresses in the laminates.

The observation of fractured surfaces also revealed uneven crack growth across the width. Analysis of angled crack front from an initially straight front was made with recourse to a 3D finite element model. First the local/point-wise energy release rate value and the two phase angles were computed along the three-dimensional crack front. Next,

the crack growth rate was correlated with range of energy release rate using a power law relation. Furthermore, a threshold value of range of energy release rate (ΔG_{th}) was estimated, below which there was no crack propagation. Computations show that values for energy release rate are higher for the three-dimensional case as compared to the two-dimensional case for similar thermal loading conditions. Thus a 2D interpretation would offer a conservative estimate for fatigue life of cross-ply laminates submitted to thermal cycling. Nonetheless, while studies on composite laminates might base their investigation on two-dimensional computational analyses for fatigue crack growth characterization, our study reveals that three-dimensional effects play a significant role on the interface crack propagation behavior in such materials.

As noted earlier, the Mode I test under monotonic load measured $G_c = 155 J/m^2$ with the present specimen. This is in line with reported values of interlaminar toughness of $G_c = 100–1{,}500 J/m^2$ [7] for various carbon fibered-reinforced epoxy laminates. In addition corresponding Mode II values are often 2~3 times higher than those of Mode I [7]. However the estimated value of threshold fatigue crack growth was only $\Delta G_{th} = 12.5 J/m^2$ under Mode II dominant condition. This presents, a much smaller temperature change is sufficient to propagate a pre-existing crack under thermal cycles. In fact, the corresponding temperature for threshold is only $\Delta T = 47^{o}C$. Such information should be useful in assessing interlaminar failure resistances of cross-ply laminates.

3.6. References

1. Vaddadi, P. Characterization of fiber-reinforced composites exposed to multiple environments. *Ph.D. Thesis*, Stony Brook University, Stony Brook, NY.
2. Paris, P.C., Gomez, M.P., Anderson, W.E. (1961) A rational analytic theory of fatigue. The Trend in Engineering, **13**(1): 9-14.
3. Vaddadi, P., Nakamura, T., Singh, R.P. (2007). Inverse Analysis to Determine Hygrothermal Properties in Fiber Reinforced Composites. *Journal of Composite Materials*, **41**: 309-334.
4. Heyder, M., Kuhn, G. (2006). 3D fatigue crack propagation: Experimental studies. *International Journal of Fatigue*, **28**(5-6): 627-634.
5. Nakamura, T., Kushner, A., Lo, C.Y. (1995). Interlaminar dynamic crack propagation. *International Journal of Solids and Structures*, **32**(17): 2657-2675.
6. Yang, W., Suo, Z., Shih, C.F. (1991). Mechanics of dynamic debonding. Proceedings of the Royal Society A433. p. 679-697.
7. Daniel IM and Ishai O. (1994). Engineering Mechanics of Composite Materials, Oxford University Press.
8. Nakamura T and Parks, DM. (1989). Anti-symmetrical 3D stress field near the crack front of a thin elastic plate. *International Journal of Solids and Structures,* **25**: 1411-1426.
9. Lansinger J., Hansson T., Clevfors O. (2007). Fatigue crack growth under combined thermal cycling and mechanical loading. *International Journal of Fatigue*,**29**(7):1383-1390.

Table 3.1. Energy release rate and corresponding growth rate at different temperatures. Interpretations based on 3D and 2D models are made.

ΔT (^{0}C)	ΔG (J/m^2)	da/dN (μm/cycle)
3D Interpretation		
30	5.1	0
60	20.6	1.22 ± 0.07
100	57.3	2.69 ± 0.07
120	82.5	3.08 ± 0.07
140	112.0	3.71 ± 0.07
2D Interpretation		
30	2.8	0
60	11.3	1.68 ± 0.07
100	31.5	3.59 ± 0.07
120	45.4	4.25 ± 0.07
140	61.9	5.11 ± 0.07

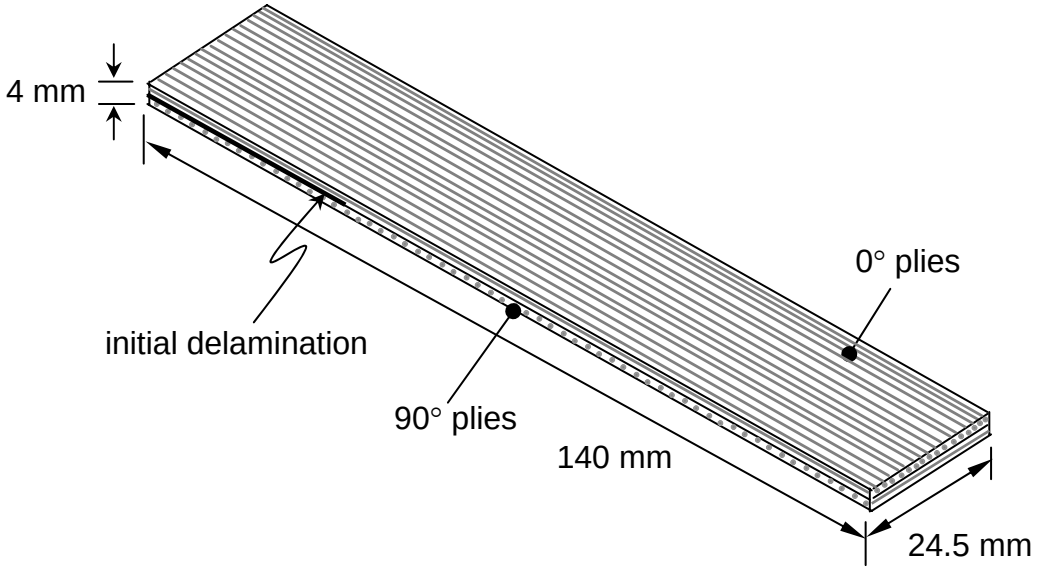

Fig. 3.1. Schematic of composite laminate with pre-existing delamination.

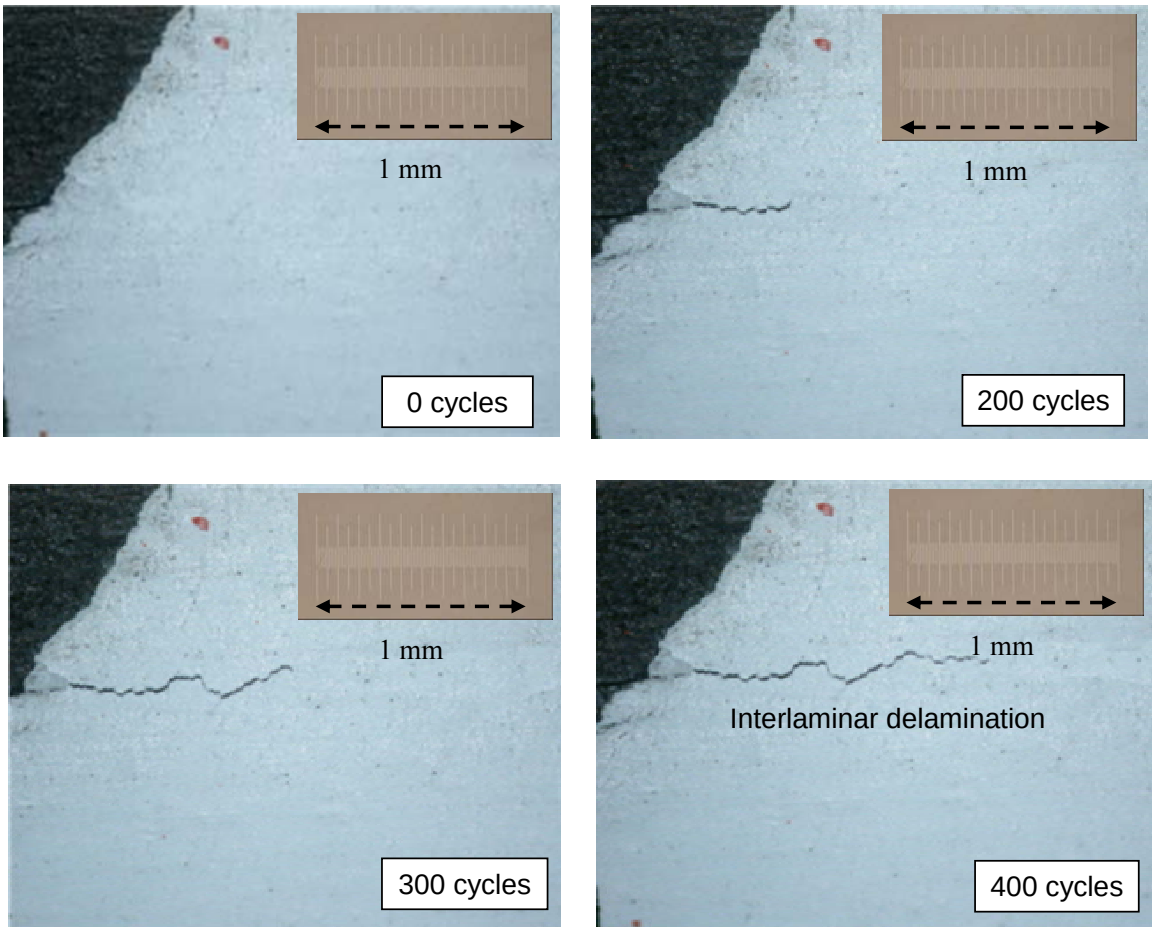

Fig. 3.2. Optical micrographs showing crack growth along the interface between the 0° and 90° plies at different thermal cycles. Specimen is masked with white tape to better show crack.

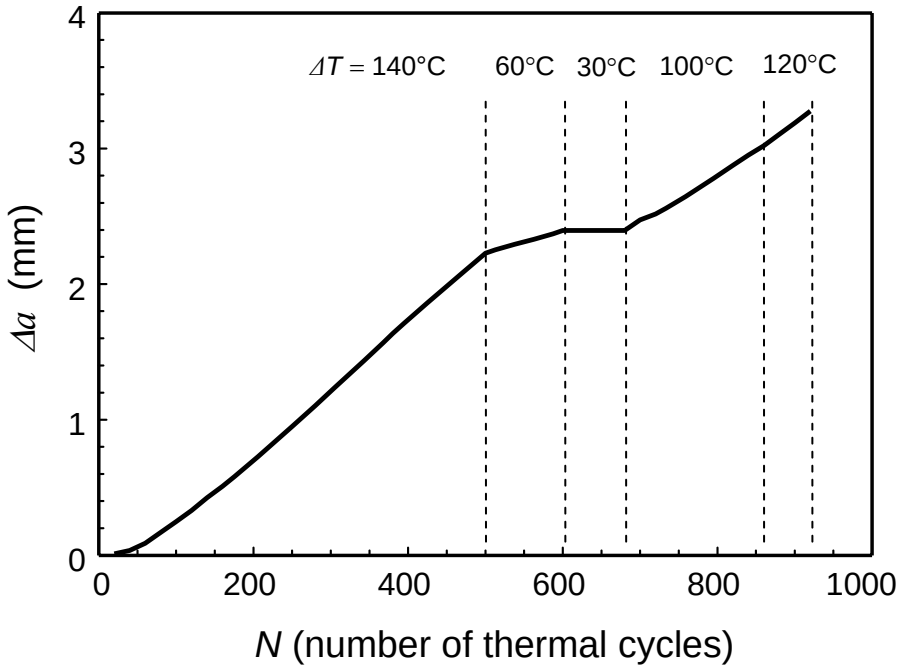

(a)

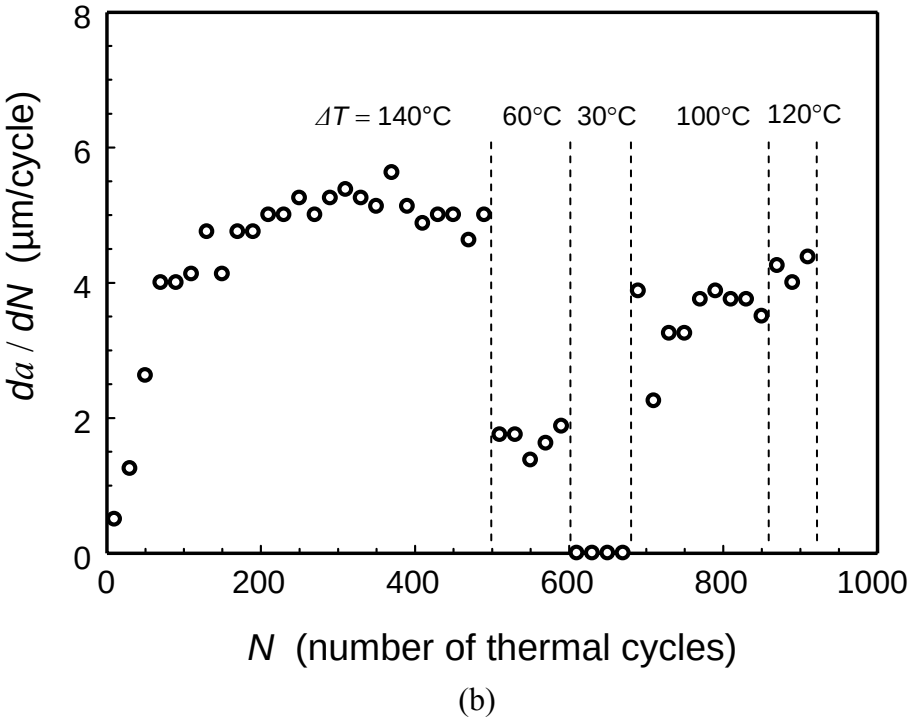

(b)

Fig. 3.3 (a) Average crack length measured at edges shown as a function of thermal cycles. (b) Average growth rate under different amplitude of thermal cycles.

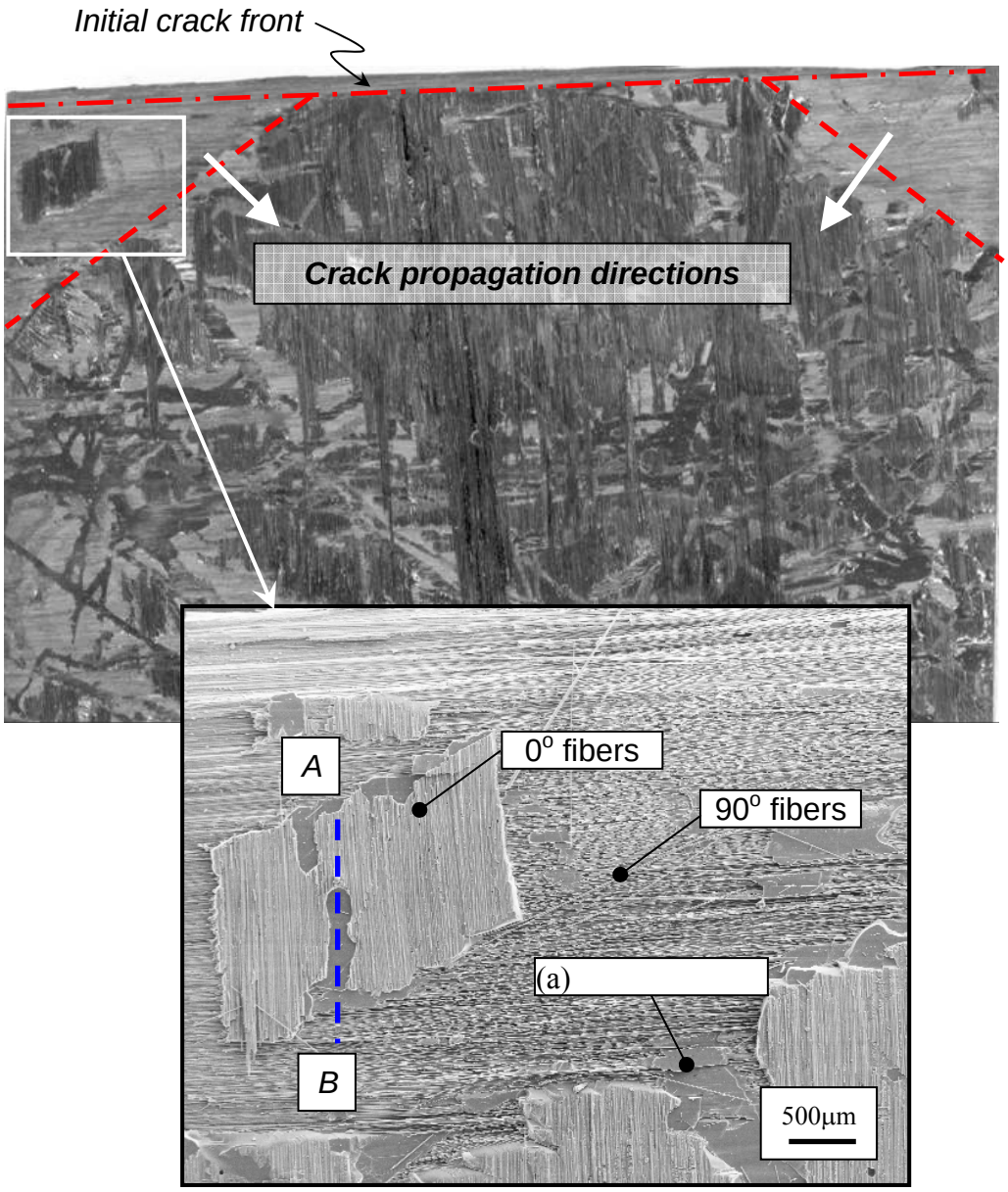

Fig. 3.4. Optical and SEM micrographs showing fractured surface. Estimated crack propagations are indicated. Note the surface exposes fibers in both directions as shown in the enlarged micrograph.

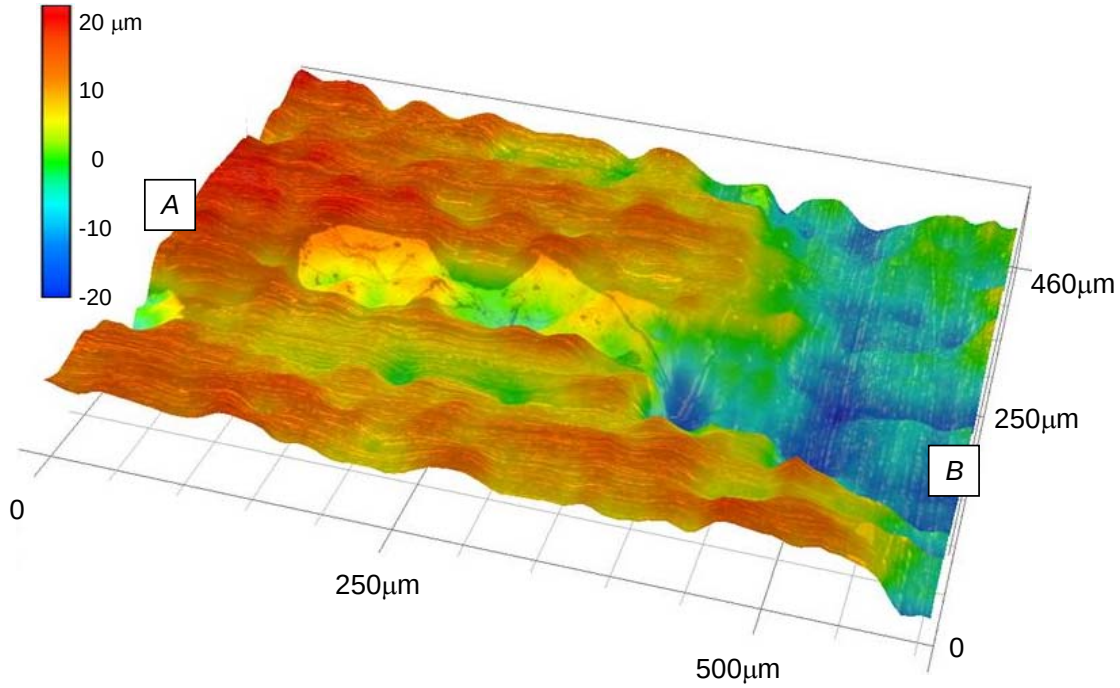

(a)

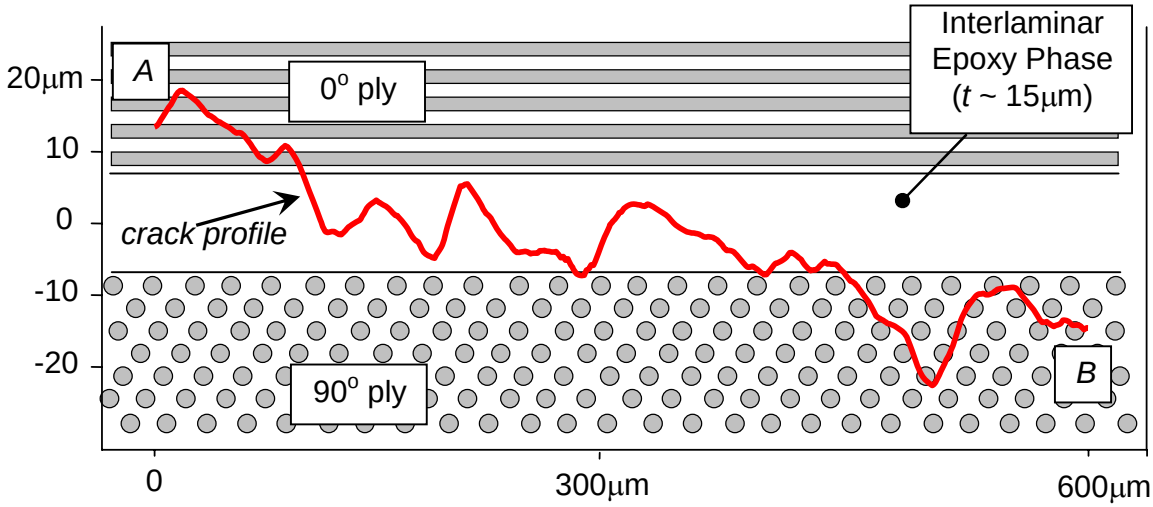

(b)

Fig. 3.5 (a) 3D fractured surface profile measured by Keyence profile microscope near line A-B in Fig. 4. (b). Measured crack profile between line A-B. Profile of different phases are imposed on the graph.

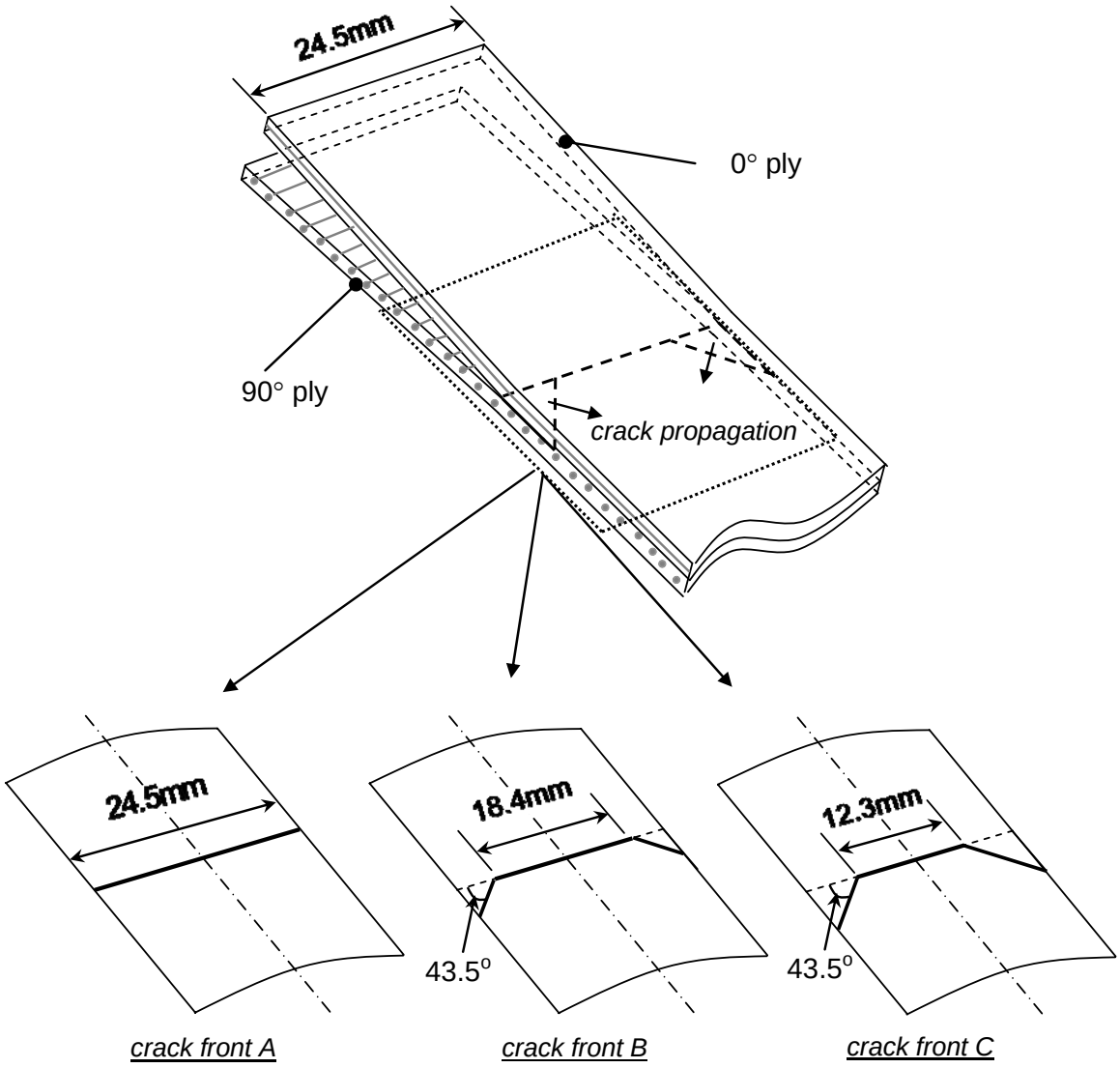

Fig. 3.6. Schematics of a section of the composite model, and three different crack configurations analyzed. Initial stage (crack front A), intermediate stage (crack front B) and final stage (crack front C).

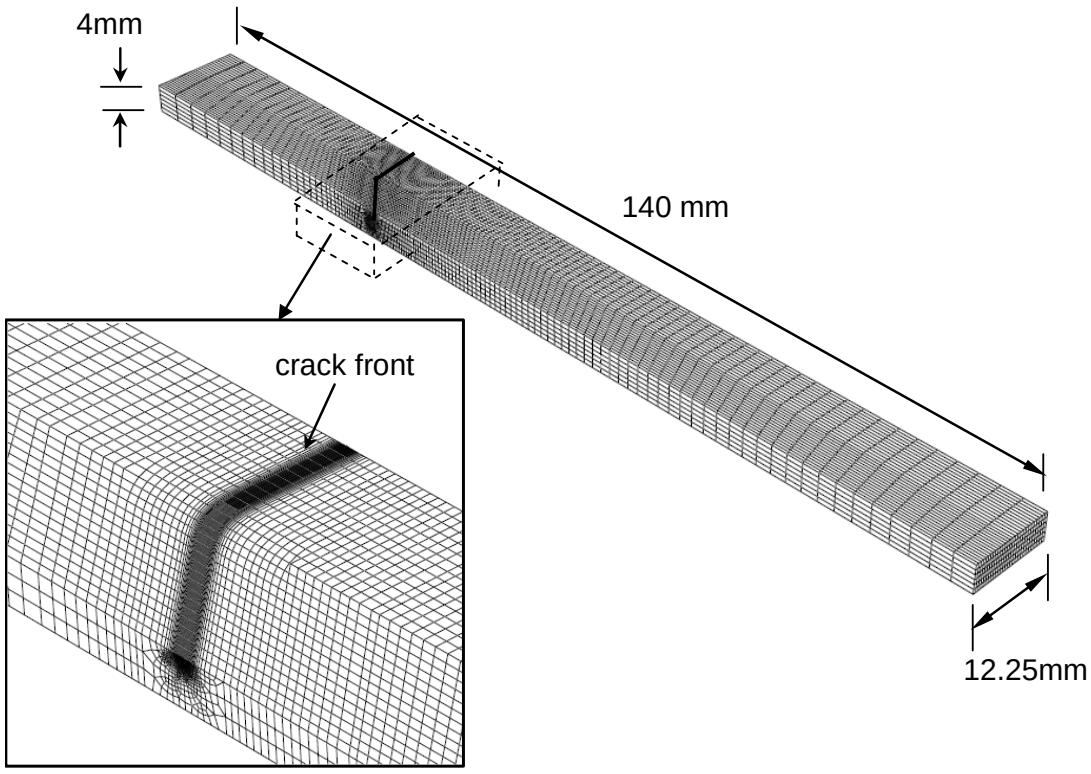

Fig. 3.7. 3D Finite element mesh for crank front C model. A enlarge section of 90^{o} ply (lower layer) exposing the crack front region is also shown.

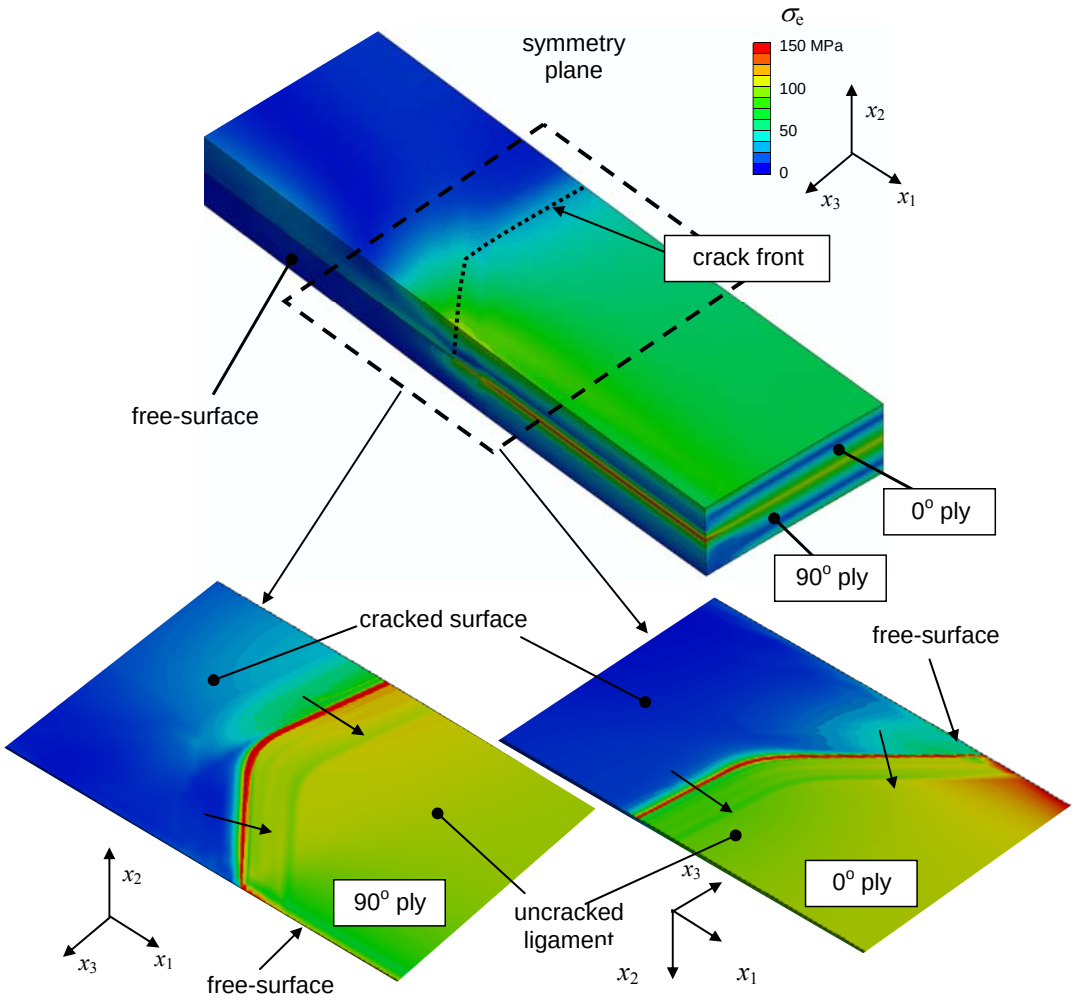

Fig. 3.8. Shades of effective stress near crack front for model C with ΔT = 140°C. The stress on the crack planes for 0° and 90° sides are also shown. Directions of crack growth are also indicated.

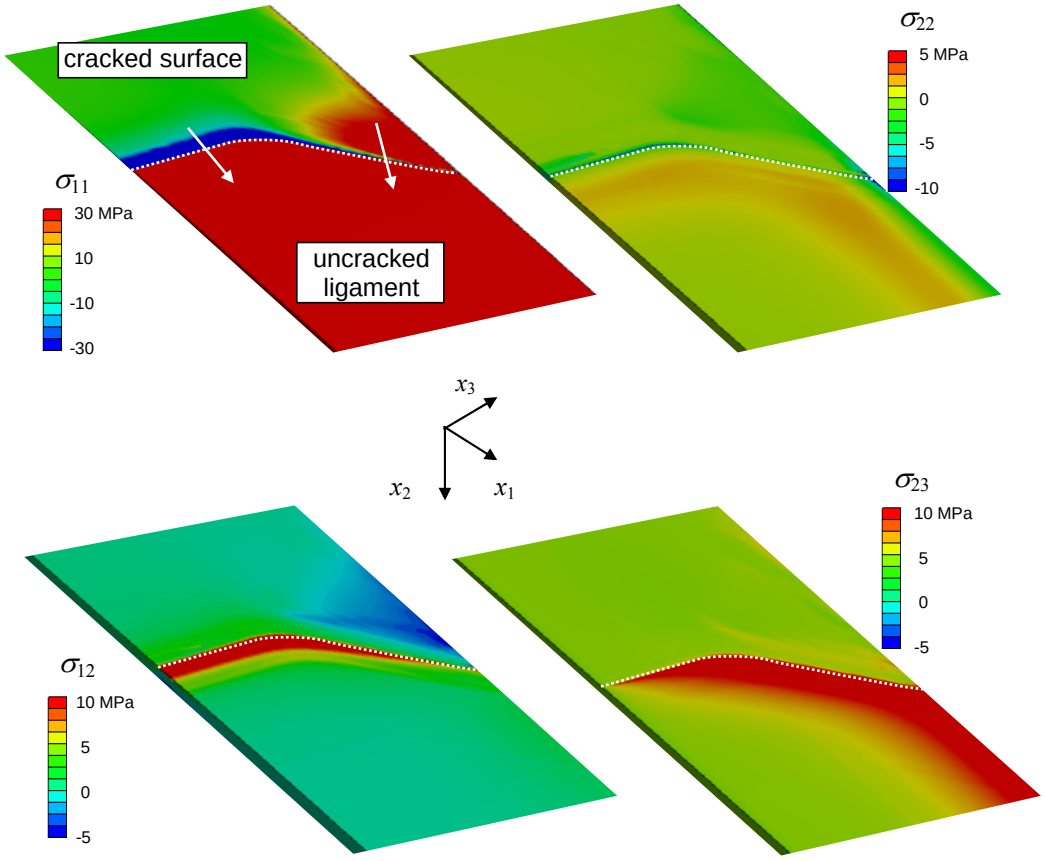

Fig. 3.9. Shades of various stress components on the 0^o ply side of crack plane for model C with $\Delta T = 140^oC$. The stress on are also shown.

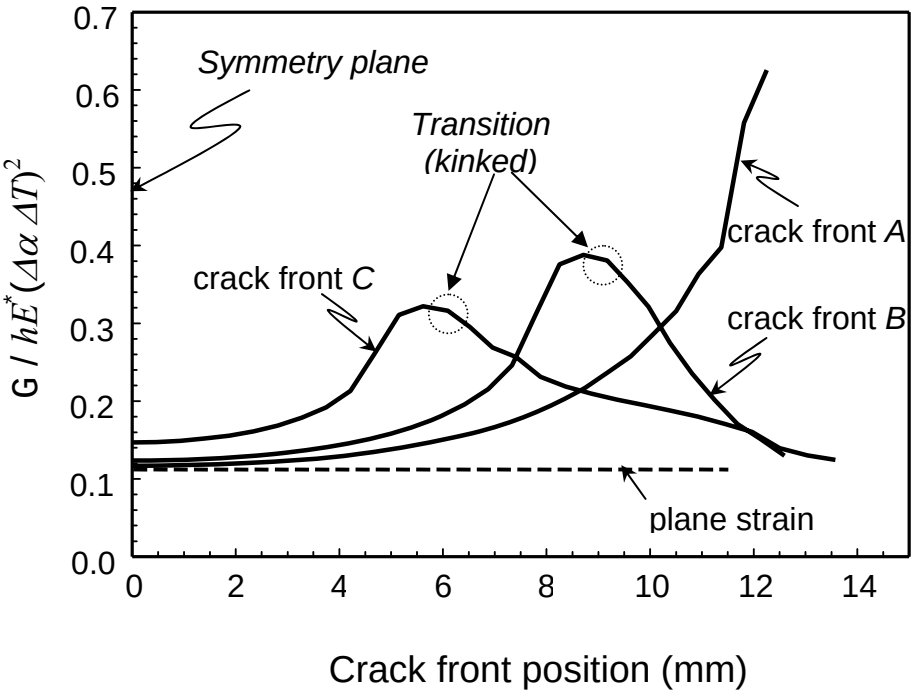

Fig. 3.10. Normalized G along crack front for three different models/stages of growth (*A* to *C*).

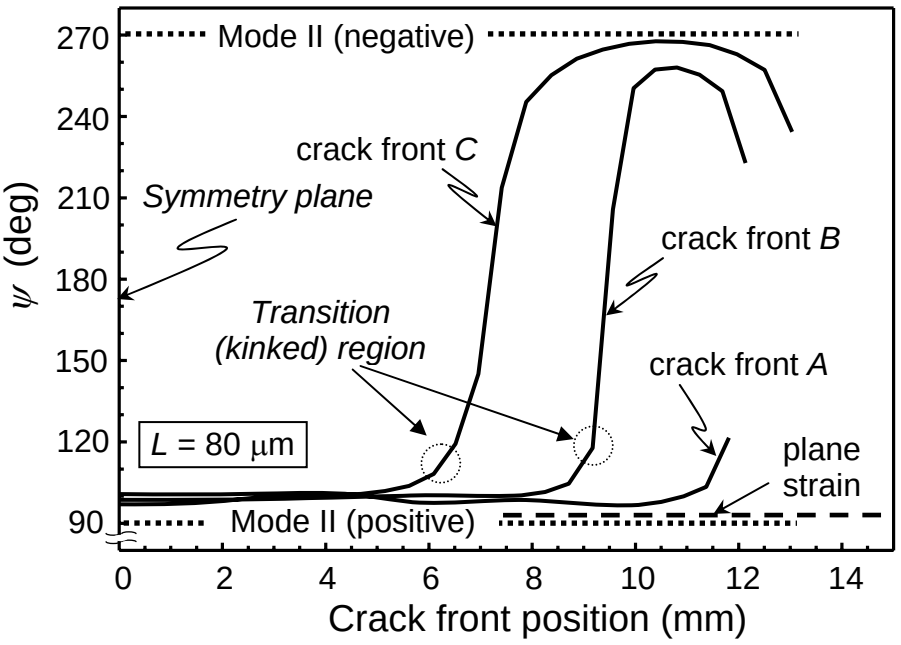

(a)

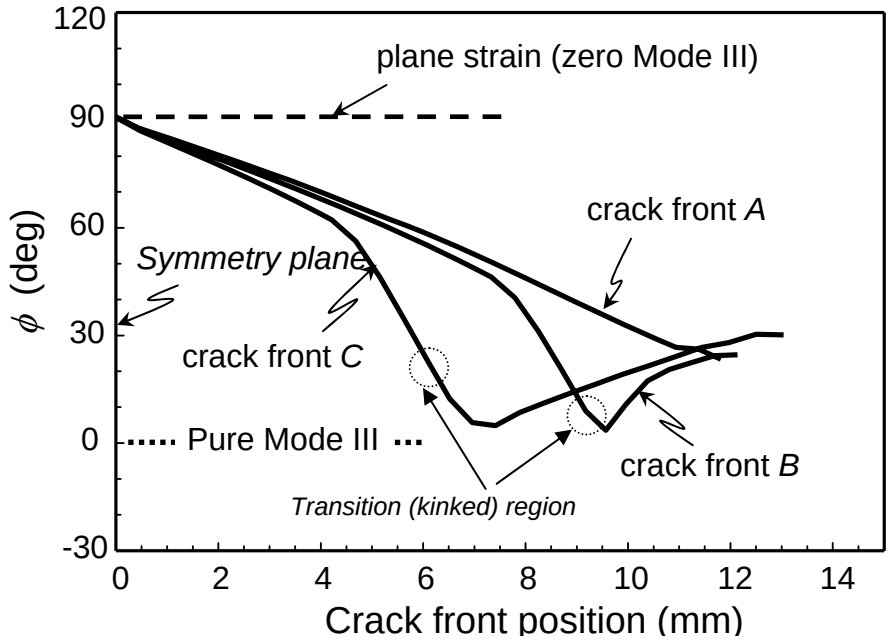

(b)

Fig. 3.11. Phase angle variations along crack front for three different models. (a) In-plane phase angle. (b) Out-of-plane phase angle.

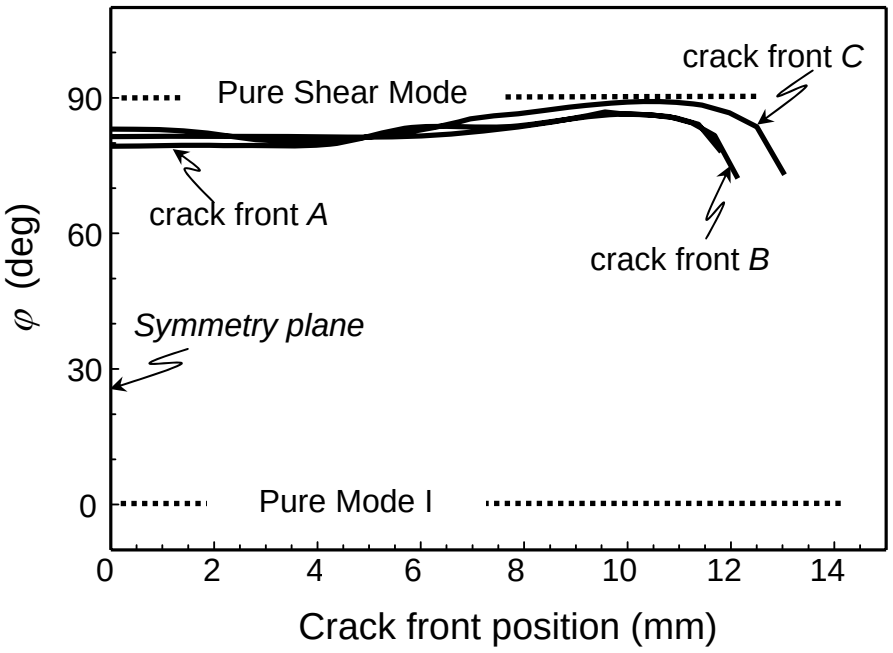

Fig. 3.12. Effective phase angle variation along crack front for three different models.

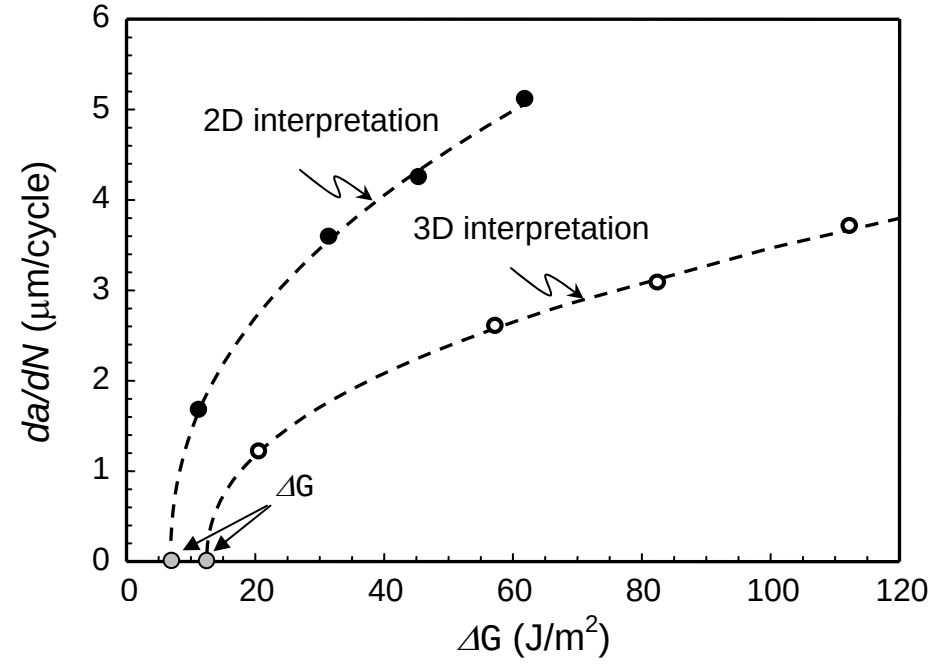

(a)

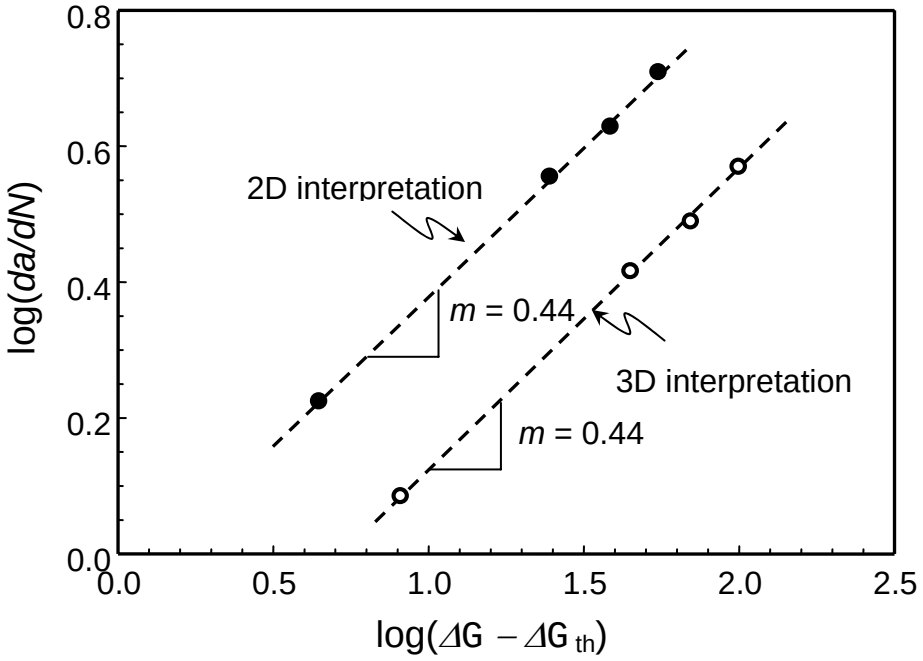

(b)

Fig. 3.13. Measured fatigue crack growth rates shown as function of energy release rate amplitude on (a) regular scales, (b) log-log scales.

4. Solid Particle Erosion of Heterogeneous Materials

4.1. Introduction

The goal of present study is to elucidate the role of ductile phase in heterogeneous materials that are subjected to solid particle erosion. Here erosion tests were conducted experimentally and they were analyzed through particle impact simulations. The test specimens were fabricated by the plasma sprayed technique. Thermally sprayed coatings contain brittle phase (YSZ) and ductile phase (CoNiCrAlY) as well as pores and some oxidized phase. Although many researchers have studied solid particle erosion, they are mostly empirical in nature and the effects of ductile phase were not investigated in depth. Work on ductile phase addition has been undertaken by Yin et al. [1] who studied effects of microstructure on mechanical properties of Al_2O_3-Al composite coatings that are deposited by plasma spraying. They observed a significant improvement in the wear response of the Al_2O_3 coatings due to reinforcements of ductile Al phase. Dong et al. [2] also fabricated Fe_2O_3 –Al self reaction composite powders. Chemical reactions produced Al_2O_3 (brittle) and Fe (ductile) phases. These composite coatings were then subjected to static loading to examine wear properties. They too observed the benefits of ductile phase addition. Chwa et al. [3] studied mechanical properties of plasma sprayed TiO_2-Al composite coatings. Here Al particle were used to reinforce the splat boundaries of TiO_2 phase. The above mentioned studies address wear but not solid particle erosion behavior. Studies of solid particle erosion behavior have been undertaken more comprehensively with ductile phase as matrix however (brittle phase reinforcement). Chen and Li [4] developed micro-scale dynamic models to simulate single particle impact of heterogeneous material to address erosion. Here Cu was

considered to be the matrix phase and SiC, the reinforcing phase. Material removal was modeled with recourse to breaking of cohesive and adhesive bonds similar to present study. Harsha et al. [5] studied solid particle erosion of polyethermide and its composites. They found the detrimental effects of brittle phase (short glass and carbon fibers) on solid particle erosion behavior. Similar studies were undertaken on solid particle erosion of polyphenylenesulphine composites by Sinmazcelik and Taskiran [6] and sand erosion of glass fiber reinforced epoxy composites by Tsuda et al. [7].

Ductile phase addition to predominantly brittle coatings finds useful applications in gasifiers and hot sections of gas turbines. For example, heterogeneous coatings mainly Cr_3C_2-NiCr, NiCr, WC-Co, WC-NiCr, NiCr-St-6 deposited through plasma spray or high velocity oxygen fuel (HVOF) techniques are used for their superior wear and erosion properties in gas turbines, steam turbines and aero engines [8]. In addition arc sprayed brittle coatings having ductile phase are shown to have higher erosion resistance [9].

Other than coatings, ductile phase addition has proven to increase erosion resistance in intermetallic compounds such as $NiAl_3$ in Ni based super alloys. Even though $NiAl_3$ is ductile at high temperatures, they are notoriously brittle at room temperatures. Intermetallic compounds find a wide range of applications as high temperature gas turbine hardware, corrosion resistant materials, heat treatment fixtures, magnetic materials and hydrogen storage materials [10]. Ductile phase additions that are a feature of cermets (ceramic matrix composites) are known to possess higher fracture toughness due to addition of a second ductile phase (eg. [11]). They can be fabricated through a number of procedures including melt processing, hot pressing, slip casting, chemical vapor infiltration and others. These composites find applications ranging from advanced space vehicles to recreational products.

In the present experiments, erosion tests are performed on plasma sprayed coatings with three different contents of ductile phase. They are eroded with alumina particles to measure material removal (mass) rates. Following the experimental results, finite element models are setup to study how a striking particle removes surface material. Models explicitly take into account the heterogeneity of coatings based on SEM image of actual coatings. In the computational analysis, single and multiple solid particle impacts simulate erosion at various velocities and angles. Fracture criteria were imposed within model. The current study is also valuable in understanding foreign object damage (FOD) of thermally sprayed blades, which are used in many gas turbines.

4.2. Erosion Tests

4.2.1. Specimen Description

Specimens in the current study are fabricated by plasma spraying of melted or semi-melted particles of Yttria Stabilized Zirconia (YSZ) and Cobalt-Nickel-Chromium-Aluminum-Yttrium alloy (CoNiCrAlY). Powder morphology used was fused and crushed (FC) for YSZ obtained from Saint Gobain Inc. The size distribution of powder particles was 10-75 μm. For CoNiCrAlY, the nominal size was 5-45 μm and was obtained from Praxair Inc. The spraying distance was set as 100 mm with a powder feed rate of 0.5 g/sec. Specimens were then machined to the dimensions 12.5mm × 25.0mm × 2.0mm for conducting erosion tests. The coating thickness was 0.7mm whereas the substrate made of steel was 1.3 mm thick. Three different coatings with target weight compositions of YSZ phase being 100%, 80% and 60% were sprayed. The ductile phase chosen for reinforcement was CoNiCrAlY.

Scanning electron micrographs (SEM) of cross-section (thickness dimension) of these specimens are shown in Fig. 4.1. The processed SEM image to generate the mesh is highlighted in Fig. 4.2. The computational models are described in detail in Section 4.3. Different colors in the figure corresponding to different phases (YSZ, CoNiCrAlY and oxide mainly Al_2O_3) are highlighted. The additional Al_2O_3 phase formed due to oxidation of aluminum in the ductile CoNiCrAlY phase. The average porosity in these coatings varies between 3% and 6%. Volume/Area fractions computed via image analysis of different phases are shown in Table 4.1. The 3 different coatings are referred to as *YSZ* (100% target weight fraction of YSZ), *YSZ/CoNiCrAlY (A)* (80% target weight fraction of YSZ and 20% target weight fraction of CoNiCrAlY) and *YSZ/CoNiCrAlY (B)* (60% target weight fraction of YSZ and 40% target weight fraction of CoNiCrAlY). As expected, there is an increase in volume fraction of Al_2O_3 phase with increase in volume fraction of ductile phase. Presence of these phases was further confirmed through an energy dispersive spectrometer (EDS) technique.

4.2.2. Erosion Test Setup

Experiments conducted according to the ASTM standard [12] using the erosion test rig is shown in Fig. 4.3. As-sprayed coating surfaces were exposed to alumina particles with irregular polygonal shape whose morphologies are shown in the inset of Fig. 4.3(b) and Fig. 4.3(c). Different parameters employed in the tests are reported below. The nominal particle size of these angular alumina particles is 50 μm. The inner diameter of nozzle is 1.5mm while the nozzle length is 37.5mm. The pressure of fluid (air) flow was chosen as 138 kPa. Further, the mass flow rate of alumina was set as 0.02 g/sec (corresponding to 1 knob rotation). With these settings the velocity of particle impact was estimated to be ~104 m/s. Estimation of velocity here was approximately done through comparison with mass loss

behavior of steel which is well documented in literature [12], and also prior measurement made by Usmani and Sampath [13].

4.2.3. Mass Loss Determination through Experiments

Figure 4.4(a) shows the surface profile of specimen during erosion process. The eroded topography is shown in Fig 4.4(b). Here, a crater of depth ~190 μm can be observed after 40 second exposure to alumina particle impacts. The crater is expected to form due to excessive material removal through cracking and chipping due to huge number of particles striking the coating. From mass flow rate of 0.02g/sec, it was roughly estimated that 80,000 particles (assuming spherical radius of 25 μm) strike the coating surface in 1 second.

Figure 4.5(a) shows mass loss curves obtained from experiments with velocity of impacting particle being 104 m/s. 3 specimens each for 3 coating types of YSZ are tested accounting for a total of 9 specimens. It can be clearly seen that the coating type YSZ shows the maximum amount of erosion with introduction of a metallic phase decreasing the erosion rates drastically. This phenomenon has been observed by Usmani and Sampath [13]. Interestingly, addition of 11% volume fraction of ductile phase (CoNiCrAlY) decreases the erosion mass loss by roughly 50%. For coating type YSZ/CoNiCrAlY (B) the drop in erosion rate is even more pronounced. As expected the YSZ phase is the most susceptible to erosion damage due to its low fracture toughness. Furthermore, micro-structural effects are more pronounced for coating type YSZ compared to other models as seen from the scatter in the plot. From the Fig. 4.5(b), it is evident that mass loss behavior shows a change in slope after an initial period (10 seconds here). Similar observations were reported by Usmani and Sampath [13]. The reason attributed to such a behavior was the polishing of protrusions during initial stages of erosion.

4.3. Computational Procedure

In the current study, finite element models are developed from real micro-structural images. The dynamic impact of particle on coating is simulated until particle rebounded. Cracking leading to fragmentation phenomenon in coatings due to impact from angular particles is modeled by embedding cohesive elements between each element boundary in the vicinity of impact region. However, particle fragmentation itself is not addressed in current study and such an event is less probable since the high impact energy of particle is distributed to the coating. The elastic energy from coating or kinetic energy from individual flying fragments that come into contact with particle would be less compared to the fracture energy of particle. More details of the finite element model are discussed next.

4.3.1. Heterogeneous Models

In current study, the main purpose of setting up computational models is to quantify erosive damage and study the energy evolution characteristics. These models offer interesting insights into the mechanism of distribution of kinetic energy into various other energies in coating. Models for studying fragmentation behavior in heterogeneous coatings are sparse. In homogeneous models, for example, quantification of erosion damage in brittle materials subjected to hard particle impact is analytically solved for erosion volume [14]. Such laws are not available for heterogeneous coatings where fracture properties vary spatially.

Here, finite element models are developed from images of real microstructure obtained using scanning electron microscope. Images for 3 specimens with different compositions of phases are chosen for modeling. These images are converted into a finite element mesh by OOF program developed at National Institute of Standards and Technology

(NIST). Models are created by progressively refining an initially coarse mesh along the interior and interface. 3 noded isoparametric elements are chosen for discretizing the heterogeneous material since they offer more crack paths, directions and better resolution between different phases along interfaces. Next, 4 noded cohesive elements are embedded along all of the 3-noded element boundaries within a large domain (165μm × 55 μm) where material removal can occur as highlighted in Fig. 4.5. Details of the cohesive element formulation are provided in the Section 4.2.3.

The full model with dimensions is illustrated in Fig. 4.6. There are a total of 60000 plane strain elements of which 20000 are cohesive elements. To minimize boundary effects (avoid cracking due to reflection of stress waves from boundary), the heterogeneous region is padded by region with homogenized elements. Material properties are assigned to different phases according to varying colors for heterogeneous region and are reported in Table 4.2. For homogenized elements, average properties obtained through uniaxial tension and compression simulations of heterogeneous phase are used. Contact conditions are enforced between the outer surface of particle and the nodes on the upper portion of mesh to a prescribed depth (55 μm). For comprehensive modeling, contact conditions among fragments forming as a result of impact have to be considered. Such algorithms are sophisticated as the fragments have to be tracked through the course of algorithm. In the current study they are not modeled. Also, the mass density of alumina was scaled by a factor of 3.0 to obtain significant erosion in computational study. As the relevant parameters for modeling erosion are kinetic energy and momentum of particle, the apparent mass scaling should not affect the results qualitatively.

The current scheme considering heterogeneous models offers realistic modeling. However, more comprehensive modeling would require consideration of 3D effects of the problem. Such models are computationally expensive and are not studied. Although 2D finite element models have limitations of not modeling erosion phenomenon comprehensively, they offer valuable qualitative insights to study erosion behavior.

4.3.2. Cohesive Element Formulation for Modeling Brittle Fracture

An embedded process zone (EPZ) model based on traction-separation relation proposed by Xu and Needleman [15] was chosen for simulation of dynamic impact driven multiple crack propagation in heterogeneous materials after various considerations as in the study by Wang and Nakamura [16]. Among other models, are Suo, Shih and Varias (SSV) model [17] based on plasticity free strip, unified model [18] (including EPZ and SSV models), cell model and virtual inter bond [VIB] model [19,20]. EPZ model however provides modeling multiple cracking in arbitrary locations where crack path is not known apriori and is suitable under general conditions. Further, it is easier to implement the EPZ model in a computational code. Hence, in the present study the same model was utilized to simulate erosion caused through cracking and chipping of fragments.

For crack growth under mixed mode condition, Xu and Needleman [15] described a traction displacement relation to model crack nucleation and propagation using a potential function Φ. The function Φ represents the integral of traction over displacement; it is equivalent to the amount of consumed energy due to a growing crack. This function couples both normal and tangential contributions as:

$$\Phi(\delta_n,\delta_t)=\Gamma_o\left\{1+e^{-\delta_n/\delta_n^*}\left[\left(1+\frac{\delta_n}{\delta_n^*}\right)(q-1)-\left(1+\frac{\delta_n}{\delta_n^*}\right)qe^{-(\delta_t/\delta_t^*)^2}\right]\right\}. \tag{4.1}$$

Here, δ_n and δ_t are the components of displacement are normal and tangential to the crack surfaces. δ_n^* and δ_t^* are the reference normal and tangential displacements respectively. The parameters $\Phi_o = e\delta_n^* \sigma_{max}$ and δ_n^* are the two parameters required to specify the constitutive relation for cohesive elements completely. The parameter q defines the ratio of separation energy under pure Mode II to pure Mode I conditions. In present study, parameter q is chosen as 1. A more detailed explanation is given in Wang and Nakamura [16]. The partial derivatives of Φ with respect to δ_n^* and δ_t^* define the components of normal and shear tractions. They are

$$T_n = \sigma_{\max}\left(\frac{\delta_n}{\delta_n^*}\right)e^{\left(1-\frac{\delta_n}{\delta_n^*}-\frac{\delta_t^2}{(\delta_t^*)^2}\right)}$$
$$T_t = 2\sigma_{\max}\frac{\delta_t}{\delta_t^*}\left(1+\frac{\delta_n}{\delta_n^*}\right)e^{\left(1-\frac{\delta_n}{\delta_n^*}-\frac{\delta_t^2}{(\delta_t^*)^2}\right)} \tag{4.2}$$

Differentiating T_n with respect to normal strain δ_n/t_c (t_c-thickness of cohesive element) and evaluating initial elastic modulus by imposing conditions $\delta_n = 0$ and $\delta_t = 0$ at time $t = 0$ from the above equation we get:

$$\left.\frac{\partial T_n}{\partial(\delta_n/t_c)}\right|_{t=0} = \left.\frac{\sigma_{\max}}{t_c}\left(\frac{1}{\delta_n^*}\right)e^{\left(1-\frac{\delta_n}{\delta_n^*}-\frac{\delta_t^2}{(\delta_t^*)^2}\right)}\right|_{t=0} - \left.\frac{\sigma_{\max}}{t_c}\left(\frac{\delta_n}{(\delta_n^*)^2}\right)e^{\left(1-\frac{\delta_n}{\delta_n^*}-\frac{\delta_t^2}{(\delta_t^*)^2}\right)}\right|_{t=0} = \frac{\Phi_o t_c}{(\delta_n^*)^2} \tag{4.3}$$

In current study, initial elastic modulus is set to be equal to the modulus of the element along whose boundaries crack propagation occurs. Here, thickness of cohesive element is chosen to be approximately $l_m/25$ where l_m is the smallest element size (~25×10^{-8} m) for the mesh with 60% YSZ. One of the disadvantages of using an EPZ model is the introduction of artificial

compliance in the model. The cohesive contribution to stiffness needs to be small compared to that of volumetric constitutive relation [21] which imposes the condition that

$$E << \frac{\Phi_o l_m}{\left(\delta_n^*\right)^2} \tag{4.4}$$

The above requirement is met in the present work where elastic modulus is at-least an order of magnitude lesser. The surface separation is assumed to occur when Φ/Φ_o of the cohesive element equals 0.47 typical of brittle materials. To alleviate issues from numerical convergence, in the present analysis, the element is deleted when Φ/Φ_o = 0.90. However, contact between flying fragments resulting from erosion is not considered. Any crushing of fragments trapped between the surface of particle and coating cannot be modeled with current simulation. The parameters chosen for cohesive element are shown in Table 4.3.

4.4. Single Particle Impact Simulations

The mechanism of damage (cracking and chipping) due to erosion of brittle materials can be modeled by a single particle impact striking a smooth surface although there are limitations as described in Section 4.5. However, when ductile phase is predominant in coating, the mechanism of damage is expected to be different (accumulation of plastic strains caused by multiple particle impacts) that cannot be simulated by a single particle impact. Current single particle impact simulations for the coatings typically take about 7 hours to complete. Results of simulation for 3 different types of coatings are discussed next.

Figure 4.7 shows stress shades in coating at different times during the impact process for YSZ coating type. The kinetic energy of simulated particle here is 0.216 J/m (results are reported for 1m through thickness). Removed areas due to erosion are also shown in the

same figure. High stresses are found in coating in vicinity of impact region about 0.15 μs after particle strikes the coating surface and drops beyond this time as particle rebounds from surface. As contact between fragments that result from impact is not modeled these elements are allowed to overlap with intact coating. Figure 4.8 and Fig. 4.9 show evolution of stress during impact of the coating types YSZ/CoNiCrAlY (A) and YSZ/CoNiCrAlY (B). For this kinetic energy of particle, it is observed that there is a decrease in amount of material with increasing compositions of CoNiCrAlY. Stress shades in coating type YSZ for different kinetic energies of particle that correspond to different impact velocities are shown in Fig. 4.10. These results are shown upon completion of impact; when the particle starts to rebound ($t \sim 0.2$ μs). As expected there is an increase in removed areas when kinetic energy of particle is increased.

4.4.1. Variability due to Impact Location

Since**,** the microstructure is heterogeneous it is expected that there should be differences in removed areas depending upon the location of impact of particle. To investigate this dependence, finite element models are performed by impacting at 5 different locations with x/L = {-0.2162, -1.081, 0, 1.081, 0.2162}. L is the total length of the heterogeneous region and here it is 185 μm in length. The 3 different coating types are analyzed.

Figure 4.11 shows the variation in removed areas due to erosion for YSZ. Figure 4.12 and Fig. 4.13 show removed areas for the coatings YSZ/CoNiCrAlY (A) and YSZ/CoNiCrAlY (B) respectively. These removed areas are computed through image analysis technique. From these simulations, erosion/removed areas are similar overall.

However, when simulated particle is located directly over a large pore in the coating underneath, there is an extensive material removal. This happened in 1 out of 5 cases for each coating as seen from the figures. Results reported here are for particle kinetic energy of 0.096 J/m.

4.4.2. Effects of Impact Velocity and Angle

The major parameters for characterizing damage due to impact erosion problems are particle's kinetic energy and momentum, angle of impact, particle shape, material properties of particle and material properties of coating. Here, since the shape of the particle and material properties are set, investigation is done mainly with different kinetic energies of particle and angle of impact.

A total of 8 different impact velocities (v_o) in increments of 25 m/s are chosen ranging from v_0 = 25 m/s to v_0 = 200 m/s. Corresponding kinetic energies of particle range from KE = 0.006 J/m to KE = 0.384 J/m. For coating type YSZ, simulations are run for 3 different locations and 8 different kinetic energies (24 simulations) as they show a greater scatter. For other coating types impact simulations are performed for 1 impact location and 8 different values of kinetic energies. Removal areas for different coating types in Fig. 4.14 indicate trends consistent with experiments for KE > 0.15 J/m. This behavior is further discussed in Section 4.4.3.

Figure 4.15 shows the effect of pores on erosion behavior of the YSZ coatings. The model with pores shows higher erosion areas overall due to networking of cracks to form larger fragments. For model without pores, removed areas are approximately linear with increase in kinetic energies of particle. This result shows the significance of modeling pores

even though there volume fractions are low and underlines the importance of heterogeneous modeling.

The effect of impact angle was investigated as shown in Fig. 4.16. Although only simulated here for coating type YSZ, it was observed that the maximum material removal occurred at impact angle of 90° for homogeneous coating (which is typical response of brittle materials) and about 60º for heterogeneous coatings. Heterogeneous coatings exhibit such a response due to presence of pores near surface and not due to any ductility. Furthermore, many computations at different locations are required for heterogeneous model to be used to comprehensively characterize effects of impact angle of particle on area removed due to erosion. Such sudies can be undertaken in future.

4.4.3. Effects of Various Volume Fractions of Ductile Phase

The main focus of the current study is to determine the effects of reinforcement of ductile phase with the YSZ phase in coatings. These effects were reported by Usmani and Sampath [13] in their experimental study albeit for functionally graded materials. Our study is in good agreement with their findings.

For kinetic energy of particle KE = 0.096 J/m, it is observed in our study that for coating type YSZ/CoNiCrAlY (A) area removed due to erosion is lesser than coating type YSZ. This is consistent with experimental observations. However, YSZ/CoNiCrAlY (B) shows the highest removed areas. From Fig. 4.2, it is seen that this model shows a greater pore volume fraction on the surface compared to other models. Moreover from Fig. 4.14 it is observed that below kinetic energy of 0.15 J/m there is an extensive material removal in coating type YSZ/CoNiCrAlY (B) due to linking up of those pores to form fragments. When

kinetic energy of particle increases, the coating model YSZ/CoNiCrAlY (B) however shows a decrease in erosion area that is consistent with experiments due to greater zone of influence of coating. Ideally, these simulations have to performed with many micro-structural images and results averaged for different kinetic energies. This would require extensive computation times and are not performed in the current study. The overall findings from computational models are in agreement with experimental findings qualitatively.

4.4.4. Energy Evolution Characteristics

One of the advantages of the current simulation studies is the ability to qualitatively examine the conversion of incident kinetic energy from particle into strain energy, kinetic energy (due to formation of fragments and due to the dynamic nature of impact), plastic dissipation (due to presence of ductile phase) and separation energy (due to cracking) in the coating. Such a comprehensive examination is not possible through direct experiments. Energy evolution characteristics are more important while studying foreign object damages (FOD) on coating. Foreign object damage can be modeled by introducing refinements to the current model. However, even for erosion it provides necessary information including duration of impact of single particle and absorbed energy (propensity of substrate to crack).

Energy evolution behavior during the process of impact as computed are shown in Fig. 4.17 for particle kinetic energy (KE=0.024 J/m). As expected, absorbed elastic strain energy drops with increasing amounts of ductile phase for coating types YSZ/CoNiCrAlY (A) and YSZ/CoNiCrAlY (B). Whereas, cracking starts in type A model at roughly the same time as type YSZ, it is interesting to note that peak of strain energy (corresponding to initiation of cracking in coating) is shifted in coating type YSZ/CoNiCrAlY (B) compared to other coating types . Evolution of kinetic energy shows a similar behavior. Separation energy

due to the formation of crack surfaces is low for all of the coating types. Although they are typically 1-2% of the incident kinetic energy, they play a major role in changing the energy evolution characteristics overall. Also separation energy may be higher for models with ductile phase due to limited cracking of the oxide phase and ductile phase that have higher fracture energies. The kinetic energy of YSZ model is highest and indicates higher fragmentation. Independent computations showed that about 80% of the kinetic energy in coating is due to formation of fragments. A major portion of energy is spent due to plastic dissipation for coating YSZ/CoNiCrAlY (B) due to the presence of 30% ductile phase. For protecting substrates it is desirable to have the coating dissipate as much energy as possible [16]. These are energies due to plastic dissipation and kinetic energy carried by flying fragments. Addition of ductile phase is seen to decrease energy absorption in coating (YSZ coating type shows the maximum absorbed strain energy making substrate susceptible to crack).

Figure 4.18 and Fig. 4.19 elucidate the energy evolution characteristics for kinetic energies of particle KE = 0.096 J/m and KE = 0.216 J/m. The percentage strain energy of coating drops with increasing kinetic energy of particle. Also, more fragmentation of coating is observed for higher particle kinetic energies. There is a 5-10% increase in fractional kinetic energy of coating when kinetic energy of particle is quadrupled. Normalized plastic dissipation remains almost the same for coating type YSZ/CoNiCrAlY (A) with increase in particle kinetic energy whereas for coating type YSZ/CoNiCrAlY (B), it increases marginally (~10%) for KE=0.096 J/m compared to KE=0.024 J/m. For KE=0.216 J/m, however there is no further improvement in plastic dissipation. These figures should aid in the understanding of energy transfer from particle to coating qualitatively.

4.5. Multiple Particle Impact Simulations

Multiple particle impact offer insight into the effects of residual stresses (elastic and plastic) in the coating on subsequent particle impacts. After a single particle impact, there are residual plastic deformations in the ductile phase and elastic energy stored in the coating. Single particle impact is incapable of capturing this phenomenon. Furthermore, estimation of mass loss due to erosion from a single particle impact to a highly eroded surface as done by previous studies is at best approximate. The damage caused by every particle should be similar in order for the estimation in the above mentioned manner. Two difficulties with the above procedure are that the particles are assumed to not be in contact with each other and that the patterns from multi-particle impact are assumed to be similar to those when a single particle strikes a smooth surface. Here, it is less likely for two particles to come into contact with each other as the current setup follows ASTM standard. Investigation of material removal from multiple particles on a subsequently eroded surface is done through computational modeling of dynamic impact of up-to 5 simultaneous particles. In the current study accommodating more particles would not only increase computation times but also affect stability of computation. The present problem is unstable as it models a high speed dynamic event. Furthermore, cohesive elements and pores present in the current model offer additional difficulties.

The locations of particles are shown in Fig. 4.20 for the model coating type YSZ. The first particle to strike coating surface is assumed to be at the center. The locations and sequence of other particles are chosen randomly with maximum distance from center of model being $\pm$ 25 μm. Material removal at different times are shown at different times after

each particle impact. After 5 particles successive particle impacts, the area removed due to erosion is computed as 4.29×10^{-10} m^2 (about 4-5 times area removed by single particle impact referring to Fig. 4.14). Figure 4.21 shows simultaneous particle impact for coating type YSZ/CoNiCrAlY (B). Here, even though the first particle removes lesser material compared to YSZ, simultaneous impacts remove more material than for YSZ. The final area removed due to erosion is 6.75×10^{-10} m^2 (about 6-7 times area removed by single particle impact referring to Fig. 4.14). Figure 4.22 shows the comparison between removed areas due to single particle impacts and multiple particle impacts respectively. Complexities do arise from particles striking eroded surface when compared to those striking smooth surface. Additional complications arise due to presence of pores in microstructure. For YSZ model, there was also a pore beneath the region of impact for first particle. For such kinetic energies single particle impact predict a lower material removal for YSZ compared to YSZ/CoNiCrAlY (B) however. It would be interesting to see erosion results for multi-particle impact at higher particle kinetic energy to observe consistencies with experiments. Here the main intention was to demonstrate the feasibility of simulating multi-particle impact.

4.6. Comparisons between Experiments and Computational Model

Current 2D finite element models do not capture three dimensional nature of material removal that is caused due to real erosion phenomenon. However, quantitative correlations obtained in the present study show good correlations of the computational study with experiments.

Single particle impact was consistent overall with experiments. Increase in ductile phase led to decrease in material removal. At lower kinetic energies, coating type

YSZ/CoNiCrAlY (B) showed highest material removal where there is discrepancy with experiments. However, at higher kinetic energies and overall, computational models are able to predict the trend obtained from experiments that addition of ductile phase improves the erosion resistance of coatings. Multiple particle impact studies were undertaken to prove the applicability of current procedure to model impact of eroded surface. For more accurate computations, detailed investigation has to be undertaken with careful assignment of properties, constructing 3D models with multiple particles of various shapes and sizes and modeling fluid flow through which particles travel. Such studies could be undertaken in future. Currently, models developed offer useful qualitative insight into the erosion phenomenon in coatings.

4.7. Summary

The present study addresses the problem of erosion in heterogeneous material systems that may be employed in hot sections of gas turbines. It is found here that addition of ductile phase lead to significant drop in erosion rates. First, experiments were performed for coatings with three different compositions of YSZ phase. Next, 2D finite element models were setup for analyzing the erosion as a dynamic impact problem.

The new features and key observations of the present study are as follows:

- Addition of ductile phase in brittle material phase in coatings leads to an appreciable drop in erosion rates. Here, it was found that there is approximately 50% drop in erosion rates due to 11% addition in volume fraction of ductile phase.

- Computational models are developed from real micrographs to simulate erosion of heterogeneous coatings. The main mechanism of damage in brittle materials occurs through cracking and chipping that is modeled using cohesive elements along element boundaries.

- Current simulation studies examine evolution of various energy components in coating during the particle impact process. This information is necessary for designing coatings to minimize energy absorption in order to protect the underlying substrate from cracking.

- Computational modeling is in agreement with experimental trends for material removal. Simulations offer benefits for qualitatively predicting erosion behavior for wide range of particle kinetic energies and impact angles. Furthermore they can accommodate different heterogeneous material systems as long as the predominant phase is brittle.

Prior to implementing present computational procedure to model actual erosion in coatings comprehensively, further refinements are essential. First, 3D finite element models need to be developed for accurate determination of volume removal. Next, cohesive element parameters especially for various interfaces between brittle and ductile phases need to be accurately evaluated. However, current simulations can model the damage mechanisms in brittle materials in addition to providing an approach to erosion modeling in heterogeneous material systems/coatings. Hence they should be useful in qualitative evaluation of erosion in different heterogeneous material systems.

4.8. References

1. Yin, Z., Tao, S., Zhou, X., Ding, C. (2007). Microstructure and mechanical properties of Al2O3-Al composite coatings deposited by plasma spraying. To appear in *Applied Surface Science*.

2. Dong, Y., Yan, D., He, J., Li, X., Feng, W., Liu, H. (2003). Studies on composite coatings prepared by plasma spraying Fe2O3–Al self-reaction composite powders. *Surface Coatings and Technology*, **179**(2-3): 223-228.

3. Chwa, S.,O., Klein, D., Toma, F.L., Bertrand, G., Liao, H., Coddet, C., Ohmori, A. (2005). Microstructure and mechanical properties of plasma sprayed nanostructured TiO2–Al composite coatings. *Surface Coatings and Technology*, **194**(2-3): 215-224.

4. Chen, Q., Li, D.Y. (2003). Computer simulation of solid-particle erosion of composite materials. *Wear*, **255**(1-6): 78-84.

5. Harsha, A.P., Thakre, A.A. (2007). Investigation on solid particle erosion behavior of polyetherimide and its composites. *Wear*, **262**(7-8): 807-818.

6. Sinmazcelik, T., Taskiran, I. (2007). Erosive wear behaviour of polyphenylenesulphide (PPS) composites. *Materials and Design*, **28**(9): 2471-2477.

7. Tsuda, K., Kubouchi, M., Sakai, T., Saputra, A.H. and Mitomo, N. (2006). General method for predicting the sand erosion rate of GFRP. *Wear*, **260**(9-10): 1045-1052.

8. Murthy, J.K.N., Venkataraman, B. (2006). Abrasive wear behavior of WC–CoCr and Cr3C2–20(NiCr) deposited by HVOF and detonation spray processes. *Surface and Coatings Technology*, **200**(8):2642-2652.

9. Venugopal, K., Agrawal, M. (2007). Evaluation of arc sprayed coatings for erosion protection of tubes in atmospheric fluidised bed combustion (AFBC) boilers. To appear in *Wear*.

10. Stoloff, N.S., Liu, C.T., Deevi, S.C. (2000). Emerging applications of intermetallics. *Intermetallics*, **8**(9-11): 1313-1320.

11. Cook, B.A., Russell, A.M., Harringa, J. L., Slager, A. J, Rohe, M. T. (2004). A new fracture-resistant binder phase for use with $AlMgB_{14}$ and other ultra-hard ceramics. *Journal of Alloys and Compounds*, **366**(1-2): 145-151.

12. ASTM G76-04. (2004). Standard test method for conducting erosion tests by solid particle impingement using gas jets. *ASTM International*.

13. Usmani, S., Sampath, S. (1996). Ambient and Elevated Temperature Erosion Behavior of Duplex and Graded Ceramic Coatings. *Journal of Metals*, **48**(11): 51-55.

14. Evans, A.G., Gulden, M.E., Rosenblatt, M. (1978). Impact damage in brittle materials. In: Proceedings of the Royal Society of London. Series A, Mathematical and Physical Sciences, Volume 361, Issue 1706, p. 343-365.

15. Xu, X.P., Needleman, A. (1994). Numerical simulations of fast crack growth in brittle solids. *Journal of Mechanics and Physics of Solids*, **42**(9): 1397–1434.

16. Wang, Z., Nakamura, T. (2004). Simulations of crack propagation in elastic-plastic graded materials. *Mechanics of Materials*, **36**(7): 601-622.

17. Suo, Z., Shih, C.F. and Varias, A.G. (1993). A theory of cleavage cracking in the presence of plastic flow. *Acta Metallurgica,* **41**(5): 1551–1557.

18. Wei, Y. and Hutchinson, J.W. (1999). Models of interface separation accompanied by plastic dissipation at multiple scales. *International Journal of Fracture*, **95**(1-4): 1–17.

19. Gao, H. and Klein, P. (1998). Numerical simulation of crack growth in an isotropic solid with randomized internal cohesive bonds. *Journal of Mechanics and Physics of Solids*, **46**(2): 187–218.

20. Klein, P. and Gao, H. (1998). Crack nucleation and growth as strain localization in a virtual-bond continuum. *Engineering Fracture Mechanics*, **61**(1): 21–48.

21. Falk, M.L., Needleman, A., Rice J.R. (2001). A critical evaluation of dynamic fracture simulations using cohesive surfaces. In: 5th European Mechanics of Materials Conference in Delft, Netherlands.

Table 4.1. Volume fractions of constituent phases of 3 different coatings through scanning electron microscope (SEM) image analysis.

Coating Types	Composition (%)			
	YSZ	CoNiCrAlY	Al_2O_3	Porosity
YSZ	95 ± 1	0	0	6 ± 2
YSZ/CoNiCrAlY (A)	82 ± 2	11 ± 1	5 ± 1	3 ± 1
YSZ/CoNiCrAlY (B)	53 ± 2	30 ± 1	14 ± 2	5 ± 1

Table 4.2. Material properties for different phases of the heterogeneous coating.

Phases	E (GPa)	ν	σ_o (GPa)	H (GPa)	ρ (Kg/m^3)
YSZ	140	0.25	-	-	6000
CoNiCrAlY	120	0.25	0.230	50	7300
Al_20_3 (oxide layer)	250	0.22	-	-	3960
Homogeneous Phase	130	0.25	0.238	90.1	5845
Solid Particle (Al_20_3)	375	0.22	-	-	11700

Table 4.3. Cohesive element parameters for different phases of heterogeneous coating.

Phases	Φ_o (J/m^2)	δ_n^* ($\times 10^{-9} m$)
YSZ	10	0.845
CoNiCrAlY	100	2.89
Al_20_3 (oxide layer)	10	0.632
Interface 1(YSZ & CoNiCrAlY)	30	1.519
Interface 2 (YSZ & Al_2O_3)	10	0.716
Interface 3 (CoNiCrAlY & Al_2O_3)	30	1.27

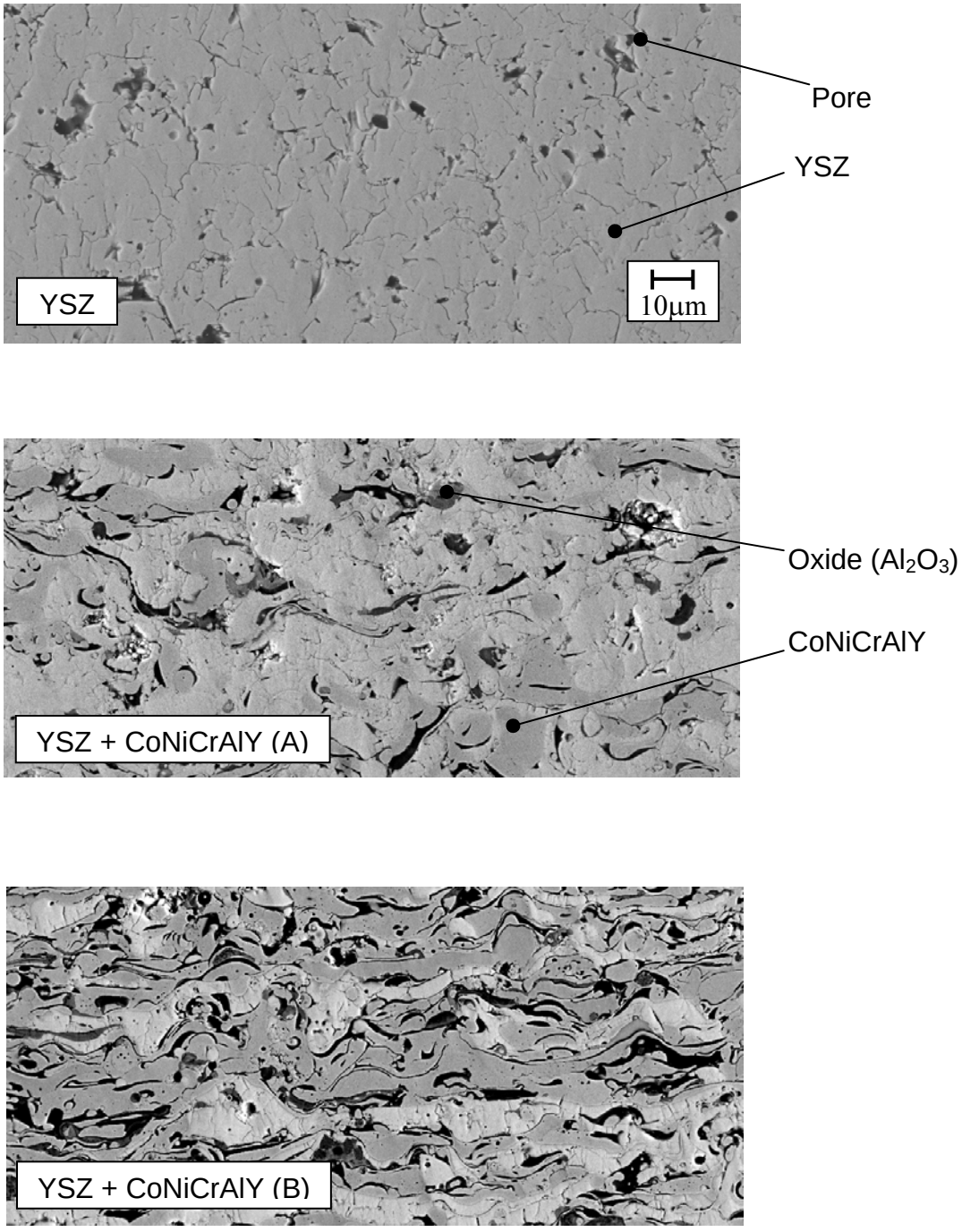

Fig. 4.1. SEM micrographs highlighting various compositions of TS coating.

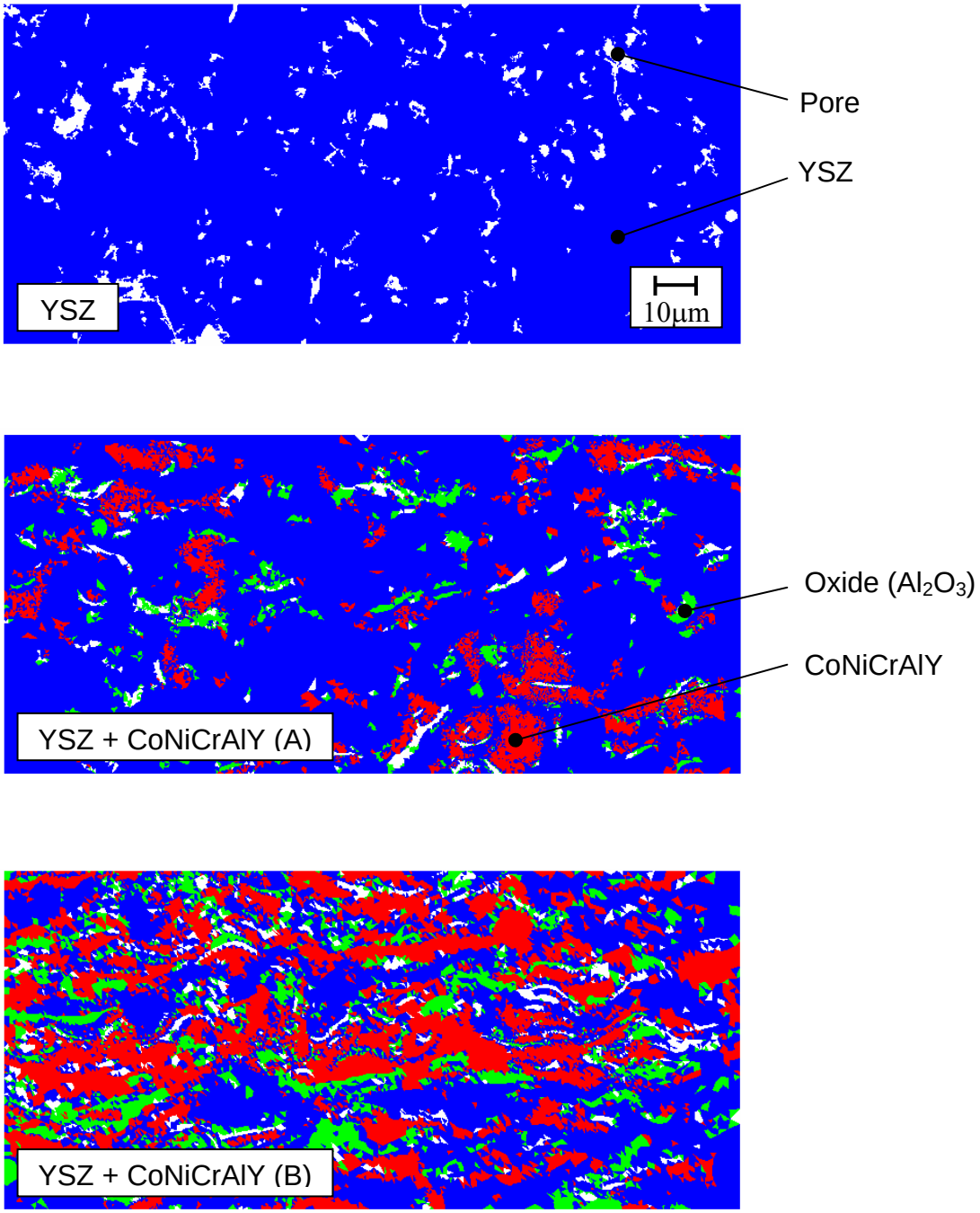

Fig. 4.2. Processed SEM micrographs highlighting various compositions of TS coating.

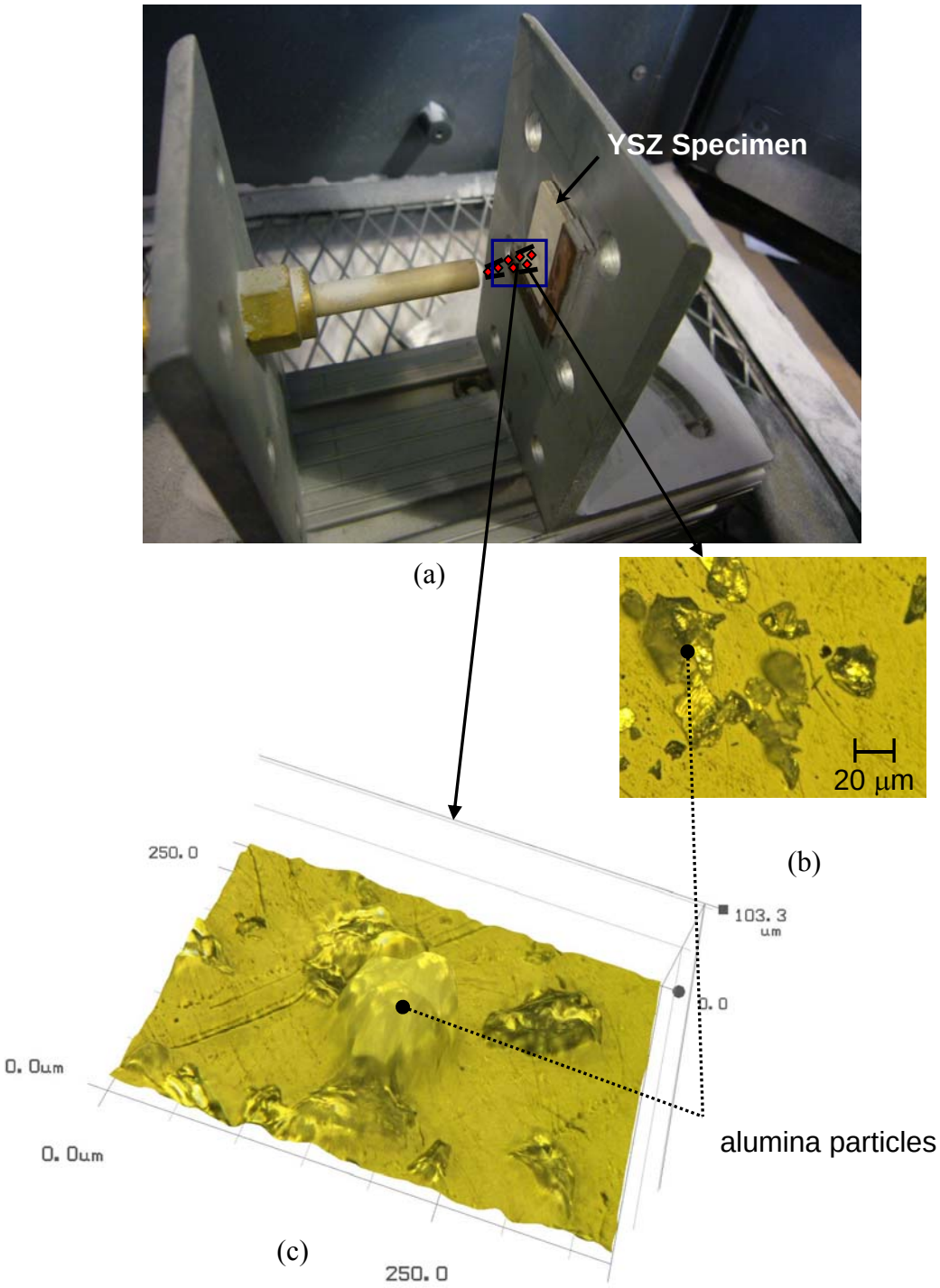

Fig. 4.3. (a) Experimental set up of erosion test rig to conduct solid particle impact tests on coatings. (b) 2D view of alumina particles (c) 3D surface profile of the angular particles.

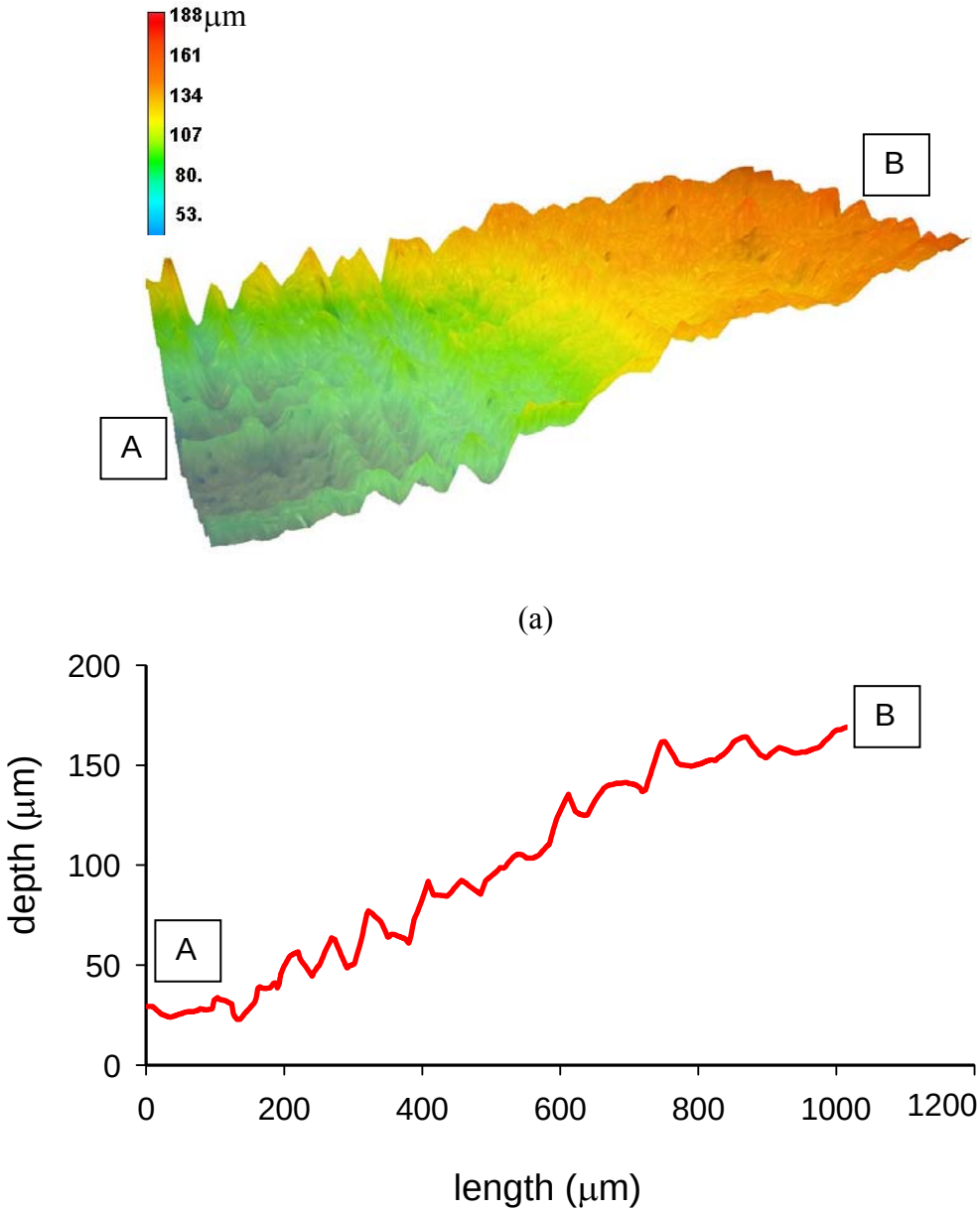

Fig. 4.4. Post erosion image showing YSZ coating. (a) 3D profile showing a part of crater (b) Surface topography measurements showing relative depth variations between points A and B.

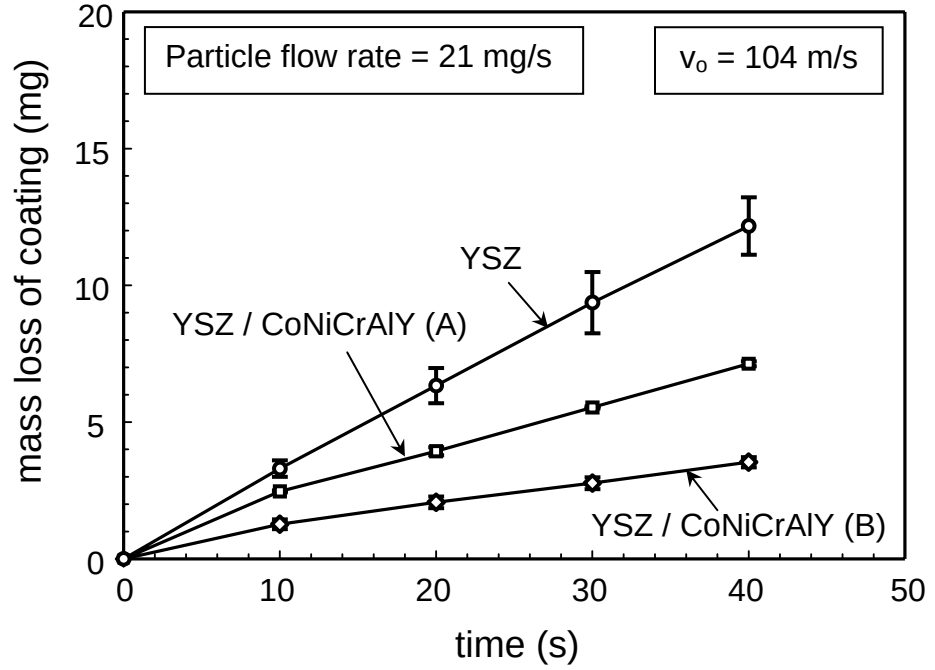

(a)

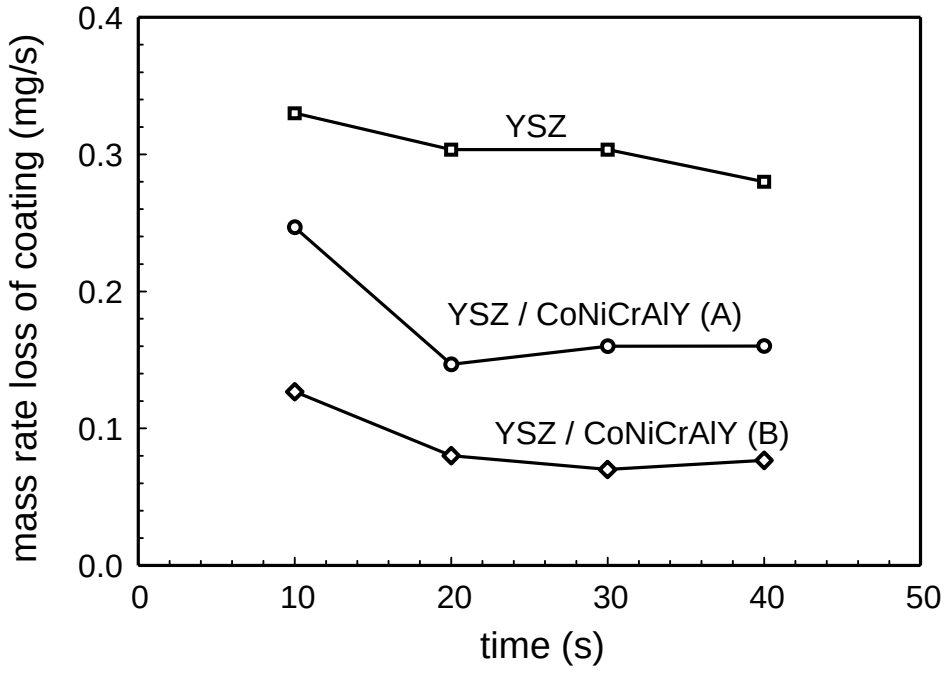

(b)

Fig. 4.5 (a) Mass loss for different coating types with respect to time. (b) Mass loss rate obtained by differentiating the above curve with respect to time.

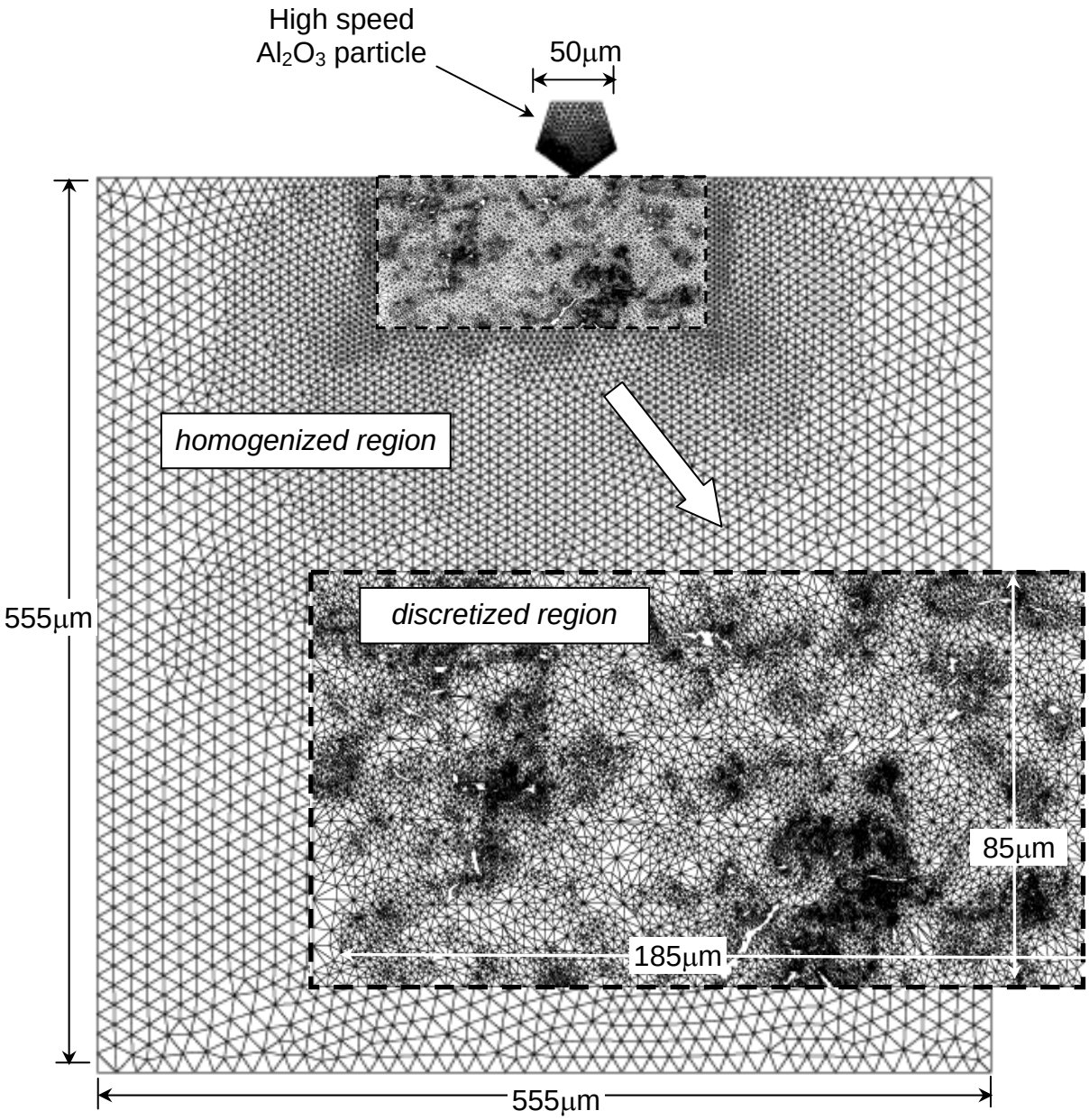

Fig. 4.6. Finite element mesh for erosion simulation. Near the particle impact, the coating is modeled as heterogeneous media with discrete phases (shown for YSZ+CoNiCrAlY(A) model) while the coating is modeled as homogeneous material further away.

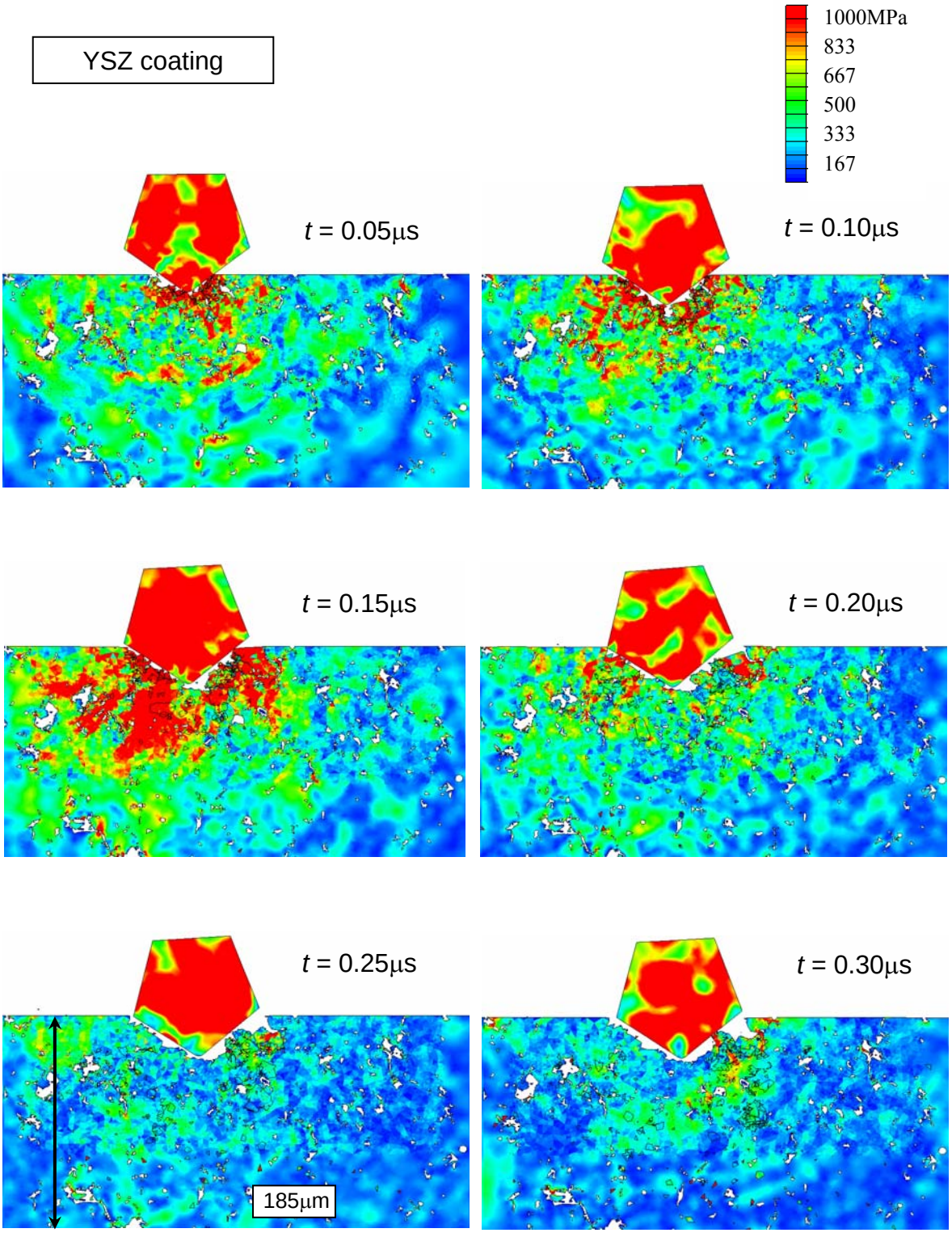

Fig. 4.7. Shades of effective stress showing progression of erosion in YSZ coating by an impacting particle with kinetic energy, KE = 0.216J/m (v = 150m/s).

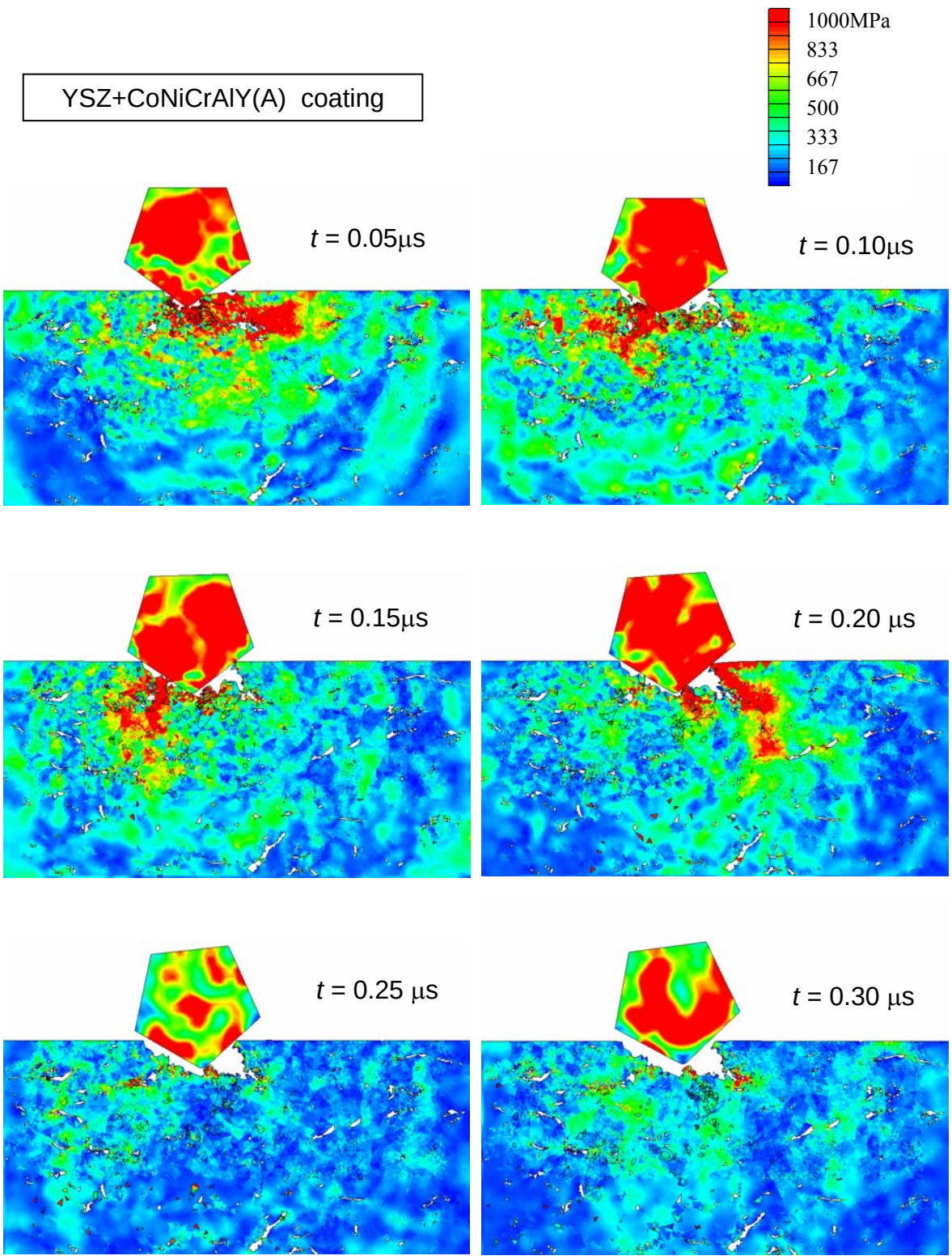

Fig. 4.8. Shades of effective stress showing progression of erosion in YSZ/CoNiCrAlY (A) coating by an impacting particle with kinetic energy, *KE* = 0.216J/m (v = 150m/s).

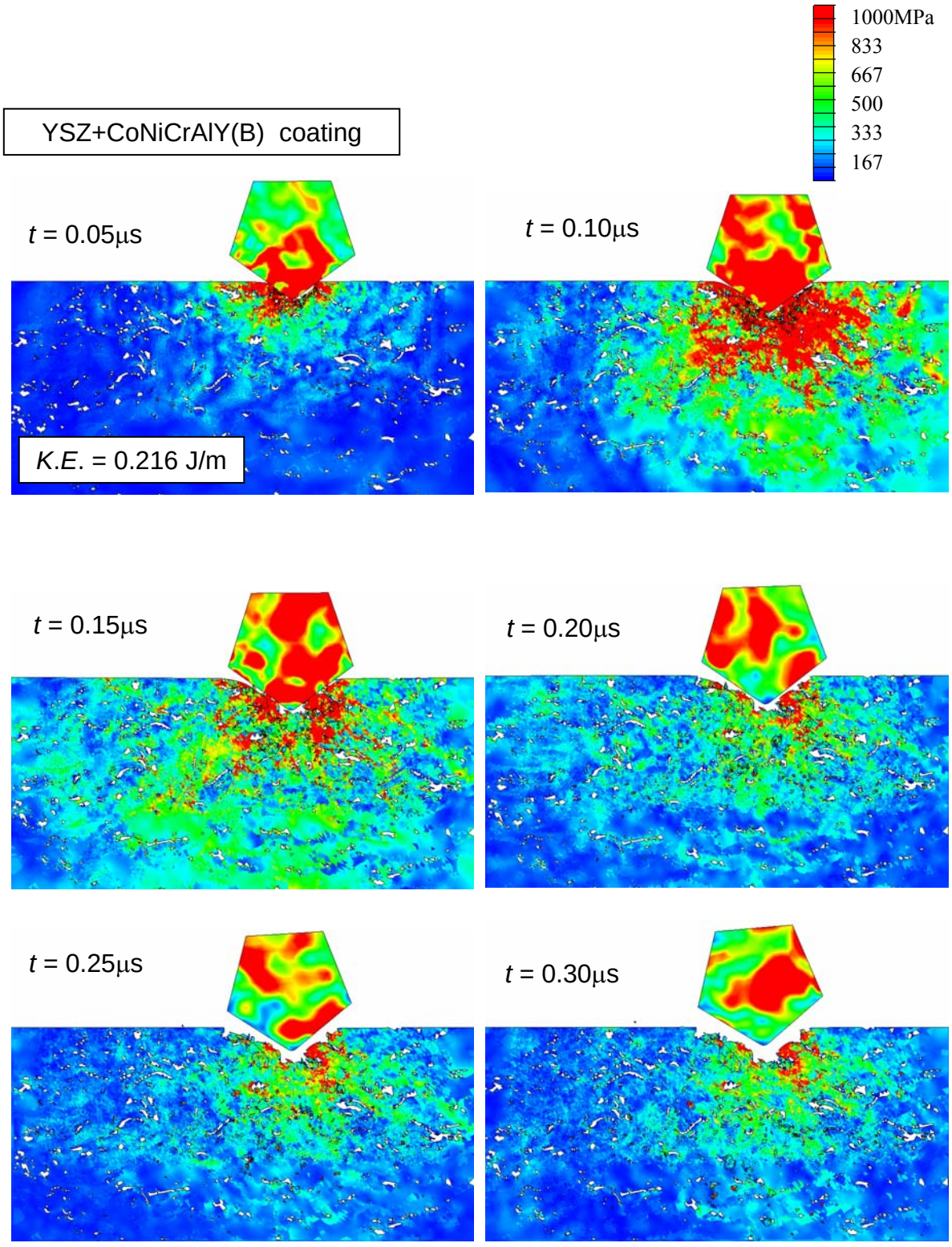

Fig. 4.9. Shades of effective stress showing progression of erosion in YSZ/CoNiCrAlY (B) coating by an impacting particle with kinetic energy, *KE* = 0.216J/m (v = 150m/s).

Eroded Profiles

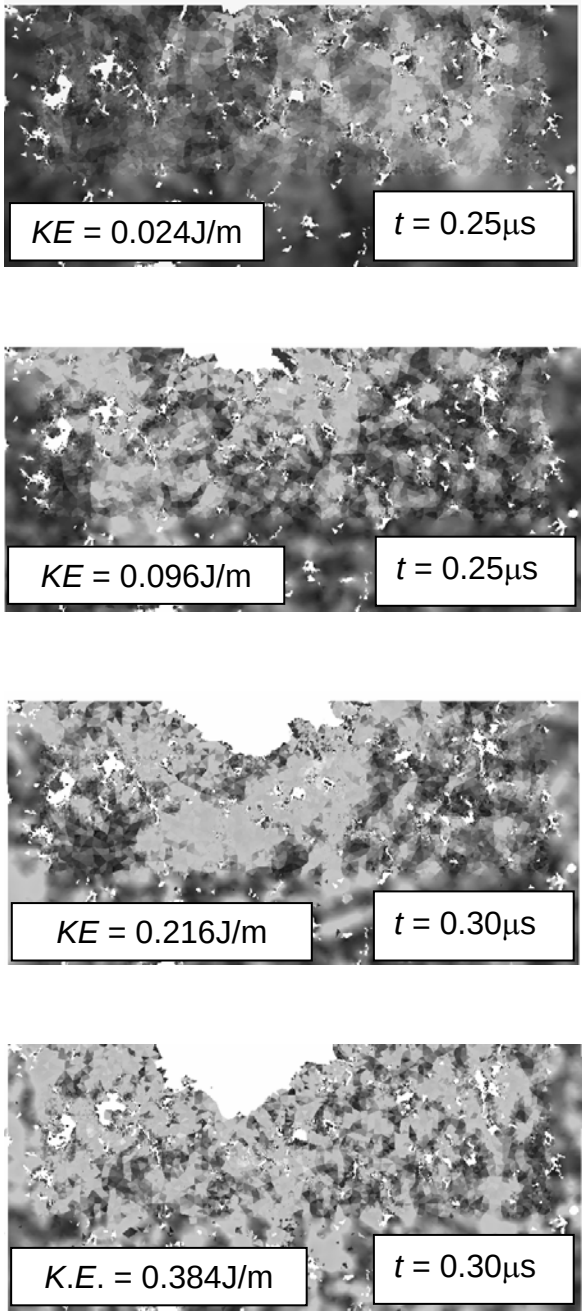

Fig. 4.10. Eroded profiles after completion of impact process due to single particle for various incident kinetic energies corresponding to v = 50m/s, v = 100m/s, v = 150m/s and v = 200m/s.

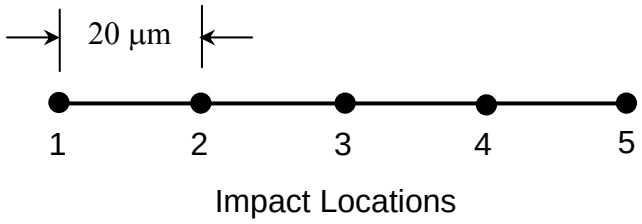

(a)

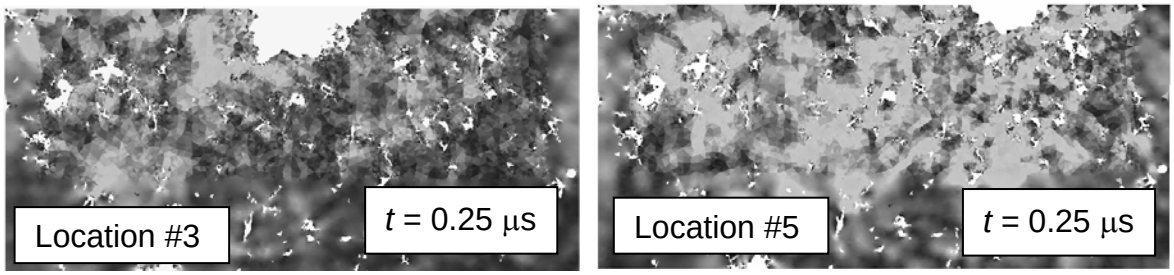

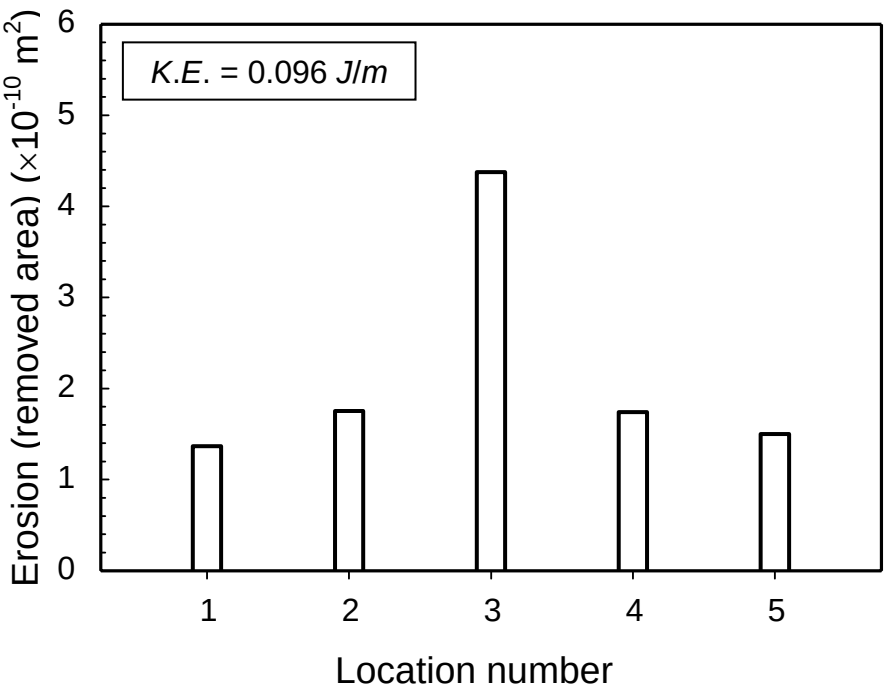

(b)

Fig. 4.11. (a) Schematic showing the 5 different locations of impact. (b) Removal area due to erosion from surface with a single particle for coating type, YSZ (v =100 m/s). Surface profile for 2 different locations are also shown geometrically.

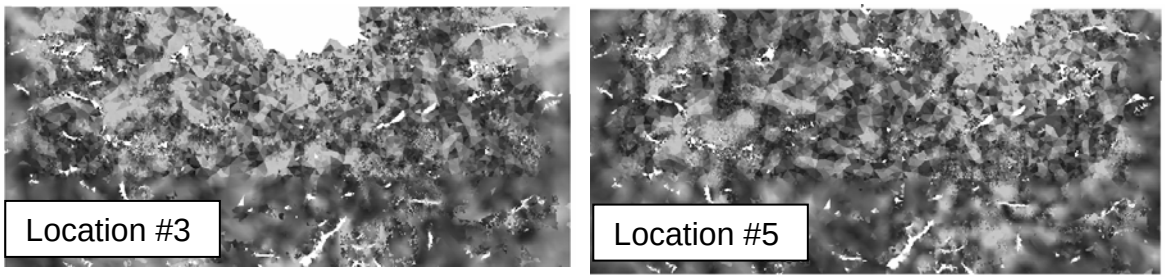

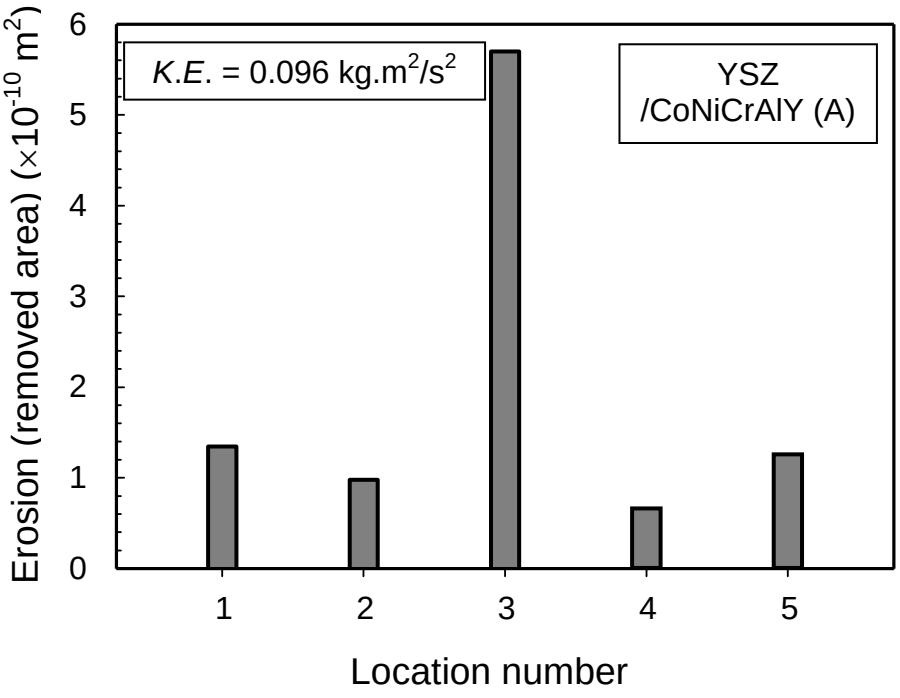

Fig. 4.12. Removal area due to erosion from surface with a single particle for coating type, YSZ/CoNiCrAlY(A) (v =100 m/s). Surface profile for 2 different locations are also shown geometrically.

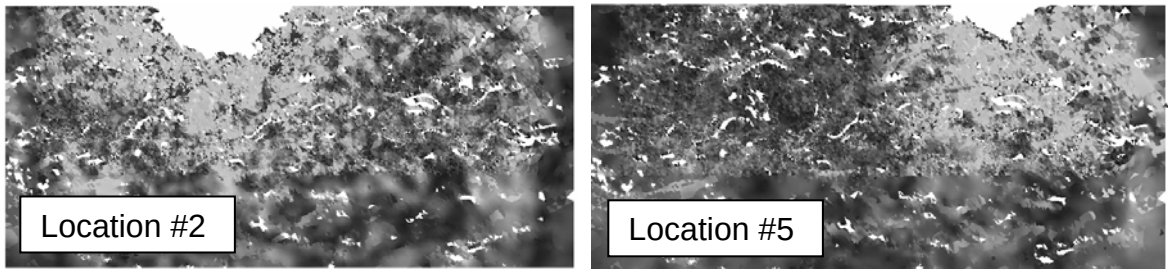

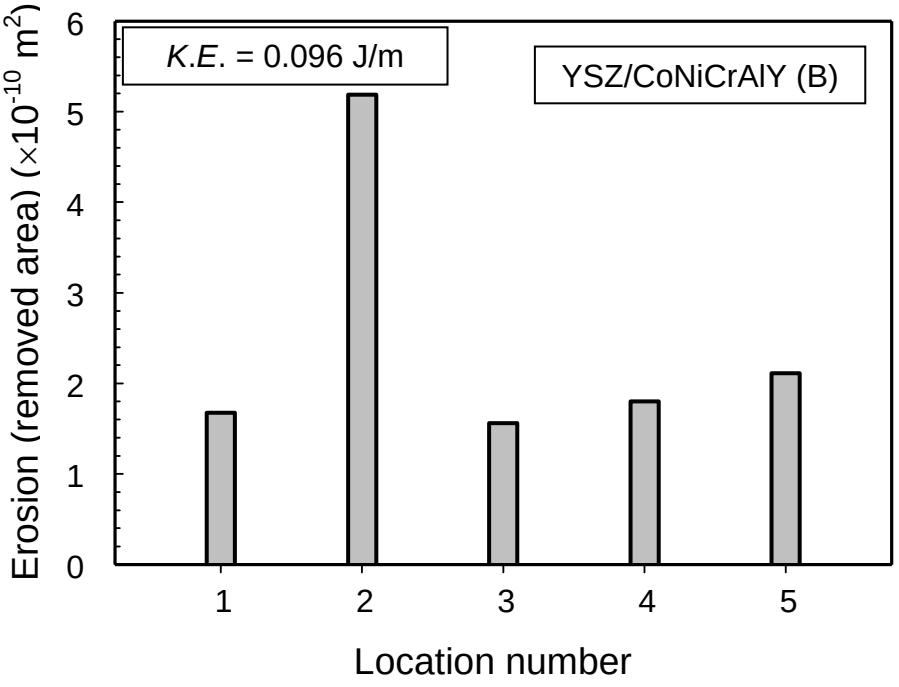

Fig. 4.13. Removal area due to erosion from surface with a single particle for coating type, YSZ/CoNiCrAlY(B) (v =100 m/s). Surface profile for 2 different locations are also shown geometrically.

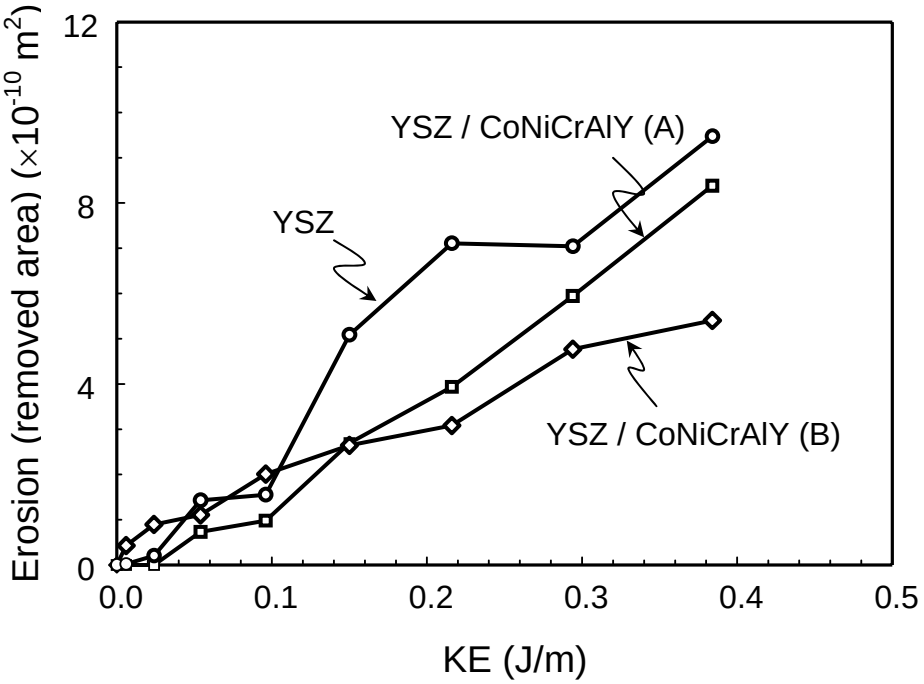

Fig. 4.14. Variation of (a) area eroded with impact velocity of alumina particle and (b) approximate volume eroded for the 3 different coating models with $\rho_{particle}$ = 11700 kg/m^3.

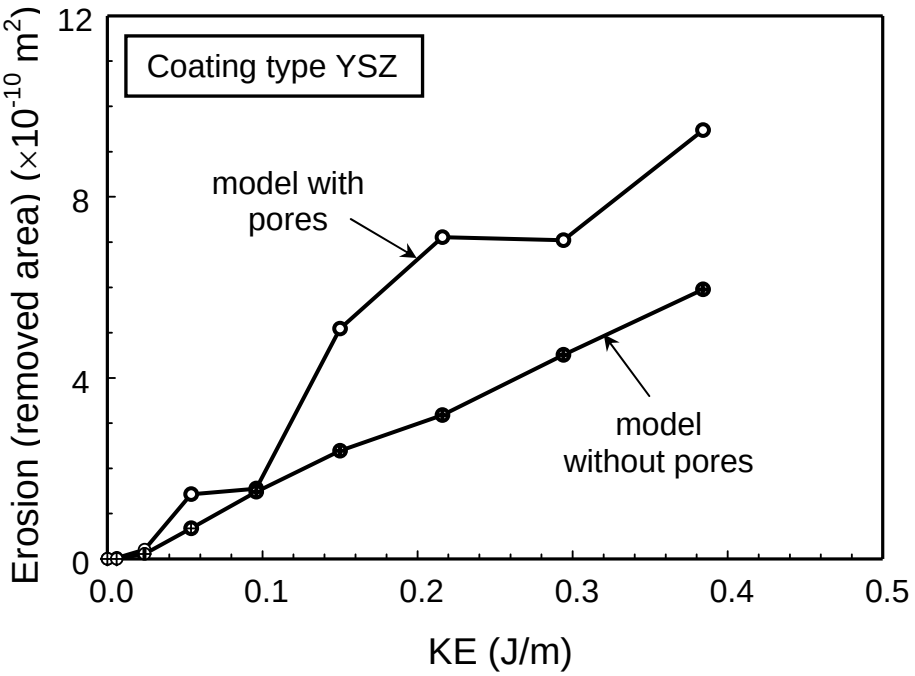

Fig. 4.15. Effect of pores on (a) area removed and (b) approximate volume removed for the coating type YSZ. The density, $\rho_{particle}$ = 11700 kg/m^3.

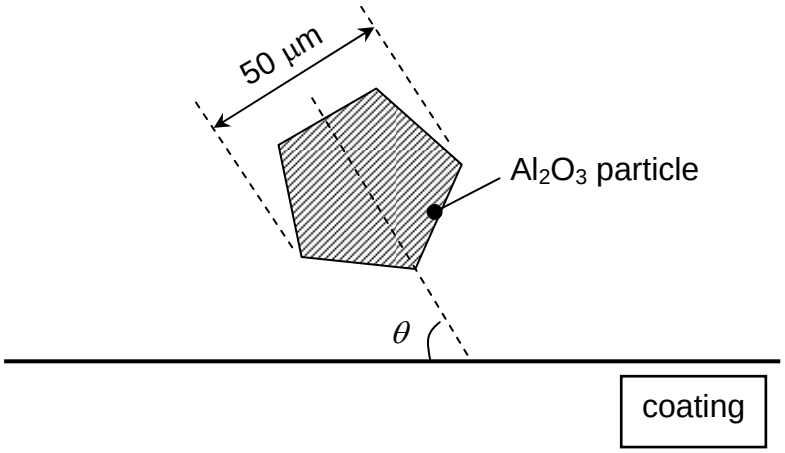

(a)

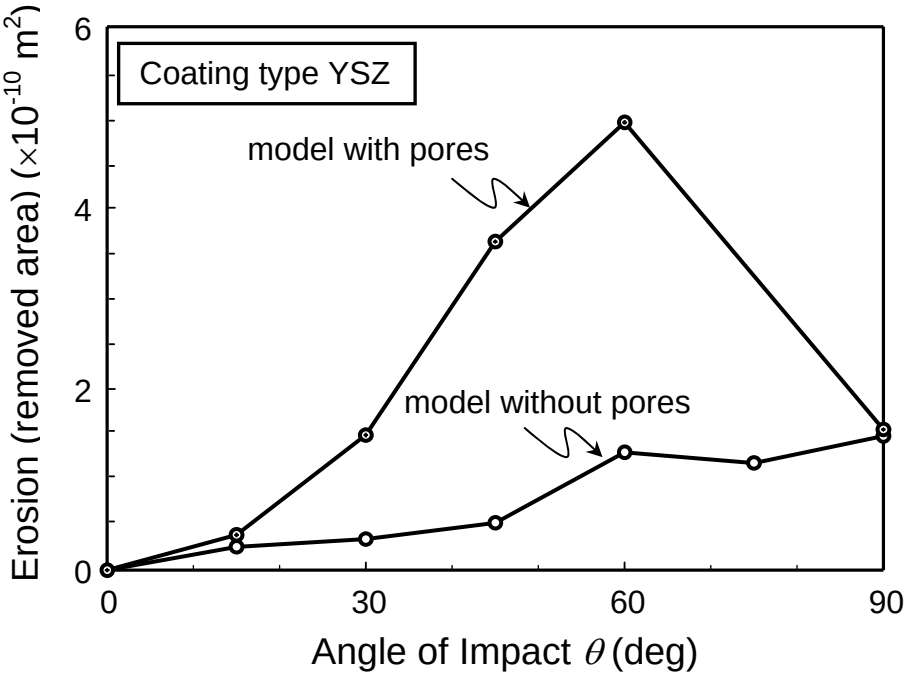

(b)

Fig. 4.16. Effect of angle of impact on the area removed for the coating type YSZ. The density, $\rho_{particle}$ = 11700 kg/m^3.

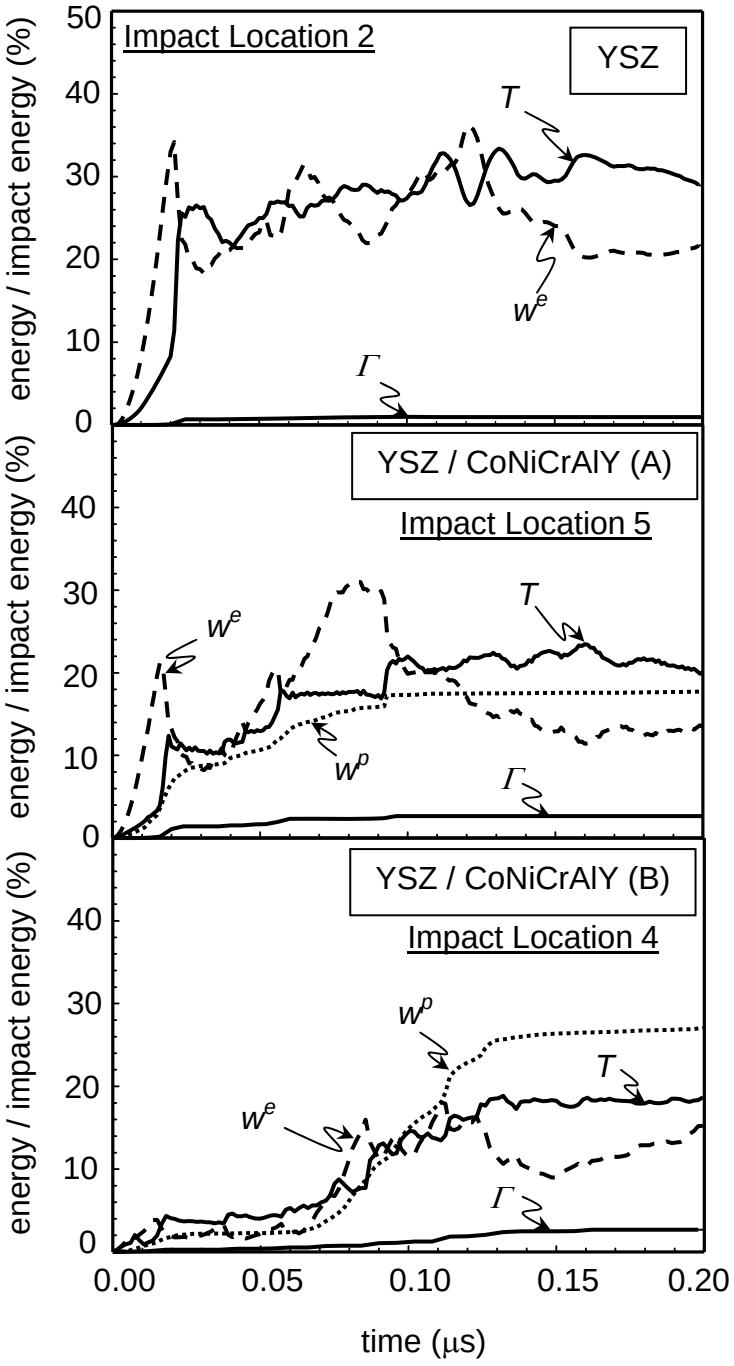

Fig. 4.17. Energy evolution behavior for the different coating types with particle kinetic energy (KE=0.024 J/m and v=50m/s).

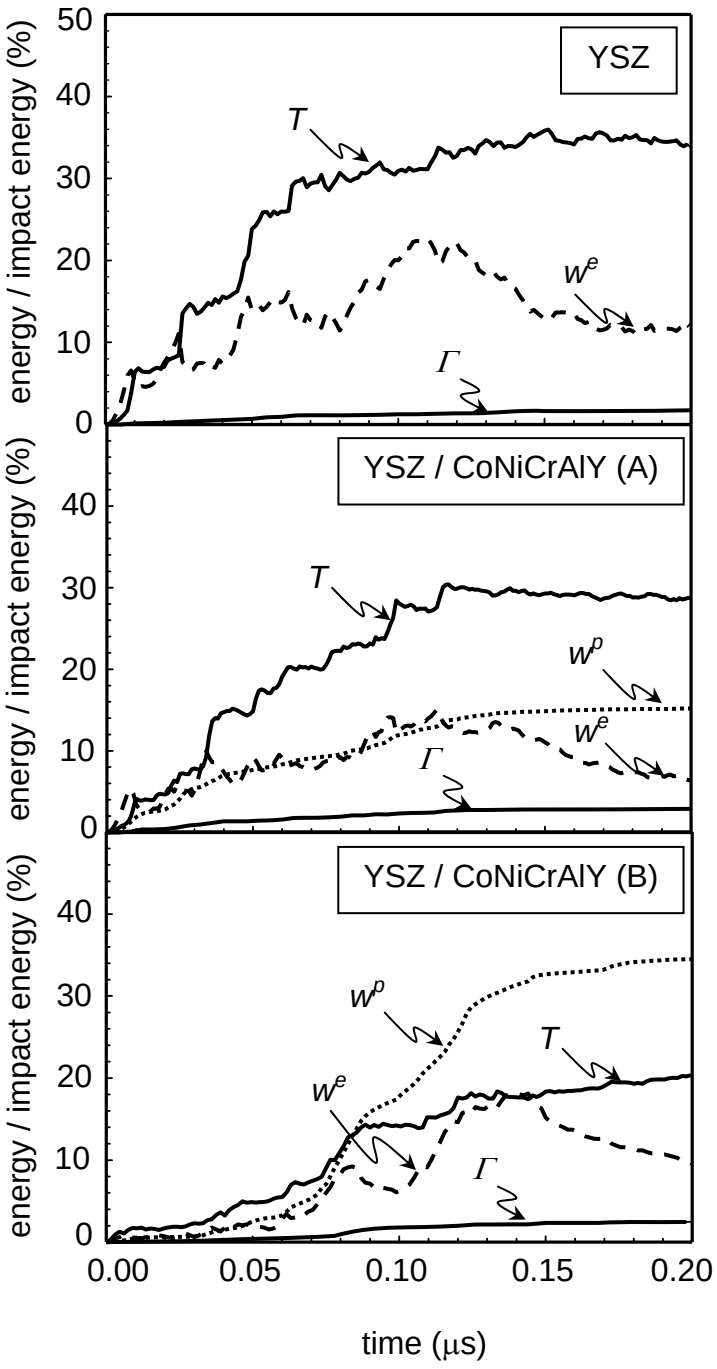

Fig. 4.18. Energy evolution behavior for the different coating types with particle kinetic energy (KE=0.096 J/m and v=100m/s).

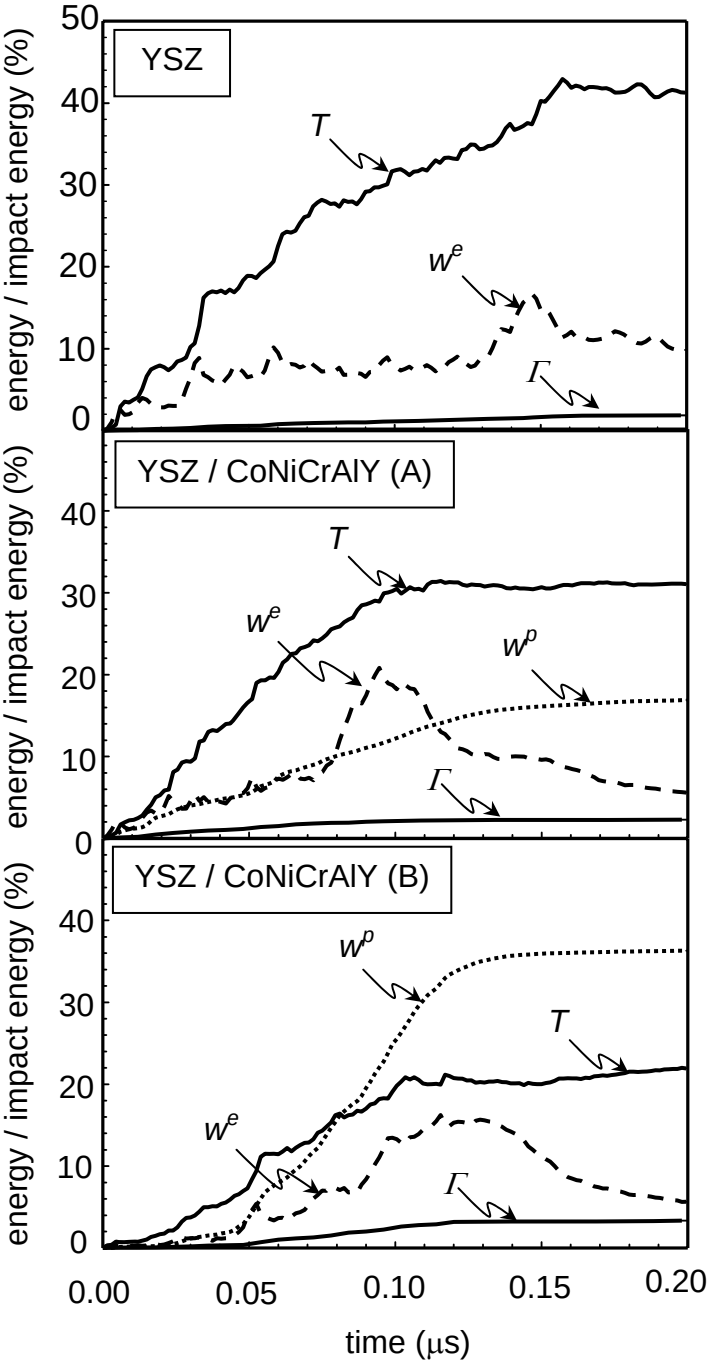

Fig. 4.19. Energy evolution behavior for the different coating types with particle kinetic energy (KE=0.216 J/m and v=150m/s).

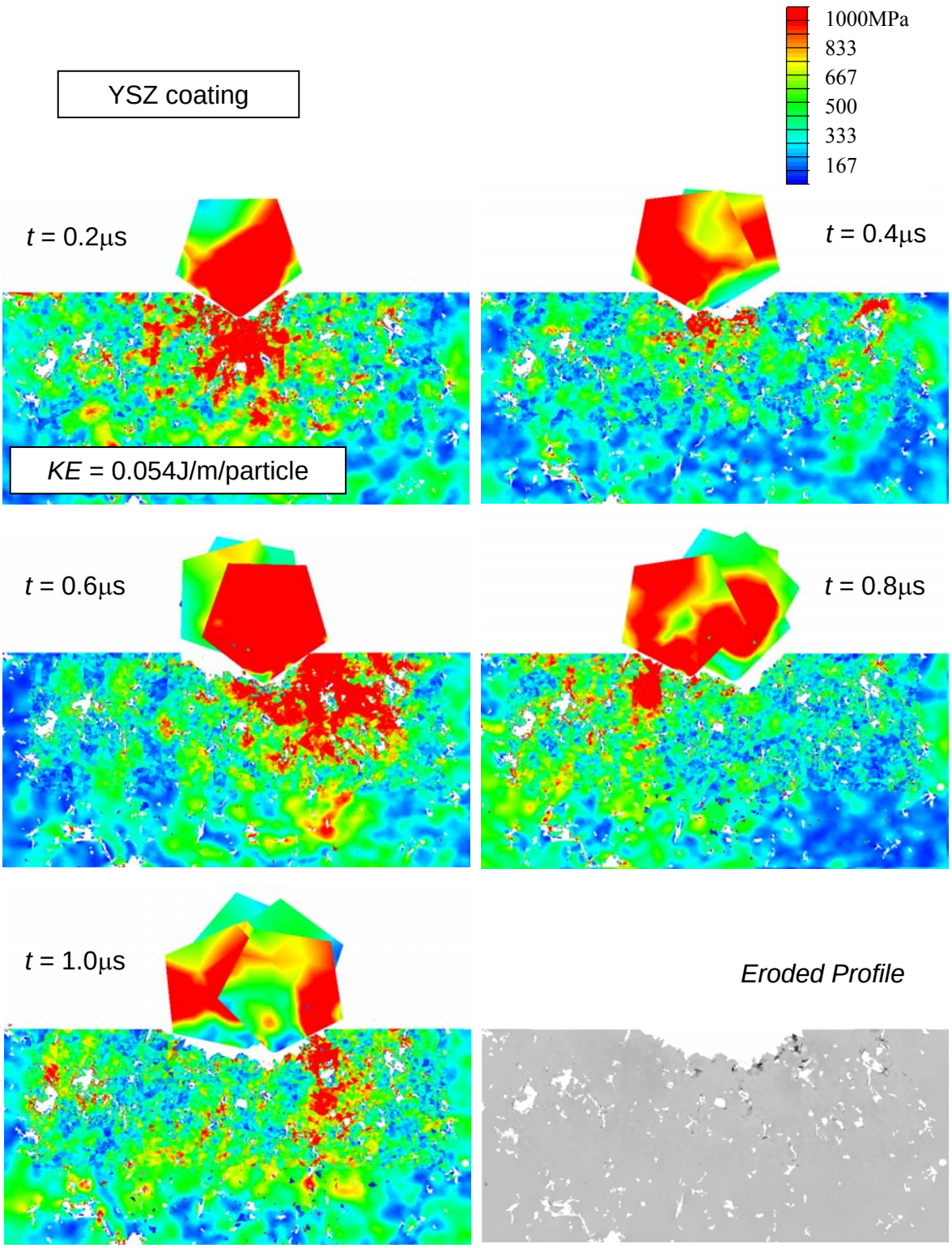

Fig. 4.20. Shades of effective stress showing progression of erosion in YSZ coating after every particle impact with KE = 0.054J/m/particle (v = 75m/s). The final eroded profile is illustrated in the last figure.

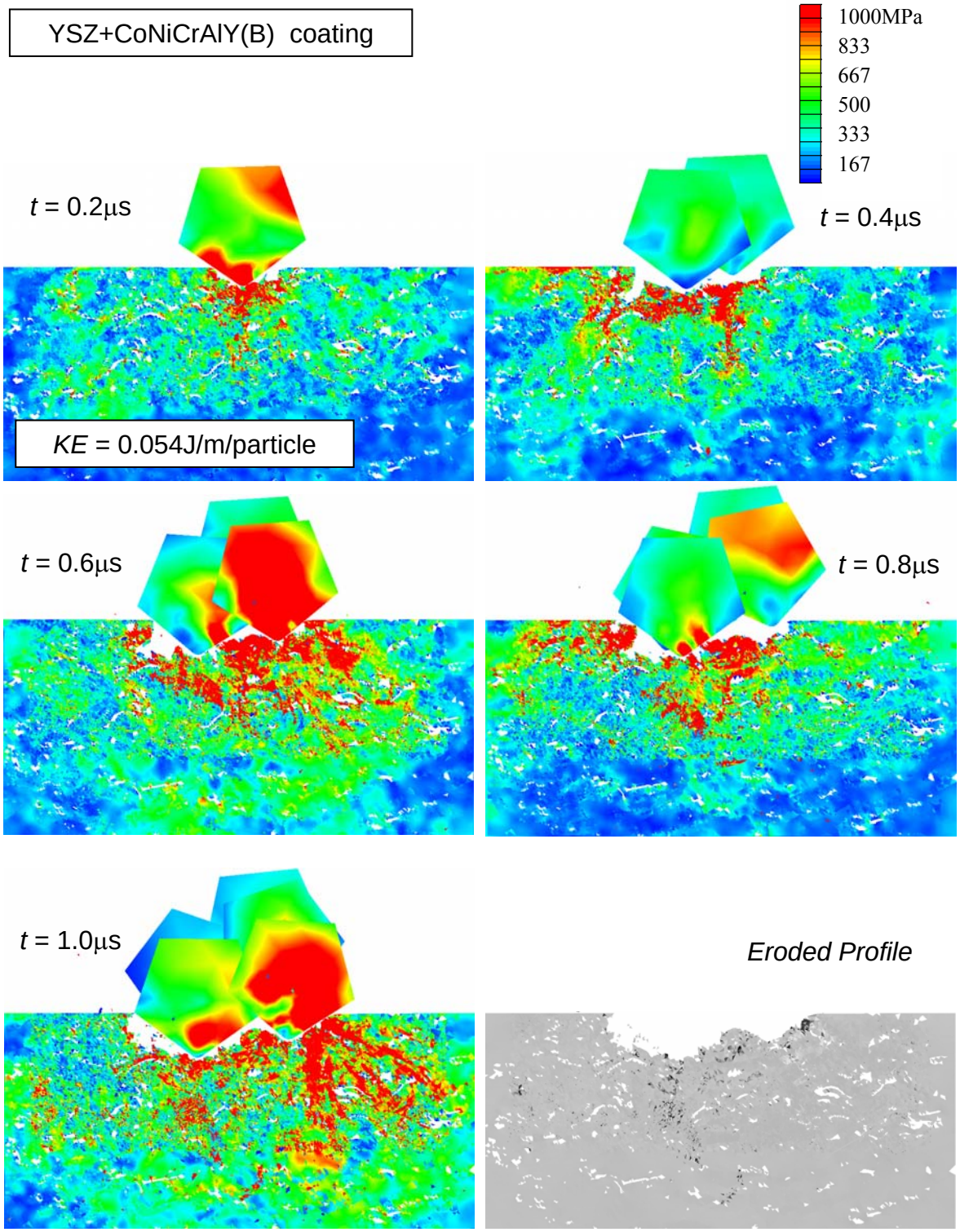

Fig. 4.21. Shades of effective stress showing progression of erosion in YSZ /CoNiCrAlY(B) coating after every particle impact with KE = 0.054J/m/particle (v = 75m/s). The final eroded profile is illustrated in the last figure.

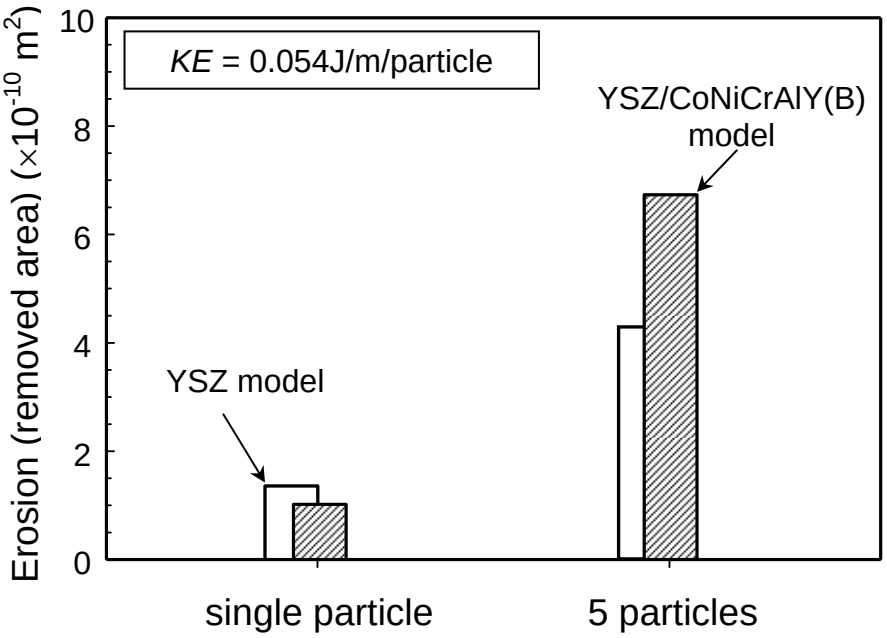

Fig. 4.22. Differences in removed areas by erosion for a single particle impact compared to area removed by impact of 5 particles for two different coating types.

5. Discussions

The goal of present research is characterization of damage by surface thinning occurring in heterogeneous material systems due to different environmental conditions. Heterogeneous material systems are increasingly being favored as they allow for tailoring of mechanical and physical properties by manufacturing process control. Here, two different material systems including continuous fiber-reinforced composites and thermally sprayed coatings were taken into consideration. Heterogeneous material systems are used for a variety of purposes. Whereas fiber-reinforced composites are used as components and structures for a wide variety of applications, coatings are used for protecting underlying substrates rather than for designed-in or prime-reliant applications. However, they are susceptible to the detrimental effects of environmental conditions. These include the more expected damage conditions, for example, exposure to UV radiation, moisture and thermal cycling that occur during outdoor service and the unexpected damage conditions including foreign particles impact. Actual damage mechanisms in current study were simulated using an accelerated weathering chamber, sand erosion and alumina particle erosion. Current studies should not only be useful in promoting our understanding on the effects of these complex conditions but also aid in the assessment of residual strength and remaining life of these heterogeneous systems.

In the first phase of work, damages are characterized for composites used in prime reliant applications where they are exposed to UV-radiation, moisture and sand environments. Strain sensors were used to detect the increased compliance in composites due to weakening. Even though the inverse analysis procedure suggested an ex-situ approach to

estimate damage extents, the procedure can be modified to make it an in-situ approach (For example, using continuous real-time strain measurements by using electric currents). Such a modification would provide useful information for more complex assessments of in-service performance for so-called structural health monitoring (SHM). The other important environmental condition namely the thermal cycling was investigated in the second-phase of the work. Delamination growth rates were correlated with energy release rates using a Paris law. A simple visual detection method was used to detect growth rates instead of sensor networks. Regardless of the method used for detection of anomalies in heterogeneous materials, understanding of the effects of individual external factors is essential. This is the reason for studying the isolated effects of various environmental conditions.

Heterogeneous material systems find importance in applications that are not prime-reliant. Examples of these systems are coatings that protect underlying substrates from erosion, foreign object damage and thermal shock. Hence, plasma sprayed coatings subjected to alumina particles impacts are examined in current study. Damages are characterized through determination of mass loss through experiments and identified using image analysis techniques for computational models. Behavior of coatings is well understood due to expected external events. However, their behavior due to unexpected damage events forms a crucial part of the present work. Current approach presents a new computational modeling approach for prediction of damage due to cracking and chipping resulting from solid particle erosion that occurs in abradable seal sections of gas turbines for example.

Thus, in the present thesis, different suitable approaches for characterization of damages due to various in-service conditions in heterogeneous material systems are discussed.